

**Naval Research Laboratory**

Washington, DC 20375-5000



NRL/MR/4720-92-6960

**AD-A251 633**



**Advanced Concepts Theory Annual Report 1991**  
**Final Report**

*Radiation Hydrodynamics Branch*  
*Plasma Physics Division*

April 27, 1992



This research was sponsored by the Defense Nuclear Agency under Subtask RLRA/Advanced Technology Development, and Work Unit Code and Title, 000789, "Advanced Technology Development," MIPR No. 91-588.

**92-15679**



REPORT DOCUMENTATION PAGE			Form Approved OMB No 0704-0188	
Public reporting burden for this collection of information is estimated to average 1 hour per response, including the time for reviewing instructions, searching existing data sources, gathering and maintaining the data needed, and completing and reviewing the collection of information. Send comments regarding this burden estimate or any other aspect of this collection of information, including suggestions for reducing this burden, to Washington Headquarters Services, Directorate for Information Operations and Reports, 1215 Jefferson Davis Highway, Suite 1204, Arlington, VA 22202-4302, and to the Office of Management and Budget, Paperwork Reduction Project (0704-0188), Washington, DC 20503.				
1. AGENCY USE ONLY (Leave blank)	2. REPORT DATE Final Report	3. REPORT TYPE AND DATES COVERED		
4. TITLE AND SUBTITLE Advanced Concepts Theory Annual Report 1991, Final Report			5. FUNDING NUMBERS PE-62715H WU-DNA 880-191	
6. AUTHOR(S) Radiation Hydrodynamics Branch				
7. PERFORMING ORGANIZATION NAME(S) AND ADDRESS(ES) Naval Research Laboratory Washington, DC 20375-5000			8. PERFORMING ORGANIZATION REPORT NUMBER NRL/MR/4720--92-6960	
9. SPONSORING / MONITORING AGENCY NAME(S) AND ADDRESS(ES) Defense Nuclear Agency RAEV Alexandria, VA 22310			10. SPONSORING / MONITORING AGENCY REPORT NUMBER	
11. SUPPLEMENTARY NOTES This research was sponsored by the Defense Nuclear Agency under Subtask RLRA/Advanced Technology Development, and Work Unit Code and Title, 000789, "Advanced Technology Development," MIPR No. 91-588.				
12a. DISTRIBUTION / AVAILABILITY STATEMENT Approved for public release; distribution unlimited.			12b. DISTRIBUTION CODE	
13. ABSTRACT (Maximum 200 words)  This report details the work of the Radiation Hydrodynamics Branch conducted in FY 91 with respect to several critical problems concerning the analysis and interpretation of z-pinch experiments, the dynamics of z-pinch implosions, and the optimization of their radiative output. Separate sections describe progress in the analysis of z-pinch experiments using phenomenological turbulence transport parameters, the development of a microturbulence analysis from which to calculate turbulence enhanced transport coefficients, the development of L-shell atomic models, the analysis of PRS argon experiments, and the development of a transmission line model with which to study power flow in IES machines, POS/PRS interactions, and energy coupling to PRS loads.				
14. SUBJECT TERMS Z-pinch physics                      PRS Argon Radiation MHD			15. NUMBER OF PAGES 120	
			16. PRICE CODE	
17. SECURITY CLASSIFICATION OF REPORT UNCLASSIFIED	18. SECURITY CLASSIFICATION OF THIS PAGE UNCLASSIFIED	19. SECURITY CLASSIFICATION OF ABSTRACT UNCLASSIFIED	20. LIMITATION OF ABSTRACT UL	

Contents

EXECUTIVE PROGRAM SUMMARY

I. PHENOMENOLOGICAL TURBULENCE MHD MODELING OF Z-PINCH IMPLOSIONS..... 1

II. EVALUATING PLASMA MICROTURBULENCE AS A POTENTIAL SOURCE FOR THE ANOMALOUS HEATING OF PRS PLASMAS..... 32

III. MODELING AND DIAGNOSING L-SHELL DYNAMICS IN PRS EXPERIMENTS..... 59

IV. POWER FLOW IN DECADE CLASS MACHINES:  
DEVELOPING TRANSMISSION LINE MODELS FOR THE LONG CONDUCTION TIME POS  
COUPLED TO A PRS..... 79

V. THE EFFECT OF 2-D MHD FLOWS ON GAS PUFF PRS PERFORMANCE/OPTIMIZING GAS  
GAS PUFF NOZZLE DESIGNS..... 100



<b>Accession For</b>	
NTIS GRA&I	<input checked="" type="checkbox"/>
DTIC TAB	<input type="checkbox"/>
Unannounced	<input type="checkbox"/>
Justification	
By _____	
Distribution/	
Availability Codes	
Dist	Avail and/or Special
A-1	

## Executive Summary

This final report describes a number of advances that are being made in the NRL Plasma Radiation Source (PRS) Theory Program in the following areas:

1. The phenomenological inclusion of plasma turbulence effects into our average 1-D MHD, detailed descriptions of PRS implosion dynamics.
2. The theoretical evaluation of a variety of plasma microturbulence mechanisms and the calculation of their effects on electrical, momentum, and energy transport processes in PRS plasmas.
3. The development of x-ray radiation dynamic atomic models in the L-shell of moderate atomic number plasmas.
4. The development of a transmission line model for DECADE-class machines that is designed to incorporate what is known about POS (and determine some of the unknowns) in order to investigate the interactions of POS with PRS loads and the effect of this interaction on power flow.
5. The application of a 2-D MHD description of PRS implosions to analyze gas puff experiments in order to optimize the design of nozzles, which, in turn, should aid in the optimization of PRS gas puff operation in DECADE-class machines.

These subjects are discussed in detail in each of the following five sections of this report and are summarized briefly below.

During the past several years, it became clear that the ideal dynamical, PRS implosion behavior predicted by detailed, 1-D, Radiative MHD calculations was not being achieved experimentally. However, it was evident from a post-analysis of these calculations that the current flow and plasma conditions being generated during idealized implosions were those needed for triggering

plasma turbulence in one form or another. The questions then arose: could turbulence induced increases in plasma viscosity, heat conductivity, and electrical resistivity account for the observed differences between calculations and experiment, and how would these increases in plasma transport affect the scaling of x-ray yields with machine current and implosion kinetic energy? Work on these questions was begun during the past year and some of the preliminary findings are described in section I of this report. The answer to the first question is yes: we can now explain experimental results with average 1-D Radiative MHD calculations provided we can make the right phenomenological choice of plasma transport, turbulence parameters. In addition, we also have a program in place, which requires joint theoretical and experimental collaboration, to determine how these turbulence parameters scale from experiment to experiment and from machine to machine. We can also make predictions of how a fixed set of turbulence parameters will affect the scaling of x-ray yield with current and implosion velocity. Moreover, when equipped with the knowledge of how these parameters are scaling in experiments, we can begin to anchor the scaling predictions to experiment.

We would also like to anchor them with theory. Some work in this direction is described in section II. The questions being addressed in section II are: Can plasma microturbulence be invoked to explain the magnitude of the anomalous resistivity commonly attributed to experimental PRS plasmas, i.e., will a physically realistic level of electrostatic plasma fluctuations produce the required resistivity increase and can these fluctuations be triggered and become saturated in a dynamically evolving z-pinch? What kinds of non-Maxwellian electron distributions will be generated by the microturbulence and can these non-Maxwellians be diagnosed from the plasma's emitted x-ray spectrum?

The reason that differences between theory and experiments can be diagnosed and quantified is because systematic experimental data analysis procedures were developed in the NRL Theory Program over the last several years. These procedures were successfully applied in the analysis of K-shell x-ray emissions from MLI and PI experiments. Efforts to analyze some recent PI argon experiments using these procedures are described in section III. It is vital that these procedures be extended into the L-shell of moderate atomic number plasmas. Some of the problems involved in this extension are being

investigated through the development of a selenium atomic model whose reliability has been benchmarked against the x-ray laser literature. The challenge in this development is to properly treat the multiplet state structure in the L-shell, which is of much greater importance to the problem of calculating x-ray output in the L-shell than it is to the similar K-shell problem. Accurate calculations of L-shell x-ray output, however, are also important ingredients in calculations of K-shell x-ray production from PRS plasmas, since the plasma must burn through the L-shell before it can emit in the K.

Other important problems for scaling PRS to DECADE-class machines involve machine power flow and the POS operation. To maximize the power output from a PRS it is necessary to maximize the power flow and kinetic energy generation into the PRS. This problem is being addressed through the development of a DECADE transmission line model in which the power flow through the POS and MITL to the PRS load can be calculated and the mutual interaction and effect of these elements on each other investigated. Crucial to this modeling is the development of improved physics models to describe the conduction phase and the gap dynamics of Plasma Opening Switches (POS). The beginning development of these efforts, which are being designed to feed into the transmission line model development, are discussed in section IV.

Finally, we note that another form of turbulence is hydromagnetic turbulence, which is a 3-D fluid flow phenomenon. One way to gain some insights into the growth of hydromagnetic turbulence in PRS implosions is through the development and utilization of a 2-D MHD description of PRS implosions. Another benefit of this development, which is an intrinsic 2-D flow application of 2-D MHD, is described in section V of this report. In this section, calculations are presented of the implosion dynamics resulting from a 2-D MHD simulation of a series of PI argon gas puff experiments. It was found in these experiments that x-ray yields were increased and the x-ray pulse sharpened when the argon injection nozzles were properly tilted inwards to compensate for the outward flow of gas from the nozzles. The calculations helped to explain the effect of nozzle orientation on x-ray output by quantifying the effect of axial gas flow has on the implosion dynamics. Thus benchmarked, these calculations should provide useful guidance in designing gas puff nozzles for use in the DECADE PRS Simulator.

# ADVANCED CONCEPTS THEORY ANNUAL REPORT 1991

## Final Report

### I. Phenomenological Turbulence MHD Modeling of Z-Pinch Implosions

#### A. INTRODUCTION

Past and current z-pinch experiments have produced more energy coupling to the plasma load, lower ion densities at peak implosion, and longer radiation pulse widths than predicted by idealized 1-D MHD calculations.<sup>1-7</sup> Some attempts have been made to reconcile these differences by including enhanced resistivity,<sup>3-5</sup> time dependent ionization dynamics,<sup>1,6</sup> and short circuiting of the power flow in the calculations.<sup>3,6</sup> In general these attempts are encouraging, but they also indicate that more physical phenomena are taking place in experiments than are presently included in our MHD descriptions of z-pinch dynamics. In this work an investigation to determine the extent that some of the differences between theory and experiment can be attributed to plasma turbulence is undertaken. Turbulence effects are modeled in our 1-D, radiation, MHD models by increasing the resistivity, viscosity, and heat conductivity transport coefficients. This is accomplished in two stages: first, a typical z-pinch experiment is modeled in which thermal conductivity,  $\kappa$ , and artificial viscosity,  $\nu$ , are systematically enhanced in order to map out a parameter space in  $(\nu, \kappa)$  space that produces results in phenomenological agreement with experiment; secondly, once values for  $(\nu, \kappa)$  are chosen, they are employed to model a specific set of argon experiments run on Physics International's Double Eagle Machine. At this stage the value of resistivity,  $\Omega$ , is varied to determine how it affects experimental agreement.

We find that enhanced numerical transport is capable of achieving remarkable agreement with experiment, especially when compared to previous efforts. Although this phenomenological work cannot in itself determine the

degree to which enhanced transport exists in a z-pinch driven plasma, it does indicate a more rigorous evaluation of turbulence effects is warranted. This evaluation will involve a systematic program of experimental/theoretical collaboration to map out the trends and trade-offs involved in the z-pinch implosions as a function of atomic number and current scaling.

The numerical model is reviewed in section B, the mapping of (v,κ) parameter space is discussed in section C, section D describes results for the enhanced resistivity simulation of the argon experiments for fixed (v,κ), and section E is comprised of conclusions.

## B. NUMERICAL MODEL

The most complete hydrodynamic model used to describe z-pinch implosions consists of continuity, momentum, and energy equations that are solved numerically in a Lagrangian reference frame with cylindrical geometry and axial symmetry. The fluid equations describing the plasma dynamics are:

Mass continuity,

$$dV/dt = (V/r)[\delta(ru)/\delta r]; \quad (1)$$

momentum conservation,

$$du/dt = -V(\delta P/\delta r) - (V/r)[\delta(rQ)/\delta r] + (VJB)/c; \quad (2)$$

an equation describing the change in electron internal energy, namely,

$$dE_e/dt = -P_e(dV/dt) + (V/r)\{\delta[rK_e(\delta T_e/\delta r)]/\delta r\} + V\eta J^2 + R + 2\omega_c(T_i - T_e); \quad (3)$$

ion internal energy conservation,

$$\begin{aligned} dE_i/dt = & - P_i(dV/dt) + (V/r)\{\delta[rK_i(\delta T_i/\delta r)]/\delta r\} - VQ\delta u/\delta r \\ & - 2\omega_c(T_i - T_e). \end{aligned} \quad (4)$$

In these equations,  $V$  is the specific volume,  $u$  the radial fluid velocity,  $P$  the total particle pressure;  $P_e$  and  $P_i$  are, respectively, electron and ion pressures,  $E_e$  and  $E_i$  electron and ion internal energies,  $K_e$  and  $K_i$  electron and ion thermal conductivities,  $T_e$  and  $T_i$  electron and ion temperatures;  $Q$  is the Von Neumann artificial viscosity,<sup>8</sup>  $R$  the specific radiative loss or gain term, and  $\omega_c$  the electron-ion collision term.  $\eta$  is the Spitzer resistivity transverse to the magnetic field,  $J$  the axial current density, and  $B$  the azimuthal magnetic field intensity. The transport coefficients  $K_e$ ,  $K_i$ , and  $\omega_c$  are given conventionally by Braginskii.<sup>9</sup>

These equations are put in closed form by using ideal gas - like equations of state for the electron and ion pressures, i.e.

$$P_e = 2/3 V(E_e - E_z), \quad (5)$$

$$P_i = 2/3 V E_i, \quad (6)$$

where  $E_z$  is the potential energy due to ionization and excitation of the atoms.

A Lagrangian form of the magnetic diffusion equation is used to calculate the spatial and temporal evolution of the magnetic field. This equation is

$$(1/r)d\Psi/dt = (c^2/4\pi)\delta[(\eta/r)\delta\Psi/\delta r]/\delta r - \Psi\delta(u/r)/\delta r, \quad (7)$$

where  $\Psi$  is equal to the product of the magnetic field  $B$  and the radius  $r$ . Once the magnetic field  $B(r,t)$  is known, the current density profile  $J(r,t)$  is calculated from Faraday's law,

$$(1/r)\delta[rB(r,t)]/\delta r = (4\pi/c) J(r,t). \quad (8)$$

The total current  $I$ , which is either prescribed in these simulations or else self-consistently calculated using a circuit model of the pulse power machine, provides a boundary condition for the magnetic field  $B$  at the outer radius of the plasma.

Some quantities in the preceding equations are obtained by solving ionization and radiation dynamics equations. These are, the radiative loss rate  $R$ , the ionization and excitation energy density  $E_z$ , and the effective charge of the plasma  $Z$ . The ionization and radiation dynamics are treated self-consistently using fully time dependent collisional radiative (CR) radiation and atomic physics models developed at NRL (see the references listed in Ref. 10). The ionization dynamics of the argon plasma is determined from 18 ground states and 61 excited levels. The excited levels are distributed primarily in hydrogen-like through aluminum-like argon because these ion stages are most prevalent in the implosion calculations that will be described shortly.

Radiation is coupled to the plasma through emission and absorption processes. The processes of photoionization and photoexcitation directly affect the populations while inner-shell absorption and radiative cooling produce indirect changes by altering the temperature  $T_e$  of the plasma. In order to include these important processes self-consistently, the radiation field must be transported. This is accomplished by a probabilistic transport scheme in which angle and frequency averaged escape probabilities are

calculated for each emission process.<sup>11,12</sup> The hydrogen and helium  $\alpha$ ,  $\beta$ , and  $\gamma$  lines are transported, along with 74 additional lines, in order to ensure good energy coupling and to provide good diagnostic information.

### C. MAPPING OF $(\nu, \kappa)$ PARAMETER SPACE

A prototypical z-pinch experiment consists of an 85  $\mu\text{g}/\text{cm}$  argon gas puff having an initial outer radius of 1.28 cm and an inner radius 1.18 cm. Ninety three percent of the mass lies between the inner and outer radii and it is taken to be of uniform density. There are 24 spatial zones used to resolve this region. The remaining mass is distributed over the six zones spanning the space between the origin and the inner radius. The inner zones and mass are included primarily for numerical stability but they also model the effects of plasma that is blown in to the origin by the initial wire/gas puff explosion. The initial plasma temperature is taken to be 5 eV. The pinch is driven by a linearly ramped current profile  $I = I_p t/\tau$ , where  $I_p$  is the peak current, which is 3 MA (for the double Eagle Machine),  $t$  is the time, and  $\tau$  is an implosion time of 110 ns. Similar to earlier work, when the outer radius reaches  $\sim 0.1$  of the initial radius the current is terminated. This allows focus on the kinetic energy thermalization aspect of the implosion and it insures that each calculation couples approximately the same amount of energy to the load. In general, in the absence of significant ohmic heating, this energy coupling is inductive and is given by  $\sim 1/2 \Delta L I_p^2$ , where  $\Delta L$  is the change in inductance. The current profile used in these simulations is representative of the load driving current produced by Double Eagle and the initial radii of the puff is indicative of a Double Eagle nozzle.

Before discussing the results for the mapping of  $(\nu, \kappa)$  space, some dramatic differences between previous calculations and experiment are highlighted by examining mass averaged profiles for ion density and radiative power for a simulation run under the conditions described above, but in which the transport coefficients are set to their classical values; that is,  $\kappa = \kappa_c$ ,  $\nu = \nu_c$ , and  $\Omega = \Omega_c$ , where  $\kappa$  is thermal conductivity,  $\nu$  is viscosity,  $\Omega$  is resistivity, and  $( )_c$  refers to classical value. Figure 1 displays a peak ion density of  $\sim 6 \times 10^{21} \text{ cm}^{-3}$  and Fig. 2 depicts a peak radiative power of  $\sim 80$  terrawatts. To our knowledge densities and powers of these magnitudes have never been achieved in a z-pinch. In particular, the argon gas puff experiments, which will be discussed in detail in the next section, produced peak radiative powers on the order of a terrawatt/cm and self-consistent analysis of He- $\alpha$  to Ly- $\alpha$  line ratios<sup>13</sup> reveal that peak ion densities were  $\sim 10^{19} \text{ cm}^{-3}$ . This is a somewhat loose comparison between experiment and calculation since the experimental mass loading is believed to be 52  $\mu\text{g/cm}$  and the driving current was slightly different than used in the calculations. However, it is doubtful that these differences alone are responsible for the two to three order of magnitude variances in density and radiative power.

Results from numerous calculations are presented in which viscosity and thermal conductivity (both ion and electron) are enhanced. Specifically, the mass averaged peak ion density, Fig. 3, and total K-shell radiative emission, Fig. 4, are examined as a function of  $(\nu, \kappa)$ . Note, real viscosity is not included in the model but rather a Von Neumann artificial viscosity  $Q = C_0^2 \rho l^2 |du/dr|$  is employed to handle shocks and resolve the Lagrangian computational mesh, where  $C_0$  is a constant of order unity,  $\rho$  is the mass density,  $l$  is a characteristic dimension of the mesh, and  $u$  is the radial velocity. Viscosity is increased by varying  $C_0$  between 1 and 10. However,

to preserve the mesh handling nature of an artificial viscosity,  $Q$  should be kept as is and then a multiple of real viscosity should be added to the momentum (2) and energy (4) equations. This is to be done in the future, but for now, since the interest is in determining only the qualitative nature of viscous effects on the numerical simulations, the treatment is adequate.

Fig. 3 demonstrates that there is a substantial decrease in the peak ion density as artificial viscosity and thermal conductivity are enhanced. An examination of the  $\kappa=\kappa_c$  curve (curve A) shows that the peak density is decreased by a factor of 17 when  $C_0^2$  is increased from 2 to 49. Likewise, for the  $\kappa=30 \times \kappa_c$  curve (curve D), the ion density is decreased by over two orders of magnitude. The experimental evidence is that the peak ion density is  $\sim 10^{19} \text{ cm}^{-3}$  for an experiment of this nature. Allowing for an order of magnitude discrepancy, Fig. 3 reveals that only those calculations with values of  $C_0^2$  in excess of 40 ever produce densities close to experimental values. The peak density was not as sensitive in regards to thermal conductivity, i.e. the results for  $\kappa=10 \times \kappa_c$  (curve C) were nearly identical to the results for  $\kappa=30 \times \kappa_c$ . This is especially true for large  $C_0^2$ , where both cases achieved ion densities in accord with experiments.

Assuming identical fluids, the same compressional work, and the same initial volume, an adiabatic compression produces more compression in a fluid having a smaller initial internal energy. With this in mind, it is clear why increasing the viscosity, which transfers kinetic energy into internal energy in order to reduce velocity gradients that exist in the plasma, makes compression more difficult. While enhancing thermal conductivity does not influence the global internal energy, it does distribute energy evenly throughout the plasma. Specifically, it takes energy from the hot core and from the high temperature resistive regions that exist at the corona of the pinch and distributes it to the rest of the

plasma; making it more difficult to compress the plasma which lies between the outer radius and the core. By limiting the compression, enhanced viscosity and thermal conduction also produce a non-linear reduction in radiative cooling that can severely limit the ability of the plasma to lower its internal energy and consequently compress. This is because radiative cooling varies as the square of the number density for optically thin bremsstrahlung and recombination radiation; and therefore a slight decrease in density makes it more difficult for the plasma to cool.

Fig. 4 is very interesting because it illustrates that the calculated K-shell emission is not very sensitive to the size of the viscous and heat conduction transport coefficients - a surprising result since Fig. 3 shows that the dynamics of the implosion are significantly affected. Implosions with near classical transport coefficients produced large radiative powers and short radiation times, whereas, large viscosity and thermal conductivity produce smaller radiative powers and longer radiation times. This suggests that there is an important trade-off between radiative power  $\dot{Y}$  and the radiation time  $\tau$ .

Recent theoretical work that focused upon kinetic energy thermalization and used classical transport showed that an efficient implosion produce K-shell yields that are 20 to 40 percent of the inductively coupled energy.<sup>14</sup> In our case, this amounts to K-shell yields of 4 to 8 kJ/cm. It is apparent that numerous choices of  $(\nu, \kappa)$  produce K-shell yields in this range. Experiments tend to produce more K-shell emission than 20 to 40 percent of inductively coupled energy, at least for  $Z \leq 13$ . In part this is thought to be attributable to anomalous resistivity and heating.<sup>2</sup> There has been little documented, systematic, experimental evaluation of K-shell emission for  $z > 13$ .

#### D. SIMULATION OF ARGON EXPERIMENTS WITH FIXED ( $\nu, \kappa$ ) AND VARIABLE $\Omega$

In the last section it was discovered that  $C_0^2$  values in excess of 40 were necessary to obtain implosion ion densities in accord with experiments. Since  $C_0^2 = 49$  was the lowest value that was tested larger than 40, it is used in the following calculations for  $\nu_c$  (classical viscosity coefficient). Having made this choice, Fig. 4, and the limited experimental evidence described above suggest that  $30 \times \kappa_c$  is a good selection for  $\kappa$ .

There were 35 argon gas puff experiments performed to explore the optimization of K-shell emission on Double Eagle. This involved a large number of variations in initial mass loading (plenum pressure), nozzle radii and design, length of the pinch region, and charge on the capacitor banks. To limit the number of comparisons with numerical calculations a subset of three typical experiments that had the same arrangement and yielded consistent values of K-shell radiative yield, K-shell radiative pulse width, and total X-ray emission are modeled. In this subset, argon is injected from a 2.5 cm diameter mach 4 nozzle. The capacitor banks were charged to 55 kV and the pressure in the gas plenum was 80 psi. A lumped circuit diagram of Double Eagle is shown in Fig. 5 and a typical machine voltage profile is displayed in Fig. 6. The available experimental information on these three shots is listed in Table 1. The mass loadings were determined from slug model analysis and knowledge of the implosion time. The K-shell yields were measured using kapton filtered tantalum foil calorimeters and also by numerical integration of filtered X-ray diode (XRD) emission power signals. An unfiltered calorimeter was used to obtain total radiated yield. The spatial and temporal behavior of K-shell emission was determined using the arrangement of Deeney et al.<sup>2</sup> Applying the analysis technique of Coulter et al.<sup>13</sup> to the time integrated K-shell data for shot

2340, which had a  $\text{He}_\alpha$  to  $\text{Ly}_\alpha$  ratio of 4.35, it is estimated that during the time K-shell radiation is emitted the time and spatially averaged ion density was  $6.8 \times 10^{18} \text{ cm}^{-3}$  and the electron temperature was 1660 eV. The measured power curves for total and K-shell emission for shot 2340 are illustrated in Fig. 7.

The experiments are modeled using the same 52  $\mu\text{g}/\text{cm}$  mass loading as shot 2340. The model uses a self-consistent current, which is calculated according to the circuit diagram and voltages displayed in Figs. 5 and 6. The length of the plasma column is 3 cm and the initial location and zoning of the puff are identical to that described in the last section. This puts the center of mass of the puff in about the same location as the experiments with only marginal differences in the initial mass distribution. Past studies shows that these differences will not significantly alter the numerical results.<sup>15</sup>

Figure 8 displays the time evolution of the mass averaged (over the outer 24 zones) ion density during and just after the z-pinch implosion. This time period corresponds to the K-shell radiation emitting phase of the experiments. No attempt is made to simulate the experiments beyond this time duration because of uncertainties in power flow, cooling to the walls, and large scale late-time macroscopic instabilities that are present in the experiments. Results for calculations having ( $\kappa=30 \kappa_c$ ,  $\nu=49 \nu_c$ ,  $\Omega=1, 20, 50$ , and  $100 \Omega_c$ ) are shown along with results for an unaltered calculation having ( $\kappa=\kappa_c$ ,  $\nu=\nu_c$ ,  $\Omega=\Omega_c$ ). Clearly, the presence of enhanced transport dramatically reduces the average peak ion density so that it begins to approach experimental densities. The time evolution of the outer radius of the pinch, Fig. 9, also illustrates this point. The more resistive  $\Omega = 100 \Omega_c$  case has the lowest density and best phenomenological agreement with the time and spatially averaged experimental ion density. Like viscosity,

resistivity raises the internal energy of the plasma, so it is not surprising that the most resistive case produces the lowest peak ion density.

The dependence of radiative power on  $N_i$  is reflected in the total radiative power shown in Fig. 10 as well as in the K-shell power curve displayed in Fig. 11. The time integrated K-shell power appears in Fig. 12. In accord with the numerical results of the last section, these three figures illustrate the trade-off that occurs between radiation time  $\tau$  and peak K-shell power  $\dot{Y}_k$  such that the total K-shell yield remains preserved. In particular, the high density, high power, small FWHM radiation time calculation having  $(\Omega=\Omega_c, \kappa=\kappa_c, \nu=\nu_c)$  produced about the same yield as the experiments (13.6 kJ) as well as the other lower density and lower power producing  $(\nu=49 \nu_c, \kappa=30 \kappa_c)$  calculations involving  $(\Omega \leq 20 \Omega_c)$ . A number of the calculations give excellent agreement with experiment in terms of peak ion density, K-shell radiative power, and K-shell yield. However, if we were to stretch the limits of this model by further increasing the resistivity in order to match the 13 - 20 ns FWHM of the radiation pulse, then the experimental K-shell yields cannot be achieved. This is illustrated in Fig. 13 where extrapolations to higher values of resistivity results in less K-shell yield. This suggests that there are other mechanisms such as zippering or other large scale macroscopic motions, which are not effectively modeled by an average one dimensional fluid flow, occurring in the experiments that extend the time scale over which kinetic energy is thermalized.

The time evolution of the mass averaged electron temperatures, which are displayed in Fig. 13, reveals that the peak temperatures are higher than the experimentally determined time averaged (over the FWHM duration of the K-shell emission) temperature of 1660 eV for shot 2340. This difference is not that dramatic because the time averaged temperatures are ~ 2200 eV for the

$\Omega = 30 \Omega_c$  calculation and  $\sim 2600$  eV in the  $\Omega = \Omega_c$  calculation. In addition, when the same method used to determine the experimental temperature is also applied to the calculations, there can be an underestimate of the temperature. This was the case for an aluminum calculation in which the time averaged temperature was 800 eV, but the method of Coulter et al<sup>13</sup> predicted a temperature of 560 eV.

Fig. 13 also shows that the peak electron temperature is somewhat insensitive to the value of the transport coefficients. The reason for this insensitivity is because the calculations are rapidly approaching Bennett equilibrium ( $T_e \propto I^2$ ), i.e. inertial effects are minimized because a significant amount of the kinetic energy has been thermalized. Because inertial effects are more damped for viscous and resistive plasmas, their time averaged temperature should be closer to the Bennett temperature. The current is 2.3 MA for the  $(\Omega = \Omega_c, \nu = \nu_c, \kappa = \kappa_c)$  case and it is  $\sim 2.5, 2.6, 2.7$  and 2.8 MA, respectively for the  $\Omega = 1, 20, 50,$  and  $100 \Omega_c$  enhanced transport calculations at the time of peak temperature. Given these currents, and the mass averaged effective charges displayed in Fig. 14, the corresponding Bennett temperature for the  $(\Omega = \Omega_c, \nu = \nu_c, \kappa = \kappa_c)$  is 1237 eV and it is 1405, 1536, 1680, and 1833 eV, respectively for the  $\Omega = 1, 20, 50, 100 \Omega_c$  enhanced transport calculations. Indeed, the calculation with the most resistivity and viscosity does produce the best agreement between its own time averaged temperature and Bennett temperature. The experimental Bennett temperature is calculated to be  $\sim 1850$  eV based upon 2.85 MA current at the time of peak K-shell emission. Because this value is close to the time averaged temperature of 1660 eV, there is good evidence to suggest that enhanced transport is present in the experiments.

## E. CONCLUSIONS

The above considerations show that turbulence effects are capable of explaining a number of the dramatic differences that have existed between experimental observations and calculations based on classical transport. Specifically, enhanced transport can account for the lower ion densities, lower radiative powers, and longer pulse widths that have traditionally been experimentally observed but unaccounted for numerically. As mentioned in the introduction, this phenomenological work does not provide a first principles determination of the degree to which such enhanced transport exists, however, it does indicate a more rigorous evaluation of these effects is warranted that requires a strong interaction between theory and experiment.

## References

1. R. B. Spielman, D. L. Hanson, M. A. Palmer, M. K. Matzen, T. W. Hussey, and J. M. Peek, *J. Appl. Phys.* 57, 830 (1985).
2. C. Deeney, T. Nash, R.R. Prasad, L. Warren, K. G. Whitney, J. W. Thornhill, and M. C. Coulter, *Phys. Rev. A* 44, (1991).
3. J. L. Giuliani, J. E. Rogerson, C. Deeney, T. Nash, R. R. Prasad, and M. Krishnan, *J. Quant. Spectrosc. Radiat. Transfer* 44, 471 (1990).
4. J. W. Thornhill, F. Young, K. G. Whitney, S. Stephanakis, J. Davis, R. Terry, F. Cochran, "Theoretical and Experimental Comparisons of Gamble II Argon Gas Puff Experiments", *Proceedings of the Defense Nuclear Agency Advanced Pulsed Power Conference - 5-6 April 1988*, DASIAC TR-90-007
5. D. C. Colombant, M. Lampe, J. Davis, and H. W. Bloomberg, *NRL Memorandum Report* 3840.
6. J. W. Thornhill, K. G. Whitney, C. Deeney, F. C. Young, J. Davis, and S. J. Stephanakis, "One Dimensional MHD Comparisons with PRS Experimental Results", *DNA PRS Workshop* 1990.
7. M. Krishnan, C. Deeney, T. Nash, P. D. LePell and K. Childers, "Review of Z-Pinch Research at Physics International Company", *Dense Z-Pinches Second Inter. Conf.*, Laguna Beach, Ca. 1989, American Institute of Physics, New York.

8. J. Von Neumann and D. Richtmyer, *J. Appl. Phys.* **21**, 232, (1950).
9. S. I. Braginskii, "Transport Processes in a Plasma," in *Reviews of Plasma Physics*, Vol. 1, M. A. Leontovich ed., Consultants Bureau, New York, NY (1965).
10. D. Duston, R. W. Clark, J. Davis, and J. P. Apruzese, *Phys. Rev. A* **27**, 1441 (1983).
11. J. P. Apruzese, J. Davis, D. Duston, and R. W. Clark, *Phys. Rev. A* **29**, 246 (1984).
12. J. P. Apruzese, J. Davis, D. Duston, and K. G. Whitney, *J. Quant. Spectrosc. Radiat. Transfer* **23**, 479 (1980).
13. M. C. Coulter, K. G. Whitney, and J. W. Thornhill, *J. Quant. Spectrosc. Radiat. Transfer* **44**, 443 (1990).
14. K. G. Whitney, J. W. Thornhill, J. P. Apruzese, and J. Davis, *J. Appl. Phys.* **67**, 1725 (1990).
15. J. W. Thornhill, K. G. Whitney, and J. Davis, *J. Quant. Spectrosc. Radiat. Transfer* **44**, 251 (1990).

TABLE I

Shot	2338	2339	2340
Diam. (cm)	2.5	2.5	2.5
Voltage (kV)	55	55	55
Peak Current (MA)	3.0	3.2	3.1
Plemum Pressure (psi)	80	80	80
K-shell Yield (kJ)	13.0	13.8	13.6
Total Yield (kJ)	133	150	150
Implosion Time (ns)	110	120	110
Current at Implosion (MA)	2.7	2.85	2.85

TABLE I (continued)

Shot	2338	2339	2340
XRD FWHM (ns)	15	13	20
Mass ( $\mu\text{g}/\text{cm}$ )	48	65	52
Length (cm)	3.0	3.2	3.2
Time Integrated			
K-shell Diam. (mm)	4.0	3.8	4.0
Time Resolved			
K-shell Diam. (mm)	1.6	-	1.6
Time Integrated			
L-shell Diam. (mm)	-	6.8	8.0
Time Resolved			
L-shell Diam. (mm)	2.4	-	3.2

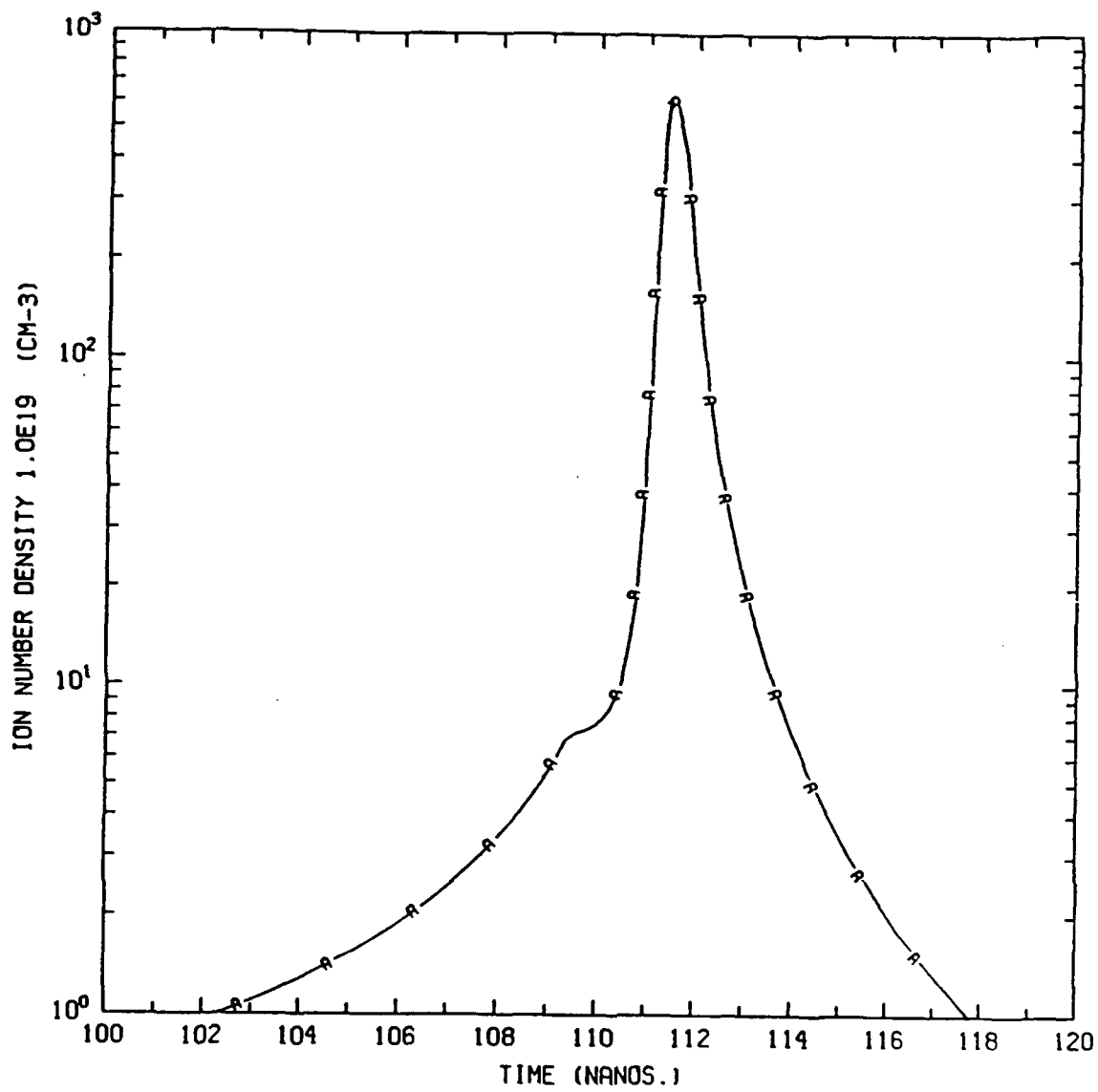


Fig. 1. Mass averaged ion density as a function of time. Only classical values of the transport coefficients are used in the calculation.

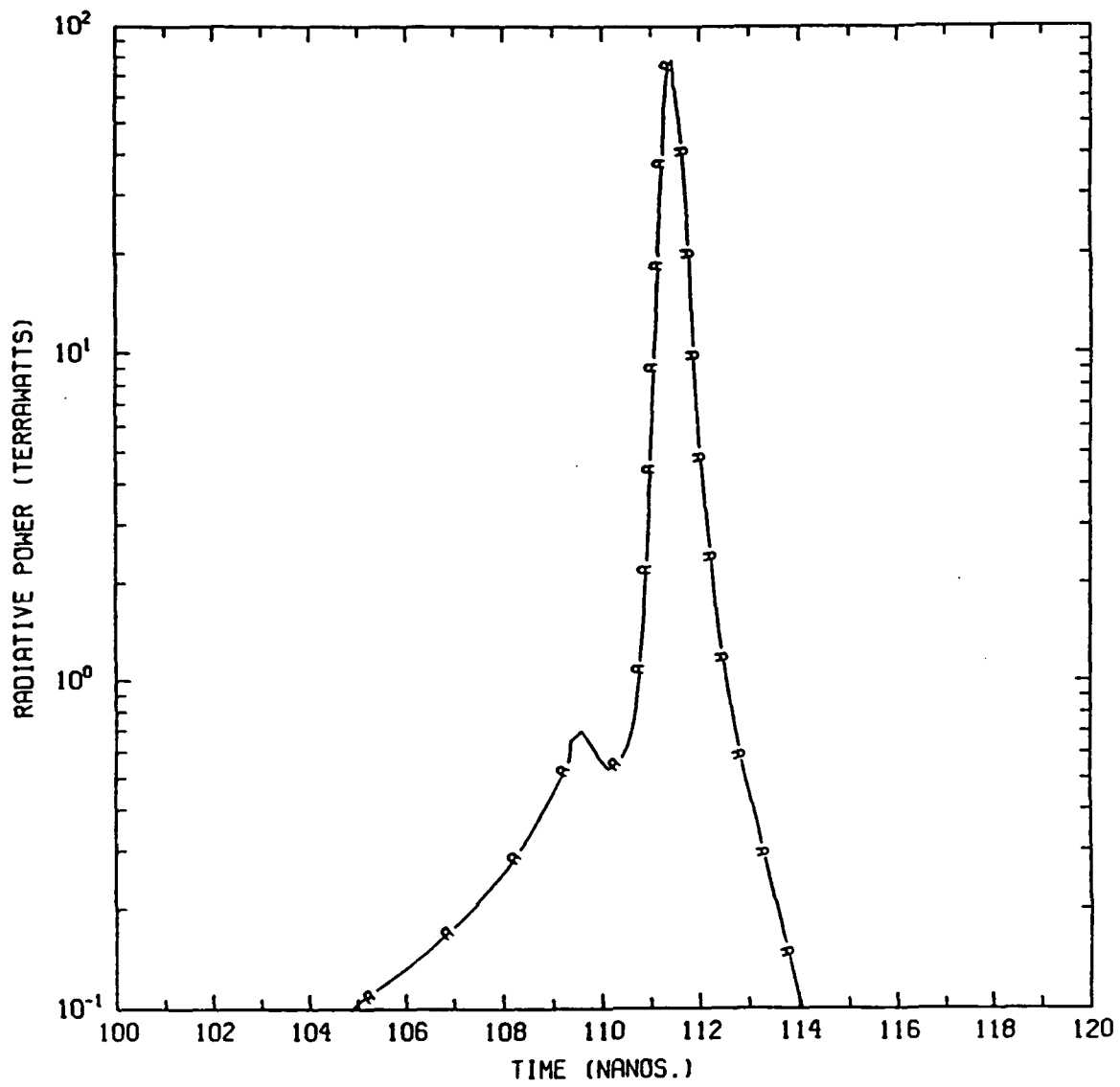


Fig. 2. Mass averaged radiative power as a function of time. Only classical values of the transport coefficients are used in the calculation.

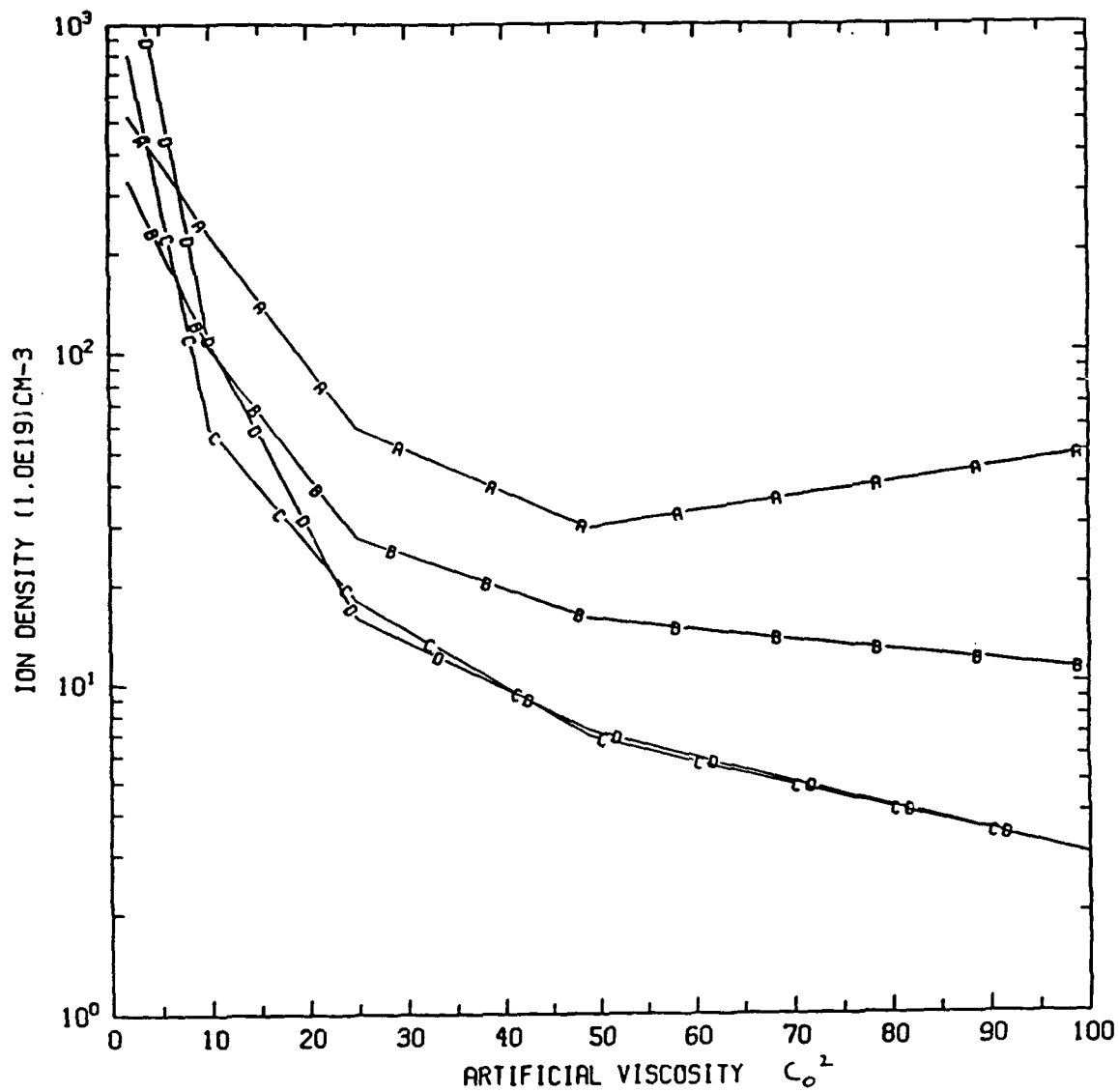


Fig. 3. Peak ion density as a function of artificial viscosity and thermal conductivity. Curve A is for  $\kappa = \kappa_c$  ( $\kappa_c$  is classical conductivity), B is for  $2 \times \kappa_c$ , C is for  $10 \times \kappa_c$ , and D is for  $30 \times \kappa_c$ . Classical values for Spitzer transverse resistivity are used to obtain these results.

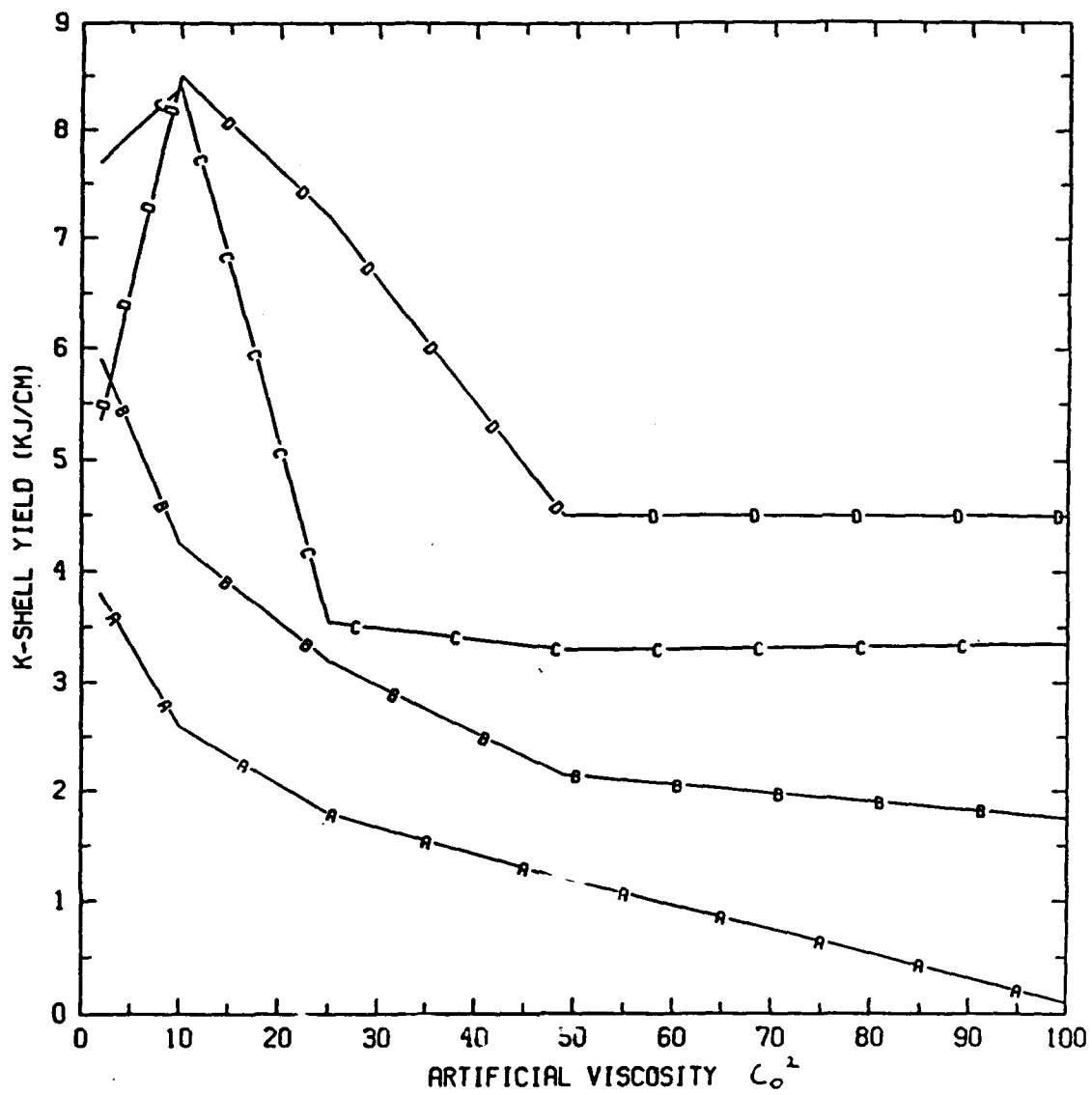


Fig. 4. K-shell yield as a function of artificial viscosity and thermal conductivity. Curve A is for  $\kappa = \kappa_c$  ( $\kappa_c$  is classical conductivity), B is for  $2 \times \kappa_c$ , C is for  $10 \times \kappa_c$ , and D is for  $30 \times \kappa_c$ . Classical values for Spitzer transverse resistivity are used to obtain these results.

# Double Eagle Circuit Diagram

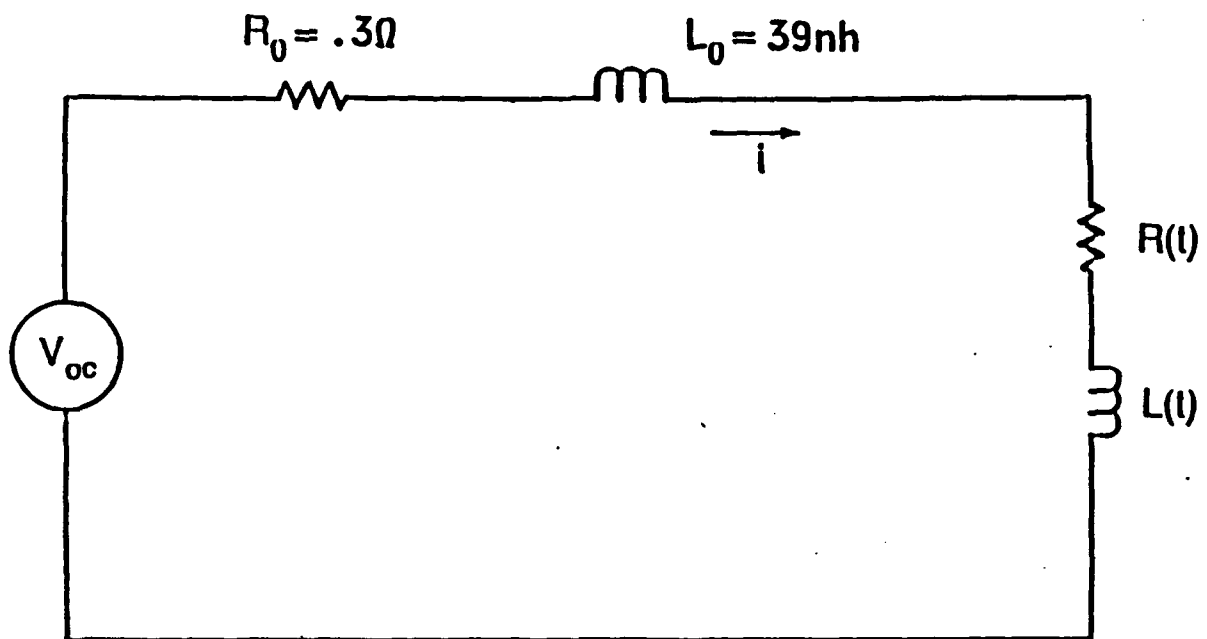


Fig. 5. Double Eagle lumped circuit diagram

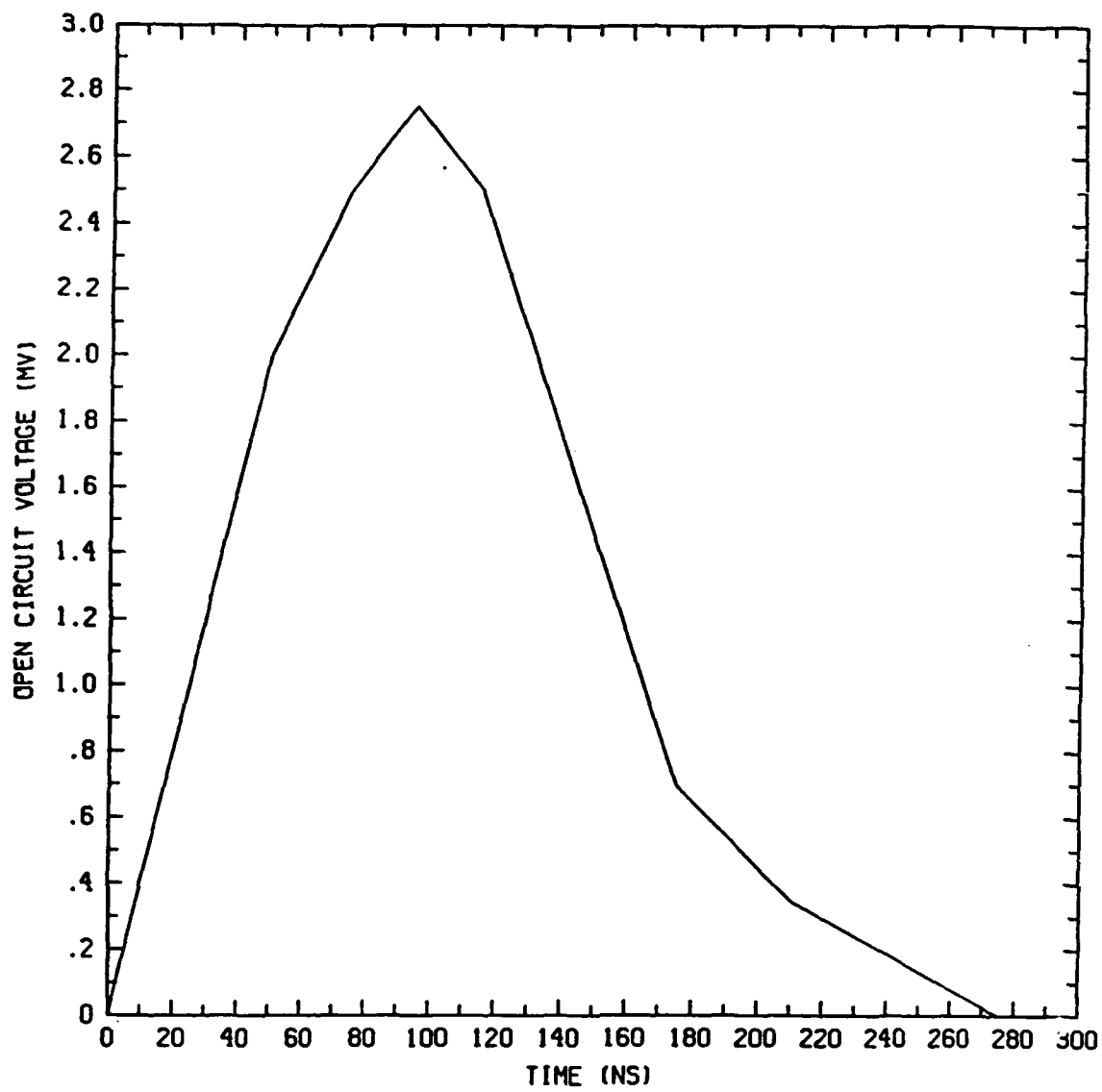


Fig. 6 Double Eagle open circuit voltage profile.

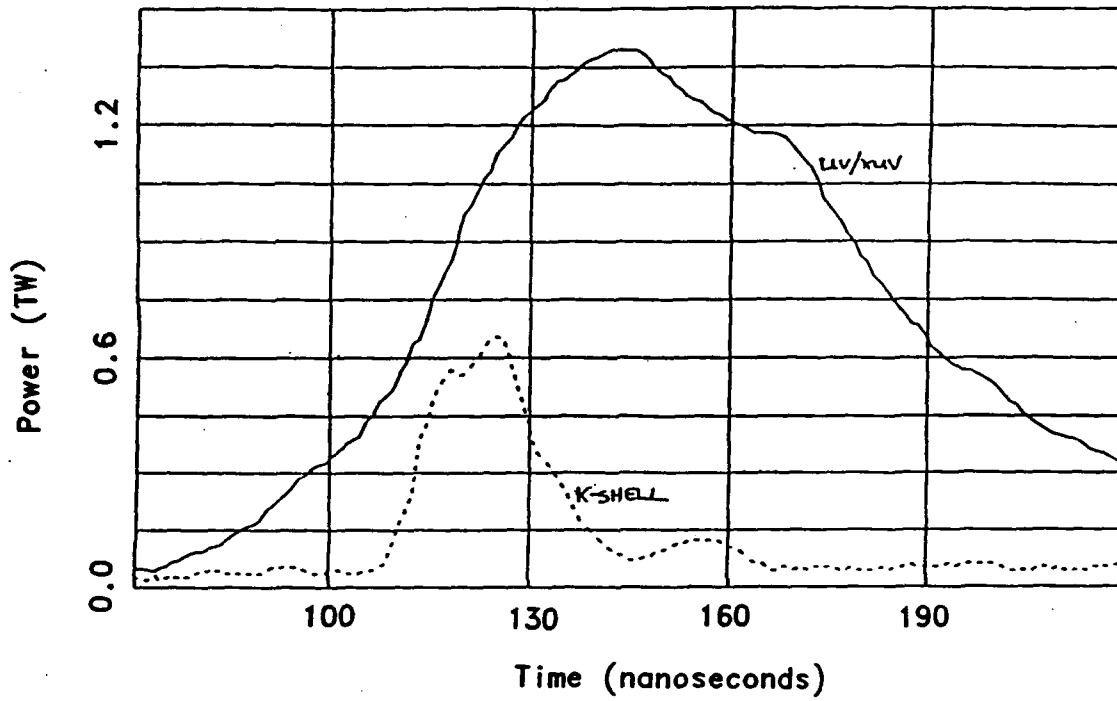


Fig. 7. Measured experimental values for total radiative power and K-shell power as a function of time for argon gas puff shot 2340.

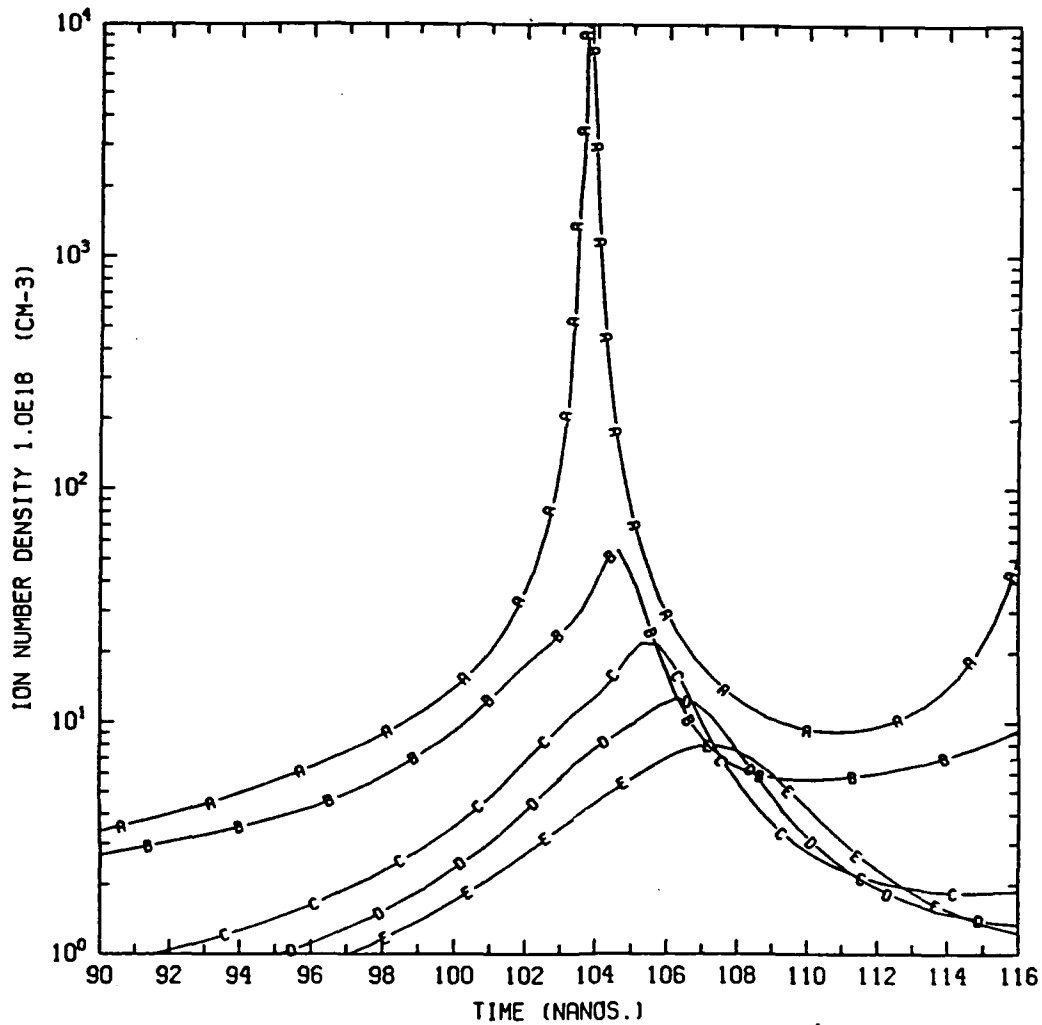


Fig. 8. Ion number density as a function of time. Results obtained using classical transport coefficients are shown in curve A. Curve B represents results obtained using Spitzer resistivity, curve C is for 20 x Spitzer resistivity, curve D is for 50 x Spitzer resistivity, and curve E is for 100 x Spitzer resistivity. A value of thermal conductivity equal to 30 x Braginskii conductivity and a value of artificial viscosity equal to 49 x Von Neumann's are used in the calculations represented by curves B - E.

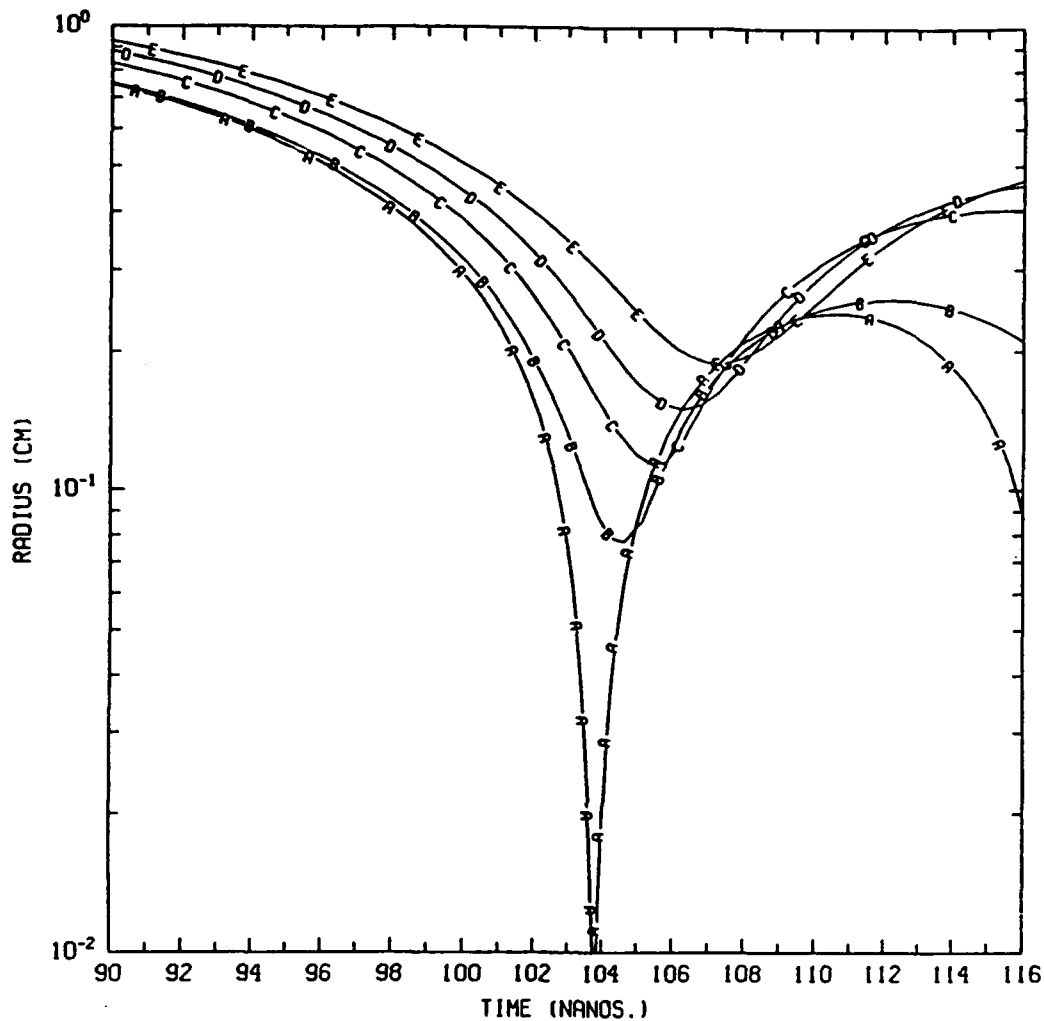


Fig. 9. Outer radius as a function of time. Results obtained using classical transport coefficients are shown in curve A. Curve B represents results obtained using Spitzer resistivity, curve C is for 20 x Spitzer resistivity, curve D is for 50 x Spitzer resistivity, and curve E is for 100 x Spitzer resistivity. A value of thermal conductivity equal to 30 x Braginskii conductivity and a value of artificial viscosity equal to 49 x Von Neumann's are used in the calculations represented by curves B - E.

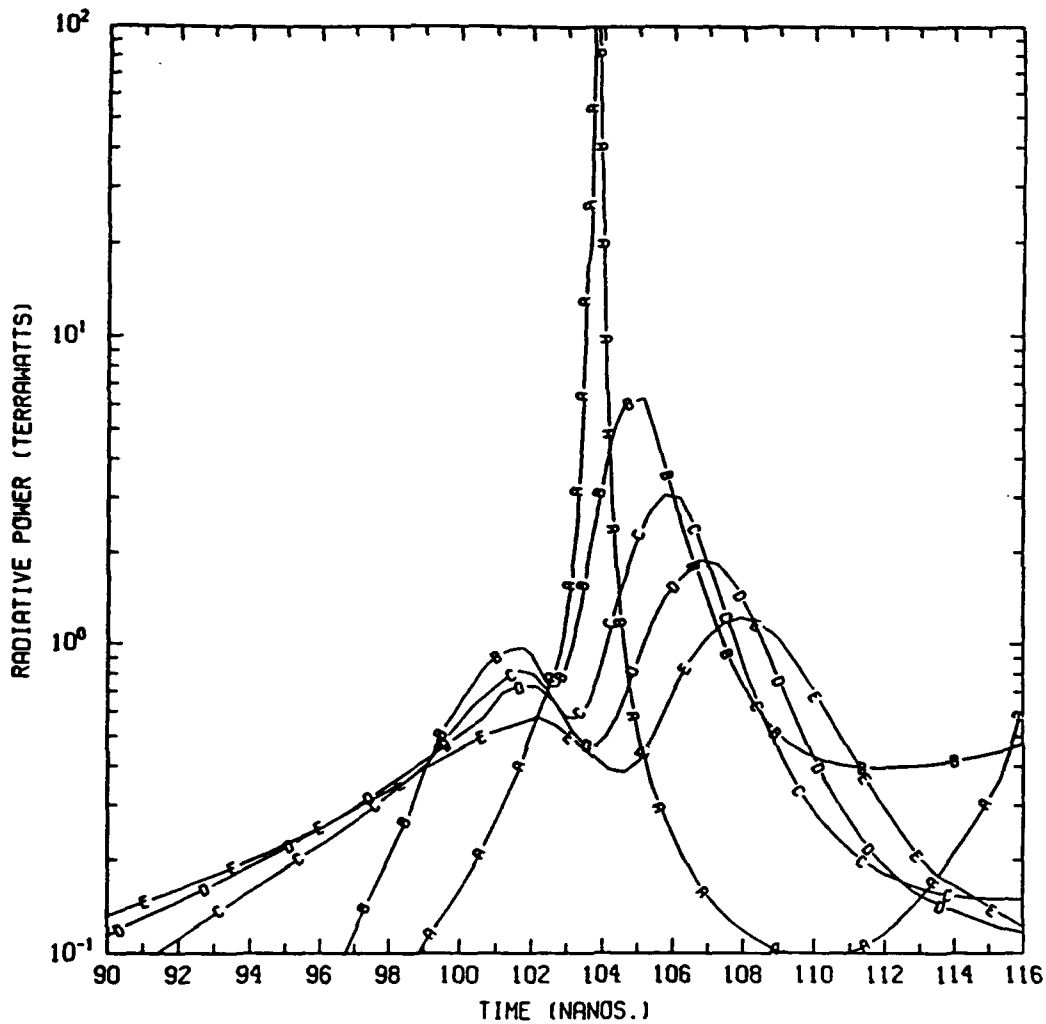


Fig. 10. Total radiative power as a function of time. Results obtained using classical transport coefficients are shown in curve A. Curve B represents results obtained using Spitzer resistivity, curve C is for 20 x Spitzer resistivity, curve D is for 50 x Spitzer resistivity, and curve E is for 100 x Spitzer resistivity. A value of thermal conductivity equal to 30 x Braginskii conductivity and a value of artificial viscosity equal to 49 x Von Neumann's are used in the calculations represented by curves B - E.

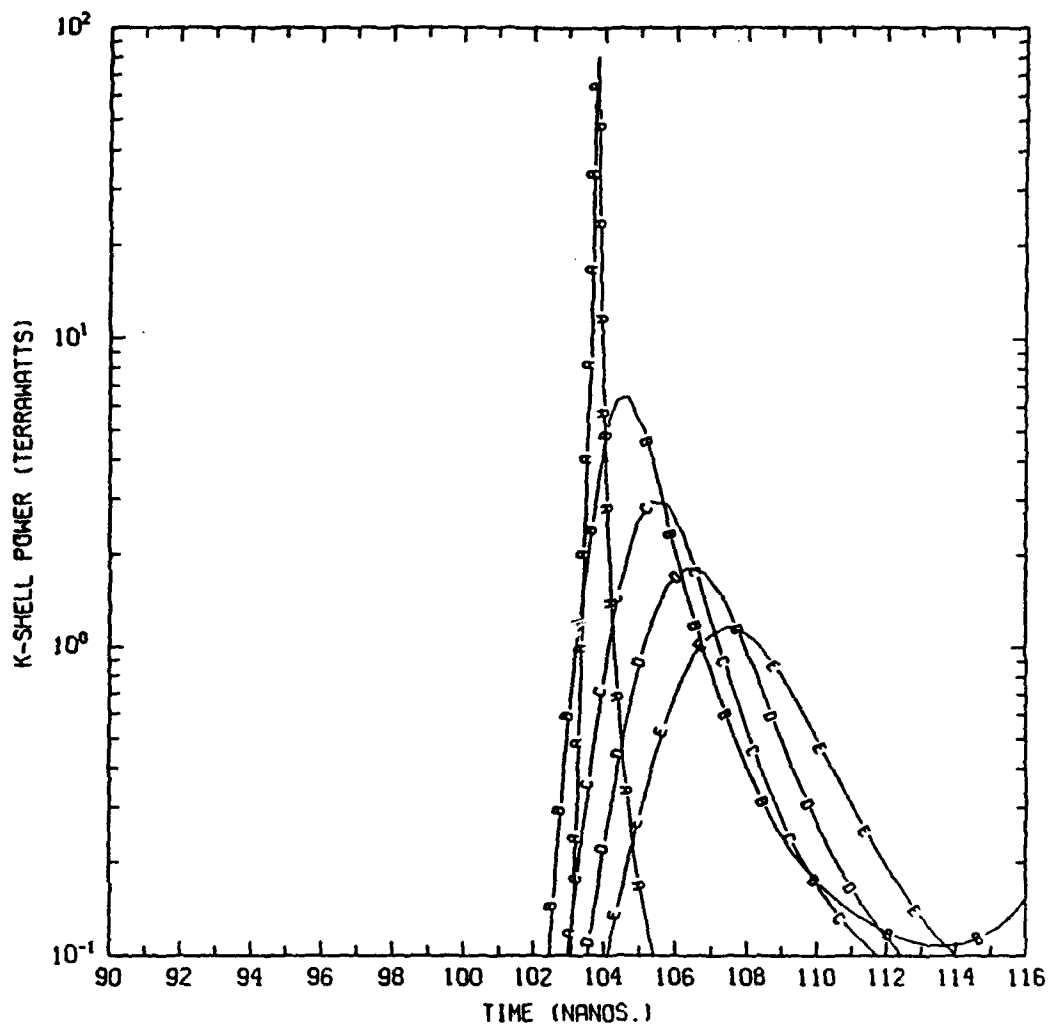


Fig. 11. K-shell radiative power as a function of time. Results obtained using classical transport coefficients are shown in curve A. Curves B represents results obtained using Spitzer resistivity, curve C is for 20 x Spitzer resistivity, curve D is for 50 x Spitzer resistivity, and curve E is for 100 x Spitzer resistivity. A value of thermal conductivity equal to 30 x Braginskii conductivity and a value of artificial viscosity equal to 49 x Von Neumann's are used in the calculations represented by curves B - E.

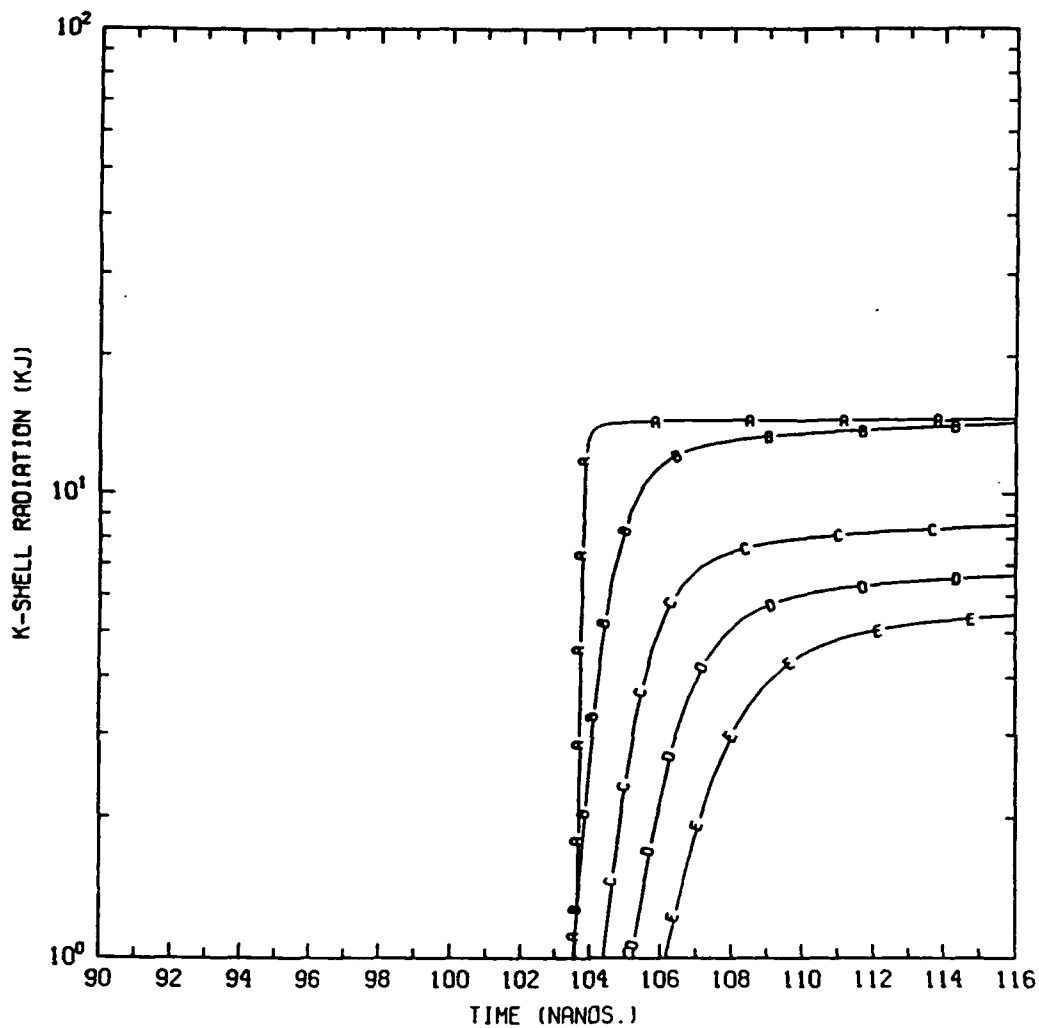


Fig. 12. K-shell yield as a function of time. Results obtained using classical transport coefficients are shown in curve A. Curves B represents results obtained using Spitzer resistivity, curve C is for 20 x Spitzer resistivity, curve D is for 50 x Spitzer resistivity, and curve E is for 100 x Spitzer resistivity. A value of thermal conductivity equal to 30 x Braginskii conductivity and a value of artificial viscosity equal to 49 x Von Neumann's are used in the calculations represented by curves B - E.

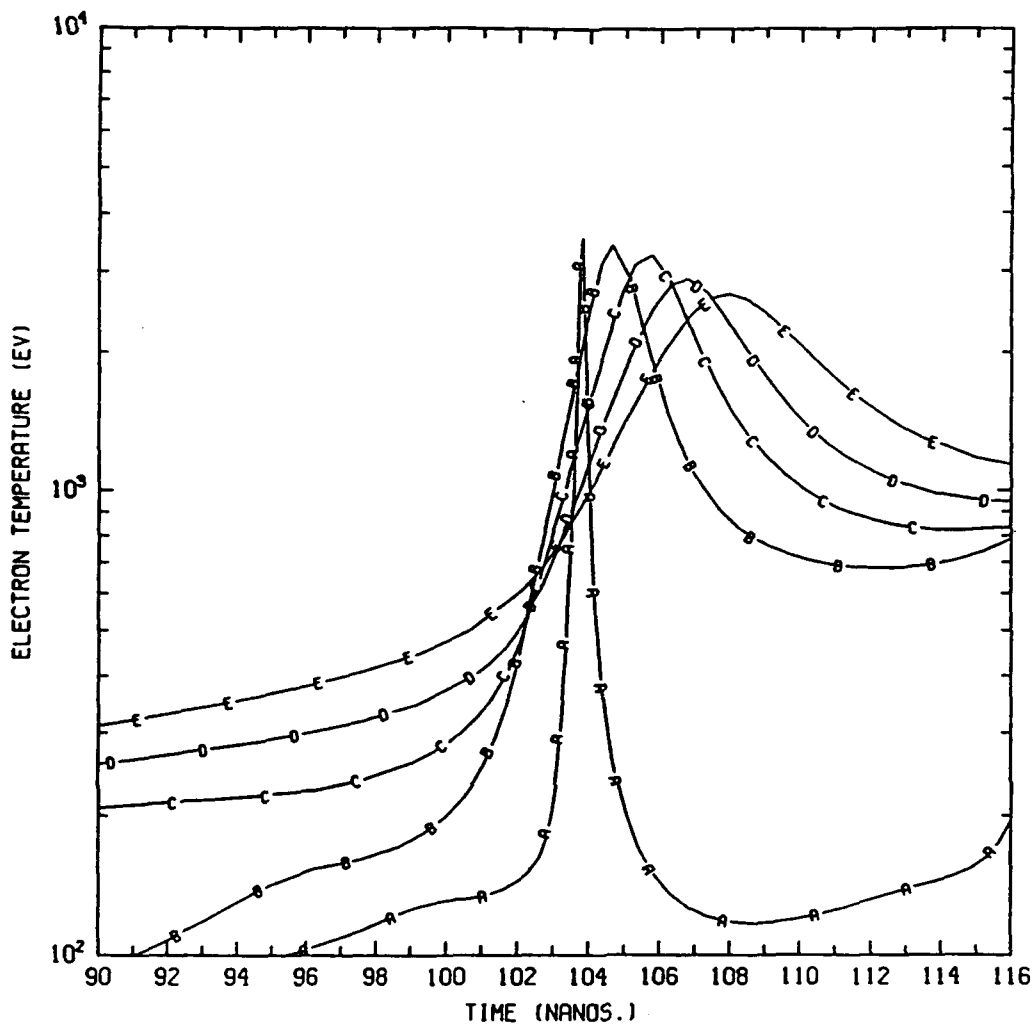


Fig. 13. Mass averaged electron temperature as a function of time. Results obtained using classical transport coefficients are shown in curve A. Curve B represents results obtained using Spitzer resistivity, curve C is for 20 x Spitzer resistivity, curve D is for 50 x Spitzer resistivity, and curve E is for 100 x Spitzer resistivity. A value of thermal conductivity equal to 30 x Braginskii conductivity and a value of artificial viscosity equal to 49 x Von Neumann's are used in the calculations represented by curves B - E.

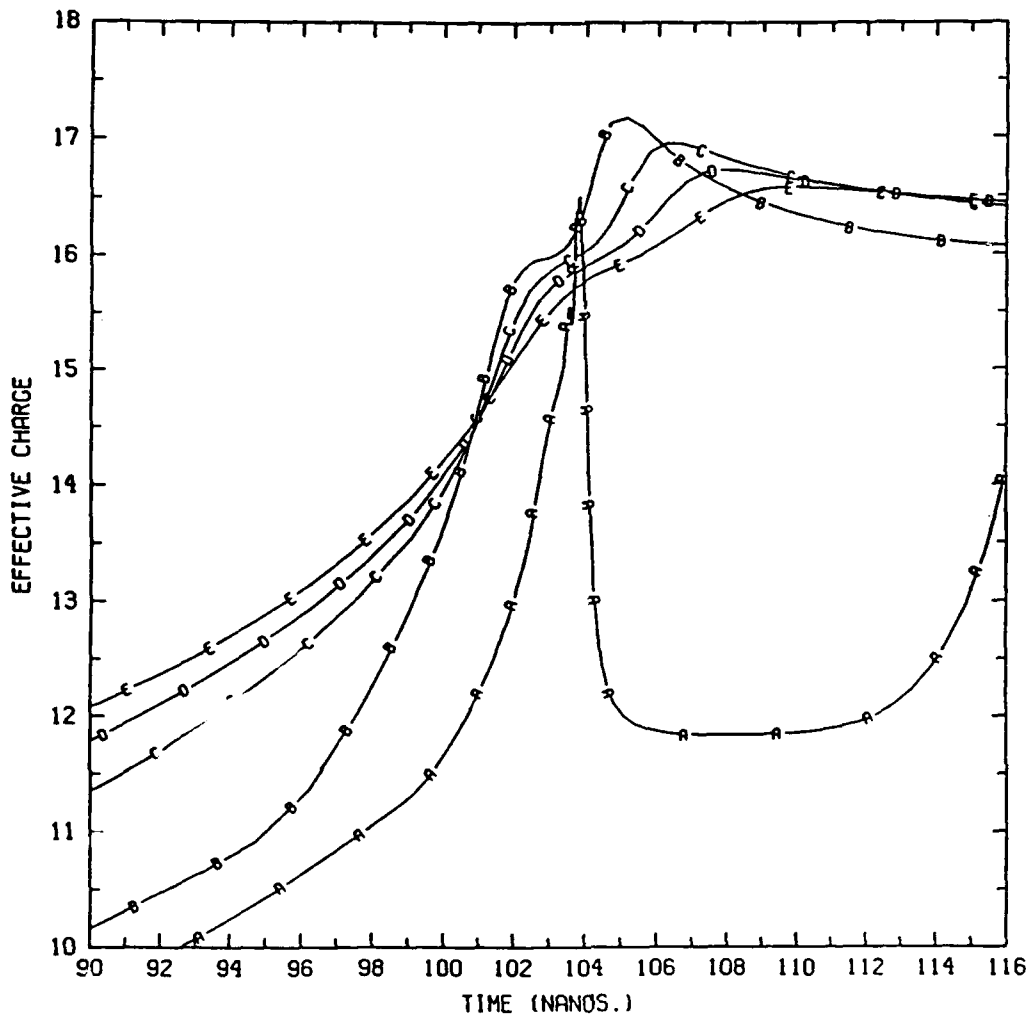


Fig. 14. Mass averaged effective charge as a function of time. Results obtained using classical transport coefficients are shown in curve A. Curves B represents results obtained using Spitzer resistivity, curve C is for 20 x Spitzer resistivity, curve D is for 50 x Spitzer resistivity, and curve E is for 100 x Spitzer resistivity. A value of thermal conductivity equal to 30 x Braginskii conductivity and a value of artificial viscosity equal to 49 x Von Neumann's are used in the calculations represented by curves B - E.

## II. Evaluating Plasma Microturbulence as a Potential Source for the Anomalous Heating of PRS Plasmas

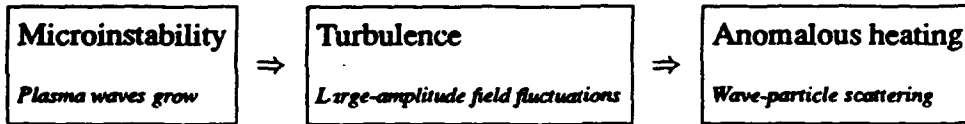
### A. Introduction

Z-pinch experiments on Double Eagle and other machines have consistently exhibited significant resistive heating, with an effective resistivity that could be two orders of magnitude greater than the Spitzer value [1]. Field penetration times into the pinch much larger than those predicted by MHD models using Spitzer resistivity can be inferred from the presence of particle acceleration phenomena like runaways; this phenomenon also points to the presence of a large plasma resistivity in the current-carrying region [2]. This anomalous resistivity is a significant factor in models to explain pinch dynamics, including pulse widths and generator-load coupling. In addition, anomalous resistivity is associated with the presence of non-Maxwellian distribution functions, which may significantly affect the dynamics of pinch radiation production and the interpretation of diagnostics. These effects are likely to be increasingly important in the planned larger, higher-power machines such as Decade. This investigation was directed towards determining and quantifying these possibilities.

We are investigating microinstability-mediated turbulence as a cause of enhanced pinch resistivity. First, we have examined typical pinch parameters to determine which microinstabilities were most likely to be present. In low-density, non-collisional pulsed-power systems like the theta pinch, plasma focus, or plasma opening switch, anomalous resistivity has been known to result typically from saturated ion-acoustic or lower-hybrid-drift microturbulence [3]. The z-pinch system has a much higher collisionality than these systems, however, and this may strongly affect the development of turbulence (including the saturation level) and its dynamical effects. Using conventional theta pinch analysis procedures, z-pinch conditions can be set up that are at least marginally favorable to a number of microinstabilities; the most important are likely to be the ion-acoustic and lower-hybrid (modified two-stream), with the former probably exhibiting the greater growth rate (about 1/100 of the pinch time).

The dynamical model we are developing is based on quasilinear theory [3]. As described below, the turbulence model provides an interaction between current-carrying electrons and

turbulent fluctuations of the plasma. Fast electron flows perturb the plasma and generate growing electrostatic waves; the turbulent waves act to scatter electrons and to reduce their mobility. The basic picture is summarized below:



The effect of turbulence is determined by its magnitude, measured by the electrostatic wave energy, and by the turbulent wave spectrum. As a first step in determining how different turbulence strengths affect the plasma resistivity and electron distribution function, we have assumed a simple spectrum of ion-acoustic turbulence. The consequences of this assumption are presented below.

The following presentation is divided into several parts. First, as motivation, we present some of the experimental evidence for anomalous heating, and sketch our model of anomalous resistivity from microinstability-mediated turbulence. Second, we summarize the properties of microinstabilities which could be present in the z-pinch plasma, and evaluate their relative importance. Third, we give a brief summary of the quasilinear kinetic theory used in our analysis. Fourth, we apply the quasilinear theory to study the ion-acoustic microinstability, using simple assumptions about the electrostatic wave spectrum. We conclude with a discussion of future work.

## B. Anomalous heating and microinstabilities

An experimental illustration of the observed anomalous heating is given in fig. (1), which contrasts observations of peak keV yield for aluminum wire array implosions on Double Eagle with theoretical predictions. Predictions are from an MHD model, assuming Spitzer resistivity and including extensive radiation transport [4]. Predicted X-ray yields are much less than observed, suggesting a much larger ohmic heating component than assumed.

A similar conclusion can be reached from performing a detailed energy balance of an implosion [1]. This is detailed below in Table 1, for a Ni wire array with mass of  $800 \mu\text{g}/\text{cm}$ , a peak current of 4 MA and measured radiation yield of 200 kJ. For the parameters in Table 1, the calculated ohmic dissipation (the last line) would be approximately 70 kJ, leading to a mean resistivity of about 0.1 ohm. This is 100 times higher than the Spitzer value.

Table 1. Energy Balance from Experiment

$\int_0^{\tau} V(t)I(t) dt =$	Total energy input to pinch ( $\approx 400$ kJ)
$L_F \int_0^{\tau} \frac{d}{dt} \left( \frac{I^2}{2} \right) dt$	Magnetic energy stored in circuit ( $\approx 160$ kJ)
$+ \frac{L_v I^2}{2} \Big _0^{\tau}$	Inductive energy stored around z-pinch ( $\approx 104$ kJ)
$+ \int_0^{\tau} \frac{I^2}{2} \left( \frac{dL_v}{dt} \right) dt$	Work done in compressing pinch plasma ( $\approx 66$ kJ)
$+ \int_0^{\tau} I^2 R dt$	Ohmic dissipation

It is attractive to imagine doing this energy balance at each instant during the implosion: The output power going into magnetic and inductive energy, radiation, and compressional work would be determined by streak camera and photomultiplier measurements and compared to the input power given by (voltage)  $\times$  (current) at the insulator stack. This power flow measurement could be combined with the plasma diagnostics to determine at each instant the magnitude of anomalous effects in the pinch. Unfortunately, such a dynamical energy balance is confounded at this time by large uncertainties, relative to the anomalous terms, in the time-resolved diagnostics. The possible presence of a short circuit in the current path [5] also introduces complications in interpretation of such time-resolved measurements. Much more reliable diagnostics exist for determining the time-integrated energy partition.

Turbulence is nonlinear and dynamic. Once the trigger conditions have been established, the turbulent state can be maintained even under the previous quiescent conditions. The turbulent oscillations tend to be damped by Coulomb collisions, and so collisional systems are not in general microturbulent. The governing parameter is the effective Reynolds number for the particular instability, which is proportional to the energy density divided by the viscous force (from Coulomb collisions). For the system to be turbulent, the effective Reynolds number should be large. The z-pinch system is fairly collisional: Coulomb collision rates typically exceed microinstability growth rates by one or two orders of magnitude. This means that relatively high levels of electrostatic

fluctuations are necessary to significantly perturb the electron distribution, and a dynamic model is needed to accurately follow the electrons' turbulent behavior.

Approximations for weak turbulence and for saturated turbulence, have been used with great success in low-density systems. The applicability of these approximations to the z-pinch must still be established, but even in those circumstances where average z-pinch conditions are not favorable to saturated microturbulence, there could still be important regions within the pinch where saturated microturbulence is extremely important. For example, a large fraction of pinch current might flow in a diffuse corona [6]; or the localized magnetic reconnection regions evident in some 2D pinch simulations [7] might have a large dynamical or radiative effect. We have focused more here on predicting the dynamical effects of developing turbulence in the bulk of the z-pinch, but our approach applies equally well to low-density regions.

### C. Survey of Instabilities

The triggering conditions and growth rates of the important instabilities depend on the background conditions in the plasma. We assume the plasma contains only two species, electrons and ions, each with separate temperature  $T_\alpha$  and density  $n_\alpha$ , where  $\alpha$  is  $e$  for electrons and  $i$  for ions. The plasma has an average ionization state  $Z = n_e/n_i$  (for generality, we also define  $Z_i = Z$ ,  $Z_e = 1$ ). For each species there is defined a plasma frequency  $\omega_{p\alpha} = \sqrt{4\pi n_\alpha (Z_\alpha e)^2 / m_\alpha}$ , and a cyclotron frequency  $\omega_{c\alpha} = Z_\alpha e B / m_\alpha c$ . In a background magnetic field, electrons and ions move in spirals with the Larmor radius  $r_{L\alpha} = v_\alpha / \omega_{c\alpha}$ , where  $v_\alpha$  is the thermal velocity. Among the important plasma parameters are the current density  $\vec{j}$ , the mean electron drift velocity  $\vec{v}_d = \vec{j} / en_e$ , the ion sound speed  $c_s = \sqrt{Z T_e / m_i}$ , and the lower hybrid frequency  $\omega_{LH} = \sqrt{\omega_{ce} \omega_{ci}}$ . Typical pinch characteristics include an implosion timescale of about 100 ns,  $\beta \equiv 8\pi n k T / B^2 \gg 1$ ,  $T_e$  and  $T_i \sim 10 - 100$  eV, and  $B \sim 10^4 - 10^5$  G. Electrons are typically magnetized, while ions are semi-magnetized, as indicated in Table 2.

The question of whether conditions are suitable for growth of microinstabilities can only be answered by looking in detail at the conditions actually present in z-pinch implosions. Unfortunately, detailed diagnostics of conditions within implosions, especially radial profiles of temperature, charge state, and electromagnetic fields, are not available. Therefore, for this analysis we have used predictions of these conditions from MHD z-pinch simulations. The MHD model

**Table 2. Typical Particle Magnetization**

Electrons	Ions
$\omega_c \sim 10^{12} \text{ sec}^{-1}$	$\omega_c \sim 10^8 \text{ sec}^{-1}$
$\omega_c \tau_{ee} \sim 1 - 10$	$\omega_c \tau_{ii} \sim 10^{-4}$
$\omega_c / \omega_p \sim 10^{-2}$	$\omega_c / \omega_p \sim 10^{-4}$
$r_{Le} \sim 10^{-4} - 10^{-3} \text{ cm}$	$r_{Li} \sim 10^{-2} - 10^{-1} \text{ cm}$

used for prediction assumes a classical Spitzer plasma resistivity, and incorporates extensive radiation transport [4]. The model is one-dimensional; radial dependence is obtained by dividing the pinch into 30 homogeneous zones, each of which is a concentric cylindrical shell. Where results are plotted, the properties of each zone are plotted individually as a function of time; this gives some idea of the radial variation of the parameters. The plotted curves are labeled with a letter (from A-Z, and then again from A-D to include all 30 zones) in order from innermost to outermost zone. Numerical results given here are for aluminum wire-array implosions; similar results, in terms of microinstability growth parameters, were obtained for titanium wire array and argon gas-puff implosions. The conditions shown here are thus "typical", and are intended to show the probable presence of microinstabilities, which will be studied in the future by the more detailed and rigorous kinetic equation analysis presented below.

The parameters important for the growth of the three most significant microinstabilities are summarized in Table 3. We now discuss the properties and prospects of each of these instabilities in an aluminum z-pinch.

The Buneman instability is driven by cold electron-ion counterstreaming. Its main effect is to reduce the current and heat the electrons. In diffuse systems, the rapid growth rate of this instability maintains conditions at marginal stability. In the dense z-pinch, the drift velocity is comparatively small, even for megagauss currents. This is shown in fig. (2), where the ratio of drift to thermal velocity is plotted for each radial zone in the pinch. Because of the skin effect, the inner zones have the smallest, and the outer zones have the highest drift velocities. The diffusion of current into the pinch can be seen in the progressive increase in drift velocity of the inner zones. The

Table 3. Summary of Surveyed Microinstabilities

Instability	Triggering Conditions	Growth Rate
Buneman	$v_d > v_e$	$\omega_p^{-1} \sim 10^{-12}$ sec.
Ion-Acoustic	$\begin{cases} v_d > c_s \\ T_e/T_i > 3/Z \end{cases}$	$\left[ \frac{\omega_{pi} v_d}{1000 c_s} \right]^{-1} \sim 10^{-9}$ sec.
Lower-Hybrid Drift	$\begin{cases} T_i \geq T_e \\ r_{Li} \frac{1}{n} \frac{dn}{dr} \gg 1 \end{cases}$	$\omega_{LH}^{-1} \sim 10^{-9}$ sec.

low magnitude of this ratio indicates that the Buneman instability is not important inside z-pinch implosions. Still, it could be a possible heating mechanism in a diffuse corona or runaway core.

The lower-hybrid drift instability is driven by ion diamagnetic drift energy perpendicular to  $\vec{B}$ . It requires large density gradients (i.e., short scale lengths), "unmagnetized" ions, and magnetized electrons. Its main effect, well-known in the theta pinch, is to broaden the current sheath and to promote field diffusion. The electrostatic wave spectrum for the instability is dominated by short wavelengths ( $k_{\perp} r_{Li} \gg 1$ ).

While changing in space and time, conditions can at times be quite favorable for growth of the lower-hybrid drift instability. In fig. (3), the ion cyclotron radius is plotted for each zone; this must greatly exceed the electron density scale length, plotted in fig. (4), for rapid microinstability growth. The other condition for growth, that the ion temperature be comparable to the electron temperature, can also be marginally satisfied, as can be seen in fig. (5), where the ratio of electron to ion temperature is plotted. For fully-developed lower-hybrid drift turbulence, a crude estimate of the anomalous resistivity is available [8]:

$$\eta_{AN} \approx 10 \frac{\omega_{ce}}{\omega_{pe} \omega_{pi}} \frac{W_0}{nkT_i}, \quad (1)$$

where in saturation the wave energy  $W_0$  can be taken to be its upper limit, namely the total directed kinetic energy

$$W_0 \approx \frac{1}{2} n_e m_e v_d^2. \quad (2)$$

The ratio between this anomalous resistivity and the Spitzer resistivity is plotted in fig. (6) for each

radial zone as a function of time. Clearly, lower-hybrid drift-generated resistivity can at times be comparable in magnitude to Spitzer resistivity.

The difficulty with assuming the lower-hybrid drift instability to be the source of z-pinch microturbulence is in the short timescale available to set up conditions favorable to the microinstability. A pinch plasma goes from having zero current and zero magnetic field to being a high-current, highly-magnetized system in a short time. The lower-hybrid drift instability model assumes that the ions are unmagnetized, a reasonable assumption on these timescales, but it also assumes that most of the current is carried by the ion diamagnetic drift, which is set up only on the (slow) timescale of the ion cyclotron frequency. In a z-pinch system, this set-up time is the same order of magnitude as the implosion time (10-100 ns). Thus, if the lower-hybrid drift instability is important during the implosion, the existing theory of this instability does not correctly describe the z-pinch system. More study is certainly needed. Still, the "traditional" lower-hybrid drift instability could be quite important in the post-stagnation pinch, where there are large gradients and strong magnetization. In fact, there is speculation that the post-stagnation pinch experiences significant ohmic heating, which would certainly contribute to the anomalous heating cited earlier which was observed in time-integrated measurements.

The ion-acoustic instability occurs when relatively hot electrons heat relatively cold ions by exciting ion sound waves. The wave phase velocity is the ion-acoustic speed  $c_s = \sqrt{ZT_e/m_i}$ . There are many varieties of ion-acoustic instability, depending on the geometry and the importance of the magnetic field [9]; in the present analysis, we confine ourselves to the simple unmagnetized ion-acoustic mode. This microinstability is likely to be present in the z-pinch: in fig. (7), the ratio of drift velocity to ion acoustic velocity is plotted, and is generally greater than one (and in some implosions can be greater than ten). The other condition for growth, that the electron temperature exceed the ion temperature, is generally satisfied (see fig. (5)), particularly at the dynamically important early times and post-stagnation times, where the plasma begins and ends its run-in and a great deal of conversion from electrical to kinetic to thermal energy takes place.

The ion-acoustic microinstability rapidly generates a large anomalous resistance (maximum resistance  $\sim 40W_0/nT\omega_{pe}$ ); then, after the electron drift velocity falls below  $c_s$ , the resistivity saturates to a smaller value. In a z-pinch implosion, this instability could be triggered at early times or near stagnation, then persist. It could be especially significant in an inner or outer corona.

Quasilinear diffusion from the ion-acoustic instability causes the ion distribution function to acquire an enhanced tail, while the tail of the electron distribution (important for radiation production) is depleted. Ion-acoustic instability-generated electron distributions have the same asymptotic form as in laser-heated plasmas [10]:

$$f_e(\epsilon) \sim e^{-(\epsilon/kT)^{m/2}} \quad (3)LAS$$

where  $m \sim 4$  to 5.

The ion-acoustic instability appears to be the most promising generator of turbulent resistivity in z-pinch implosions. Thus, while we next develop a general quasilinear theory for describing turbulent plasma heating and particle velocity-space diffusion, we will soon specialize this theory to examine more closely the effects of ion-acoustic turbulence.

#### D. Quasilinear Theory of Turbulent Resistivity

The quasilinear theory of plasma turbulence is well known [2,3]. A brief summary is presented here for clarity in explaining the present model. While its underlying assumptions have always been somewhat controversial, the quasilinear theory has been very successful in predicting the early-time growth of weak turbulence.

Quasilinear theory has the additional advantage that it can be easily integrated with the electron kinetic (Fokker-Planck) code developed by us earlier [11]. With this code, augmented by the turbulence theory presented here, we can calculate the time-evolution of the electron distribution function under the influence of the following factors:

$$\begin{aligned} \frac{df}{dt} = & \{ \text{microinstability fluctuations} \} \\ & + \{ \text{electron-electron scattering} \} \\ & + \{ \text{ohmic heating} \} \\ & + \{ \text{compressional heating} \} \\ & + \{ \text{inelastic electron-ion scattering} \} \end{aligned} \quad (4)$$

By calculating the changing electron distribution function in the system, we can determine the changing transport coefficients (e.g., electrical and thermal conductivities) that result from

assuming different levels of plasma microturbulence in a collisional z-pinch plasma. This allows us to predict the magnitude of turbulence required to explain the experimentally-observed resistivity, and to determine if the assumption of a Maxwellian electron distribution can be used in this case for accurate computation of plasma conductivities and for accurate z-pinch modeling. This kinetic model can also be used in conjunction with an MHD z-pinch model to dynamically estimate the likely strength of turbulence effects, including required modifications to transport coefficients.

In quasilinear theory, the electron distribution function  $F(\mathbf{r}, \mathbf{v}, t)$  is divided into an equilibrium part  $f(\mathbf{v}) = \langle F \rangle$  (where the angle brackets denote a spatial average) and a fluctuating part  $\delta f(\mathbf{r}, \mathbf{v}, t)$ :

$$F(\mathbf{r}, \mathbf{v}, t) = f(\mathbf{v}) + \delta f(\mathbf{r}, \mathbf{v}, t) \quad (5)$$

Macroscopic quantities like mean plasma density  $n$  and energy  $U$  are determined only by  $f(\mathbf{v})$ , but the microscopic fluctuations of these quantities are given by the moments of  $\delta f$ . In thermal equilibrium,  $\delta f \ll f$ , but when there are instabilities,  $\delta f \approx f$  is possible.

If direct interparticle interactions are ignored, the electron acceleration  $\vec{a}$  is determined only by the electric field  $\vec{E}$  and magnetic field  $\vec{B}$ , which are produced by both external sources and the average particle distribution:

$$m\vec{a} = e\vec{E} + (e/c)\vec{v} \times \vec{B}. \quad (6)$$

Like the distributions, the fields have both fluctuating and average components; in a neutral plasma, the average components can come only from external sources, while the fluctuations come from other particles. Below, we assume zero background magnetic field ( $\vec{B} = 0$ ), and examine only the simplest case of electrostatic fluctuations ( $\delta\vec{B} = 0$ ).

With these assumptions, the full electron distribution function  $F(\mathbf{r}, \mathbf{v}, t)$  obeys the Vlasov equation. Averaging this equation gives the "quasilinear" relation satisfied by  $f(\mathbf{v})$ :

$$\frac{\partial f}{\partial t} + \langle \vec{a} \rangle \cdot \vec{\nabla}_v f = - \langle \delta\vec{a} \cdot \vec{\nabla}_v \delta f \rangle, \quad (7)$$

while subtracting this average equation from the full equation and neglecting terms second-order in the fluctuations gives the linear relation satisfied by  $\delta f$ :

$$\left[ \frac{\partial}{\partial t} + \vec{v} \cdot \vec{\nabla} + \langle \vec{a} \rangle \cdot \vec{\nabla}_v \right] \delta f(\mathbf{r}, \mathbf{v}, t) = -\delta\vec{a} \cdot \vec{\nabla}_v f(\mathbf{v}). \quad (8)$$

Eq. (8) is in the same form as the linearized Vlasov equation.

In the electrostatic approximation, the fluctuating electron distribution  $\delta f$  produces fluctuating electric fields  $\delta E$  (waves), determined from Poisson's equation:

$$\vec{\nabla} \cdot \vec{\delta E}(\mathbf{r}, t) = 4\pi \int d^3v \delta f(\mathbf{r}, \mathbf{v}, t). \quad (9)$$

The fluctuating electric field acts on the average distribution  $f(\mathbf{v})$  to generate further fluctuations  $\delta f(\mathbf{r}, \mathbf{v})$ , given by eq. (8). The fluctuating densities and fields then interact nonlinearly to heat the plasma, via eq. (7). This is the picture of turbulent heating sketched out above, where microinstability leads to turbulence, which results in anomalous heating.

The evolution of the average distribution function can readily be determined by Fourier transforming, solving eq. (8) for  $\delta f(\mathbf{k}, \mathbf{v}, t)$ , and substituting this into eq. (7). The result is a diffusion equation identical in form to the Fokker-Planck equation:

$$\frac{\partial f}{\partial t} + \langle \vec{a} \rangle \cdot \vec{\nabla}_v f = \vec{\nabla}_v \cdot [\mathcal{D} \cdot \vec{\nabla}_v f] \quad (10)$$

where the diffusion tensor is

$$D_{ij} = \frac{8\pi^2 e^2}{m^2} \int d^3k \frac{k_i k_j}{k^2} W(\mathbf{k}) \delta(\omega(\mathbf{k}) - \vec{k} \cdot \vec{v}), \quad (11)$$

and  $W(\mathbf{k})$  is the electrostatic wave energy density, defined such that

$$\int d^3k W(\mathbf{k}) = \langle \delta E^2 \rangle / 4\pi. \quad (12)$$

The electrostatic wave energy density determines, among other things, the anomalous heating rate:

$$\left( \frac{dU}{dt} \right)_{AN} \sim \frac{\omega_p^2}{U^{3/2}} W(\mathbf{k}). \quad (13)$$

It can be measured spectroscopically through its direct proportionality to the density correlation function  $S(\mathbf{k}) \sim \langle \delta n(\mathbf{k}) \delta n(-\mathbf{k}) \rangle$ , and through the increased opacity associated with turbulence.

The wave energy spectrum is initially thermal, and then it grows or damps with the density fluctuations. The spectrum of fluctuations  $\delta f(\vec{k}, \omega)$  evolves on a rapid timescale according to eq. (8). The normal modes of the fluctuating system and growth or damping rates are given by the complex frequencies  $\omega(\vec{k})$  that satisfy the dispersion equation

$$1 + \frac{1}{k^2} \int \frac{\omega_{pe}^2 \vec{k} \cdot \vec{\nabla} f_e(v) + \omega_{pi}^2 \vec{k} \cdot \vec{\nabla} f_i(v)}{\omega - \vec{k} \cdot \vec{v}} d^3v = 0, \quad (14)$$

where both electron and ion distributions ( $f_e, f_i$ ) contribute. The electrostatic energy density evolves from the initial (thermal) level according to:

$$W(\vec{k}, t) = W(\vec{k}, 0) e^{2 \int_0^t dt' \Gamma(\vec{k}, t')} \quad (15)$$

where the growth (damping) rate  $\Gamma(\vec{k})$  is the imaginary part of  $\omega(\vec{k})$ ; in principle,  $W(\vec{k}, t)$  can be determined by solving the dispersion relation in the evolving system and applying eq. (15).

In practice, because of the difficulties in solving for the dispersion relation, the electrostatic energy spectrum is often approximated, by, e.g., an isotropic spectrum, a delta function at the fastest-growing wavenumber, or a power-law spectrum such as those known to apply in other systems with fully-developed turbulence. The asymptotic, small- $k$  (Kolmogorov) spectrum is given by

$$W(k) \sim (nT) k^{-3a} \quad (16)$$

where  $a$  measures turbulence strength:  $a = 0$  for quiescent plasmas,  $a = 1$  for strongly turbulent plasmas. The spectrum is often strongly directional, and assumptions must be made about dependence on both magnitude and direction of  $\vec{k}$ .

### E. Ion-Acoustic Turbulent Diffusion

If the turbulent spectrum  $W(\vec{k})$  is isotropic, the integral in eq. (11) can be evaluated in a frame where  $\vec{v} = v\hat{z}$ . Because the survey of instabilities given in this report indicates that the ion-acoustic instability is probably quite important, the turbulent diffusion tensor is now evaluated for this microinstability. If we take an acoustic mode with sound velocity  $c_s$ , so that  $\omega(\vec{k}) = |k|c_s$ , the delta function in eq. (11) is

$$\delta(\omega(\vec{k}) - \vec{k} \cdot \vec{v}) = \begin{cases} \frac{\delta(\theta - \theta_i)}{|kv \sin \theta_i|} & \text{if } v > c_s \\ 0 & \text{if } v < c_s \end{cases} \quad (17)$$

where

$$\theta_i \equiv \cos^{-1} \left( \frac{c_s}{v} \right). \quad (18)$$

In this case, if we define

$$\Omega \equiv 4\pi \int dk k W(k) \quad (19)$$

then  $\mathcal{D} = 0$  when  $v < c_s$  and

$$\mathcal{D} = \frac{2\pi^2 e^2 \Omega}{m_e^2 v} \begin{pmatrix} 1 - c_s^2/v^2 & 0 & 0 \\ 0 & 1 - c_s^2/v^2 & 0 \\ 0 & 0 & 2c_s^2/v^2 \end{pmatrix} \quad (20)$$

when  $v > c_s$ .

Because the integral was carried out in spherical coordinates with the axis along  $\vec{v}$ , the diffusion tensor has diagonal elements  $\mathcal{D}_{\theta\theta}$ ,  $\mathcal{D}_{\phi\phi}$ ,  $\mathcal{D}_{vv}$ , in this order. To evaluate the turbulent diffusion term, we assume that the distribution function can be represented by a Cartesian-tensor expansion:

$$f(\vec{v}) = f_0(v) + \hat{v} \cdot \vec{f}_1. \quad (21)$$

With the diffusion tensor in eq. (20) and the expansion of eq. (21), the right-hand side of eq. (10) becomes (for  $v > c_s$ ):

$$\vec{\nabla}_v \cdot [\mathcal{D} \cdot \vec{\nabla}_v f] = \frac{4\pi^2 e^2 \Omega}{m_e^2 v^2} \left\{ \frac{\partial}{\partial v} \left[ \frac{c_s^2}{v} \frac{\partial f(\vec{v})}{\partial v} \right] - \frac{1}{v} \gamma \hat{v} \cdot \vec{f}_1 \right\} \quad (22)$$

where

$$\gamma \equiv 1 - \frac{c_s^2}{v^2}. \quad (23)$$

This contributes to both the zero-order (scalar) and first-order (vector) equations in the Cartesian tensor expansion of the Vlasov equation [11]:

$$\vec{\nabla}_v \cdot [\mathcal{D} \cdot \vec{\nabla}_v f]^{(0)} = \frac{4\pi^2 e^2 \Omega c_s^2}{m_e^2 v^2} \frac{\partial}{\partial v} \left( \frac{1}{v} \frac{\partial f_0}{\partial v} \right) \quad (v > c_s) \quad (24a)$$

$$\vec{\nabla}_v \cdot [\mathcal{D} \cdot \vec{\nabla}_v f]^{(1)} = \frac{4\pi^2 e^2 \Omega}{m_e^2 v^2} \left\{ \frac{\partial}{\partial v} \left( \frac{c_s^2}{v} \frac{\partial \vec{f}_1}{\partial v} \right) - \frac{\gamma}{v} \vec{f}_1 \right\} \quad (v > c_s) \quad (24b)$$

The zero-order ion-acoustic diffusion expression in eq. (24a) is identical in form to the ohmic-heating term found for laser-heated plasmas [10] or for strong-magnetic field heating of z-pinch plasmas [11], and so it can be expected to amplify these effects. As an illustration of the behavior of a system with turbulence, the electron kinetic model described earlier [11] was used to obtain the time-evolution of the average electron distribution function and over plasma parameters (average energy, current density, and effective resistivity) when a small electric field is applied to a plasma with a fixed level of turbulence:  $4\pi^2 e^2 \Omega c_s^2 / m_e^2 = 0.1$ . These quantities are plotted in fig. (8)–fig. (11). The turbulence had a pronounced effect on both distribution functions and plasma properties. Note that the depleted-tail self-similar form for the distribution function predicted in eq. (\*) is indeed present.

## F. Conclusions

The ion-acoustic instability was identified as the most promising candidate for immediate investigation to study z-pinch anomalous heating. When a simple (isotropic) spectrum was assumed for ion-acoustic turbulent heating, a significant modification in both plasma resistivity and electron distribution functions was observed.

The work reported here is oriented towards answering a specific set of questions regarding the relevance and importance of microturbulence to PRS dynamics. It has limitations, which will be remedied in the future. First, magnetic field effects have been neglected. This is not a serious limitation in the bulk of the pinch, but in the edge or corona, the magnetic field should be significant. Second, directional dependence of wave fluctuations will need to be included (the ion-acoustic turbulent spectrum reportedly [12] peaks in a cone 20-30 degrees from the drift velocity). Finally, the results presented here are not yet self-consistent, because the fluctuation energy was not yet considered to change with changes in the particle energy and distribution function shape. This could make our present results not energy-conserving. For realistic modeling, we will need to incorporate self-consistent solutions of the dispersion for the evolving particle distribution. The computationally feasible way to accomplish this is to expand the distribution function in terms of the energy, e.g., in a polynomial expansion [13,14]. This will be a particular focus of work in the coming year.

## REFERENCES

1. M. Krishnan, "PRS - A critical assessment," Physics International Company Report Pitr 3992-01 (1989).
2. NRL Plasma Radiation Branch, "Advanced concepts theory annual report 1990," NRL Memorandum Report 6870 (1991), pp. 86-105.
3. R.C. Davidson and N.A. Krall, "Anomalous transport in high-temperature plasmas with applications to solenoidal fusion systems," Nucl. Fusion 17:1313 (1977).
4. "TRIHYP"; cf. J.W. Thornhill, J.L. Giuliani and J.P. Apruzese, Bull. Am. Phys. Soc. 33:1920 (1988).
5. NRL Plasma Radiation Branch, "Advanced concepts theory annual report 1990," NRL Memorandum Report 6870 (1991), pg. 28ff.
6. NRL Plasma Radiation Branch, "Advanced concepts theory annual report 1989," NRL Memorandum Report 6612 (1990), pp. 80-99; P.E. Pulsifer, K.G. Whitney and J.W. Thornhill, "The coronal current channel in an exploding-wire z-pinch," Bull. Am. Phys. Soc. 34:1944 (1989).
7. NRL Plasma Radiation Branch, "Advanced concepts theory annual report 1990," NRL Memorandum Report 6870 (1991), pp. 106-112.
8. Ronald C. Davidson, *Nobel symposium on nonlinear effects in plasmas*, Lerum, Sweden (1976).
9. M. Lampe, W.M. Manheimer and K. Papadopoulos, "Anomalous transport coefficients for HANE applications due to plasma micro-instabilities," NRL Memorandum Report 3076 (1975).
10. A.B. Langdon, Phys. Rev. Lett. 44:575 (1980).
11. P.E. Pulsifer and K.G. Whitney, "Non-Maxwellian electron distribution functions in z-pinch plasmas," NRL Memorandum Report 6662 (1990).
12. D. Biskamp, R. Chodura and C.T. Dum, Phys. Rev. Lett. 34:131 (1975).
13. Robert S. Cohen, Lyman Spitzer and Paul McR. Routly, "The electrical conductivity of an ionized gas," Phys. Rev. 80:230 (1950).
14. N.J. Fisch, "Conductivity of rf-heated plasma," Phys. Fluids 28:245 (1985).

## Figure Captions

1. Radiative yield for aluminum wire array implosions on Double Eagle. Shown are peak X-ray production in kJ, as a function of array radius. Experimentally observed yields (diamond symbol) are much greater than predictions from a Spitzer-resistivity-based MHD model (circular symbol).
2. Ratio of drift velocity to thermal velocity in an aluminum wire array implosion, based on MHD simulation. Each curve is a graph of the time-dependence of one of 30 cylindrical shells, labeled from A-Z, then A-D, from inside out. Innermost shells have the lowest velocity.
3. Ion cyclotron radius (in cm) as a function of time for each radial zone. See fig. (2) caption for description of zones. Innermost zones have the largest cyclotron radius.
4. Electron density scale length (in cm), defined as  $[(1/n)d \log n/dr]^{-1}$ , as a function of time. See fig. (2) caption for description of zones.
5. Ratio of electron temperature to ion temperature as a function of time, for each radial zone. See fig. (2) caption for description of zones.
6. Ratio between maximum anomalous resistivity from lower-hybrid drift turbulence and classical Spitzer resistivity, for the plasma conditions at each radial zone as a function of time. See fig. (2) caption for description of zones.
7. Ratio between electron drift velocity and ion acoustic velocity, for each radial zone, as a function of time. See fig. (2) caption for description of zones.
8. Evolution of the electron distribution function as a function of time, under the influence of a small constant electric field, and with a small fixed amplitude of ion-acoustic turbulence. Each curve is the average, isotropic distribution function as a function of velocity at a given time.

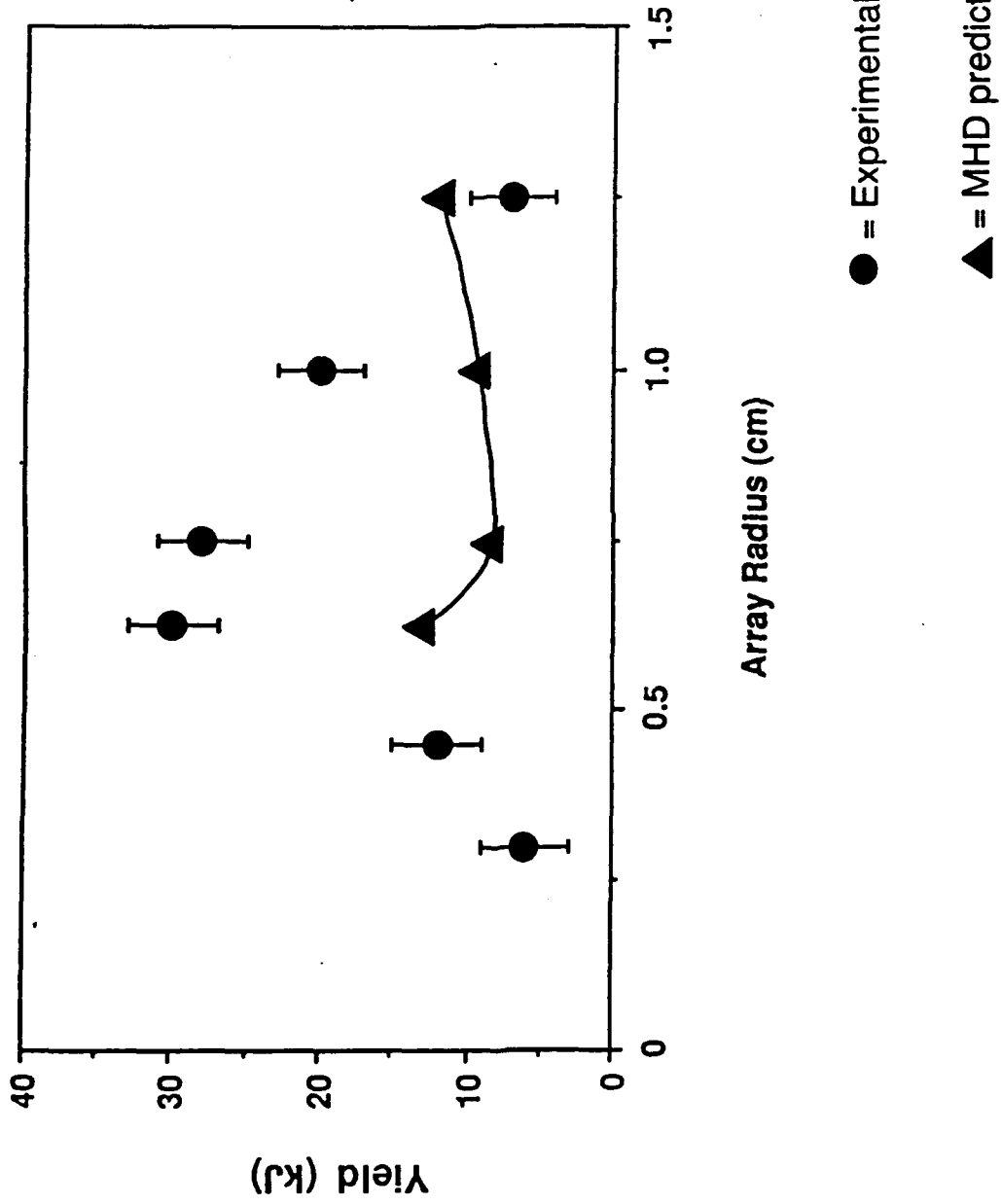
Successively later curves are labeled A, B, C, etc.

9. Average plasma energy as a function of time, under the same conditions as in fig. (8).

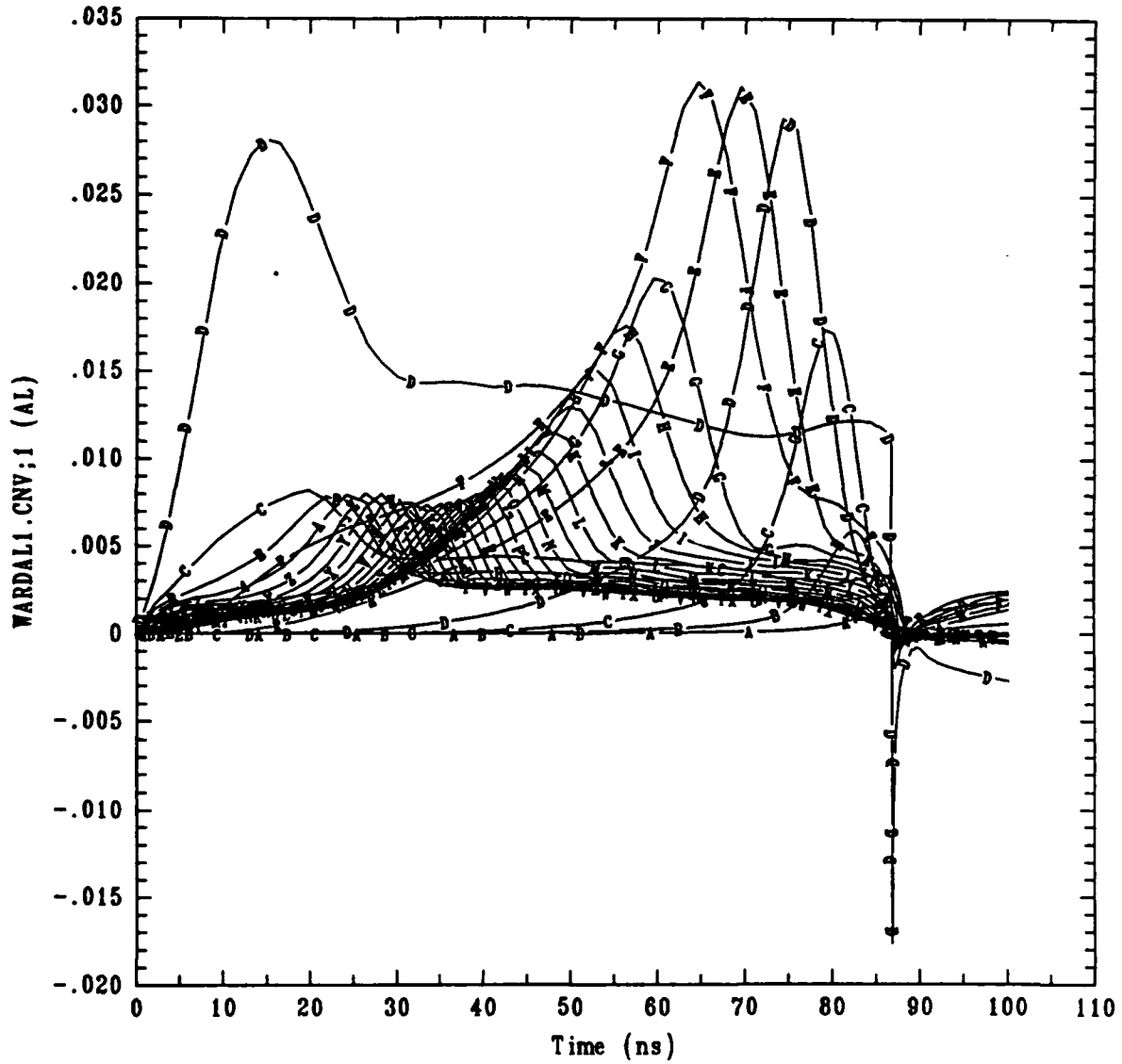
10. Current density as a function of time, under the same conditions as in fig. (8).

11. Effective resistivity of the plasma under the conditions of fig. (8): plotted is ratio of the calculated resistivity and the Spitzer resistivity.

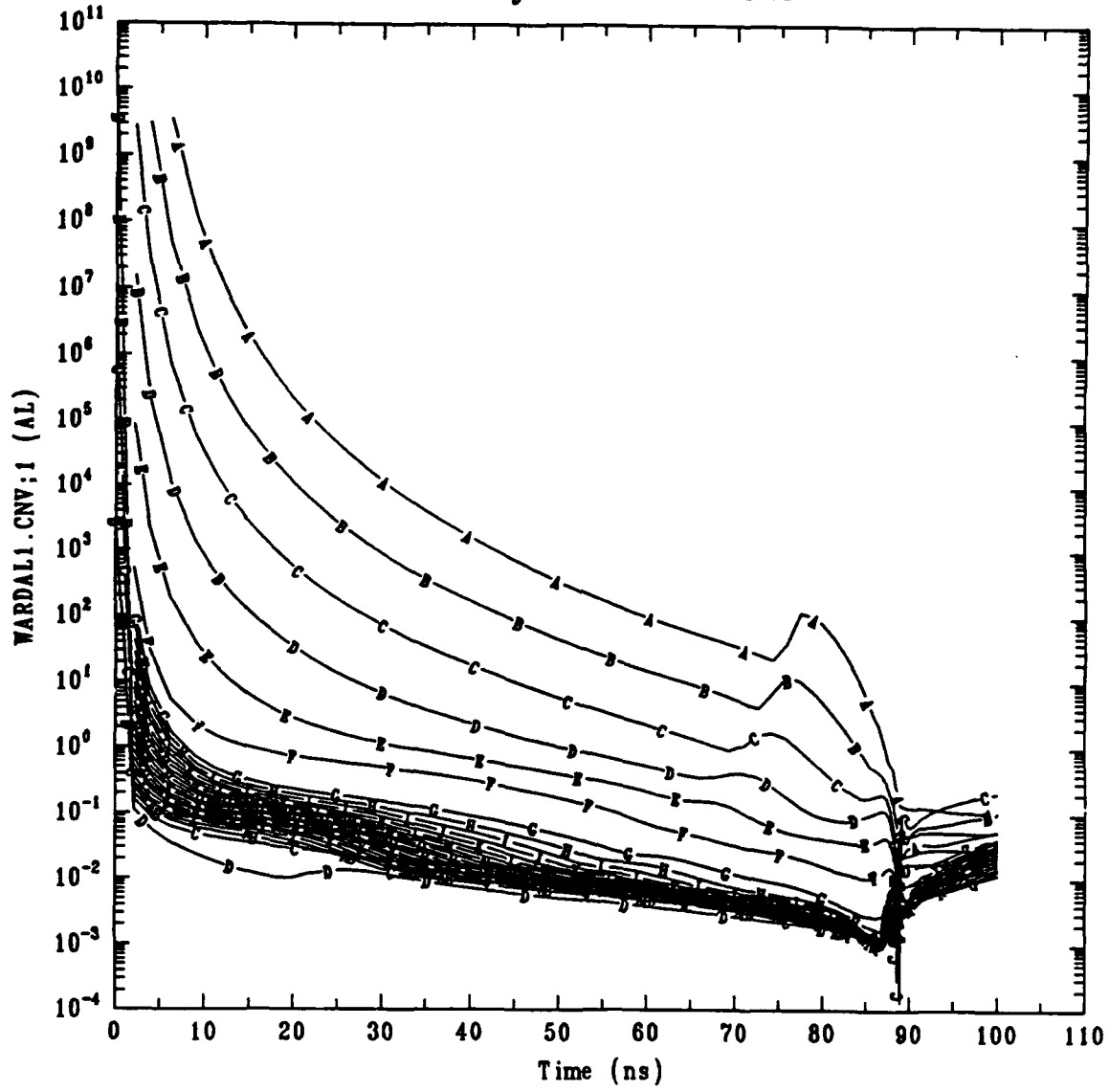
# Al wire array results on Double-Eagle



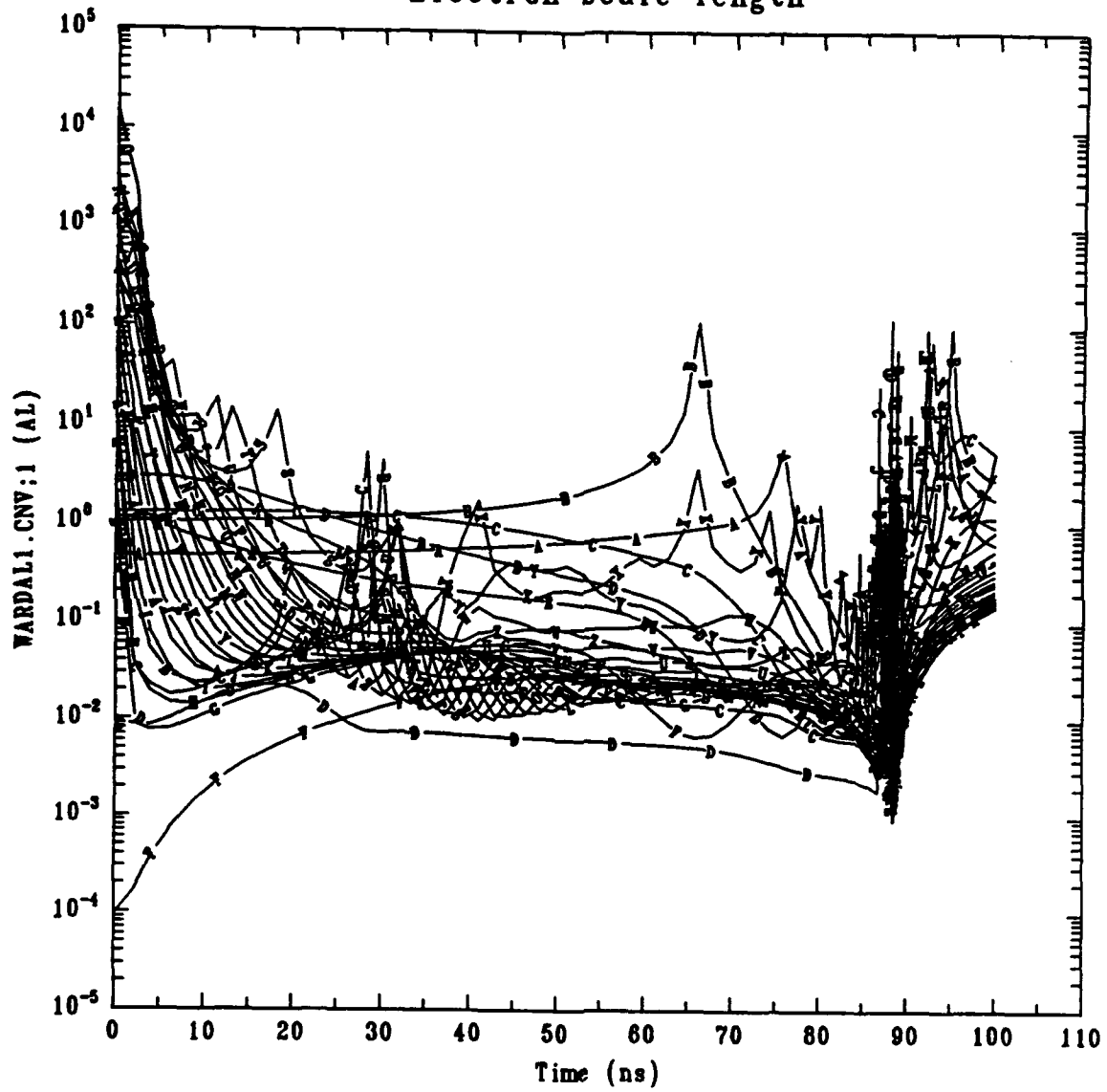
### Drift/Thermal velocity



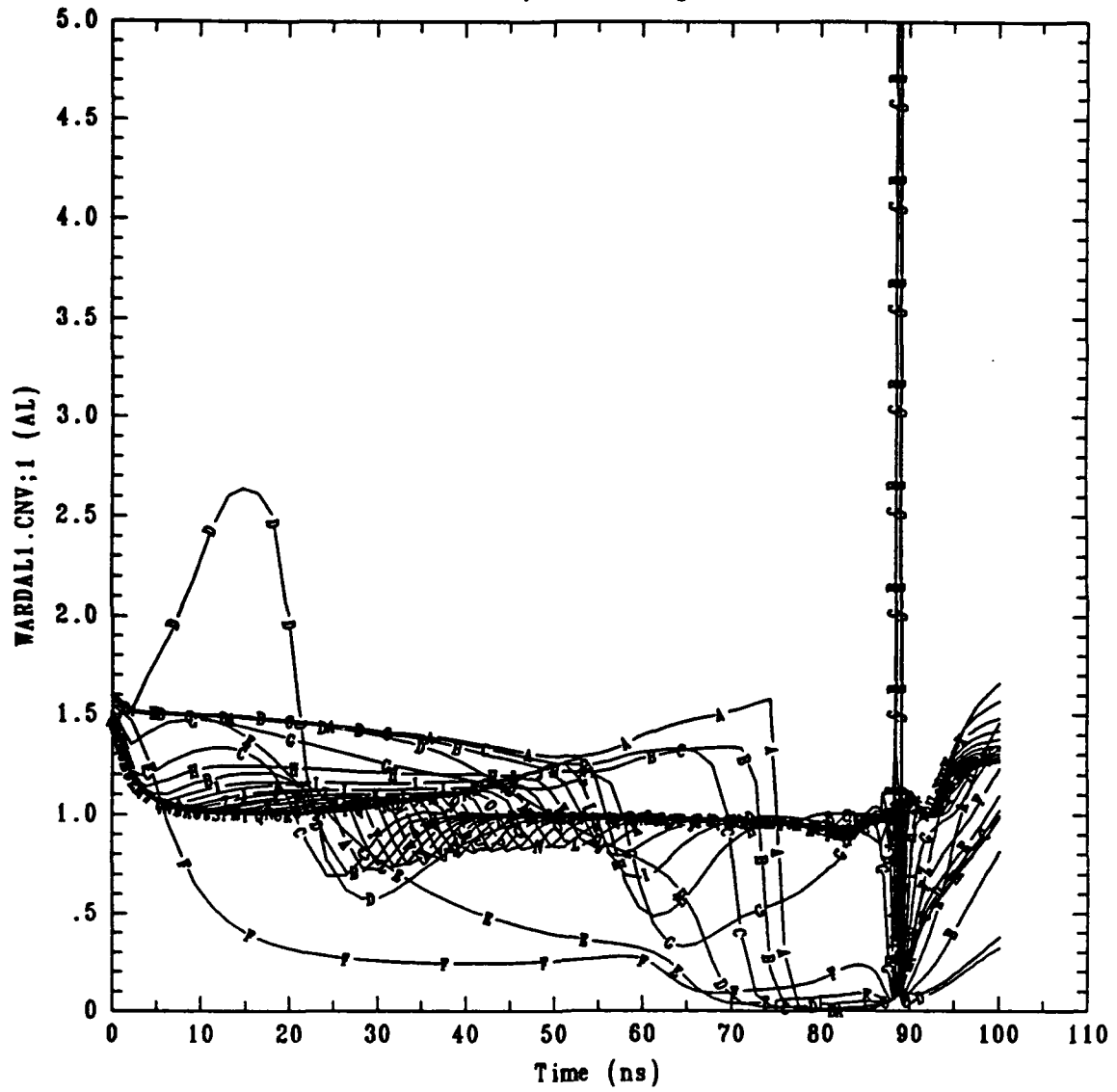
# Ion cyclotron radius



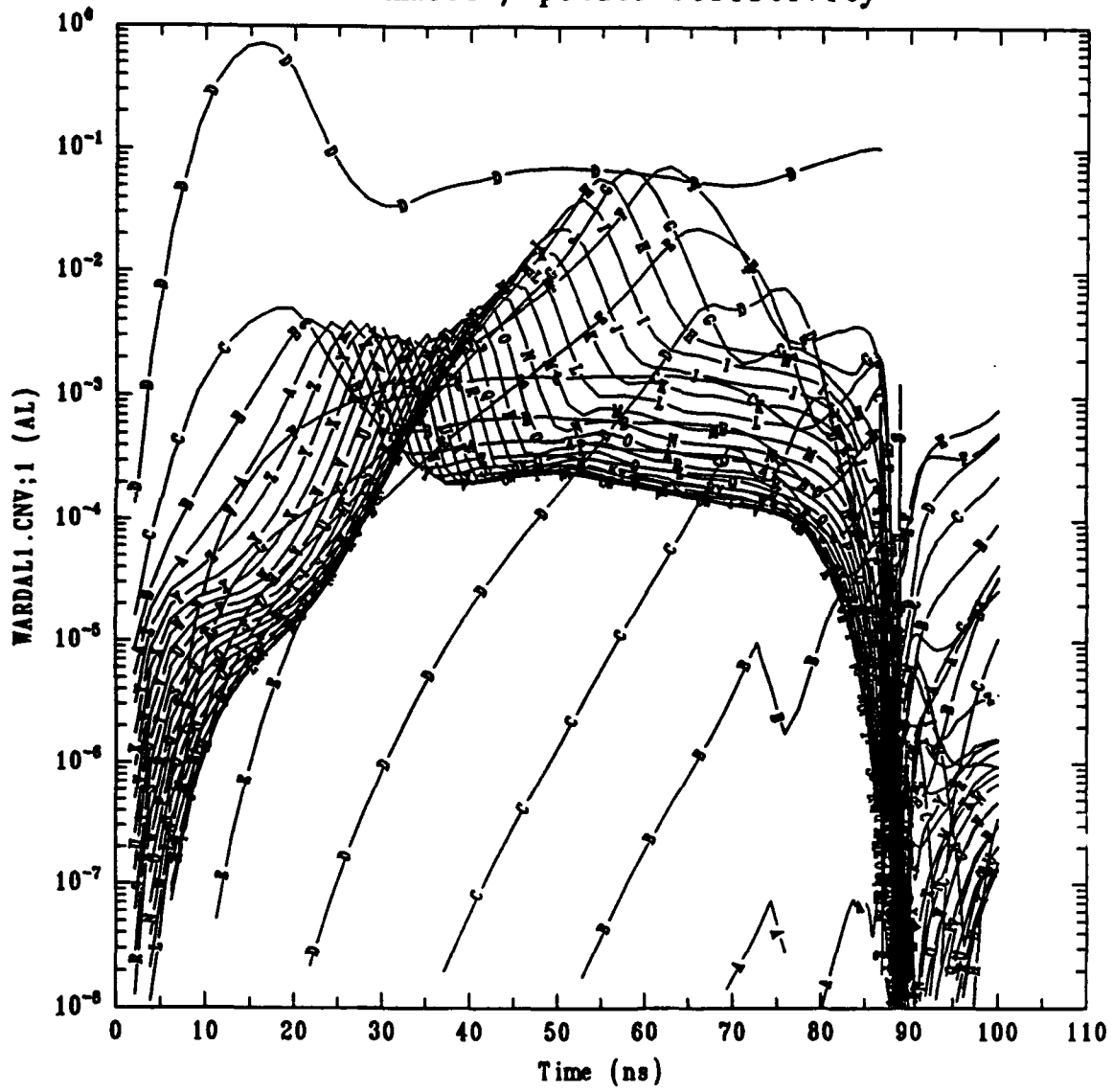
# Electron scale length



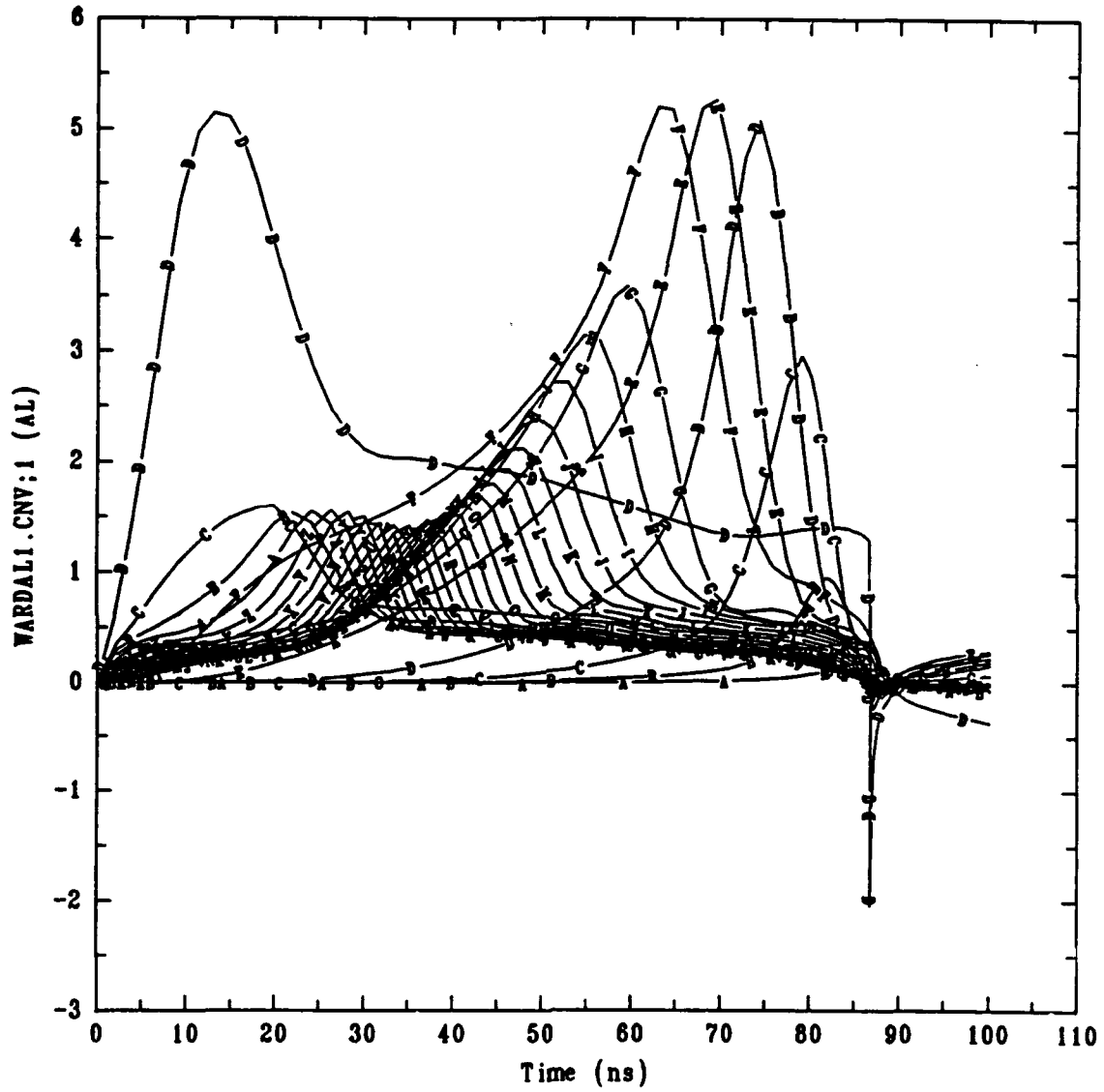
# Electron/Ion temperature



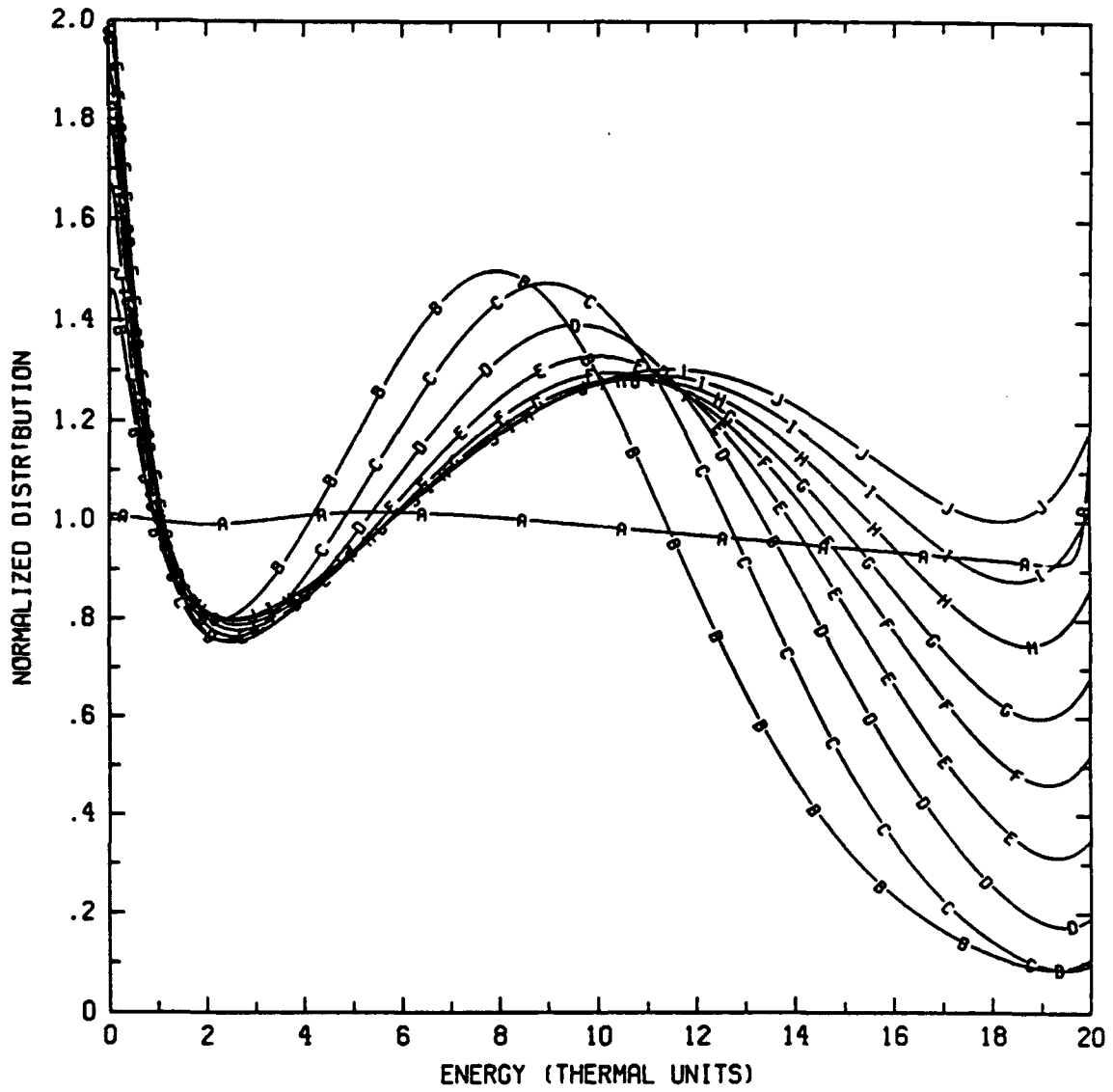
### Anomalous/Spitzer resistivity



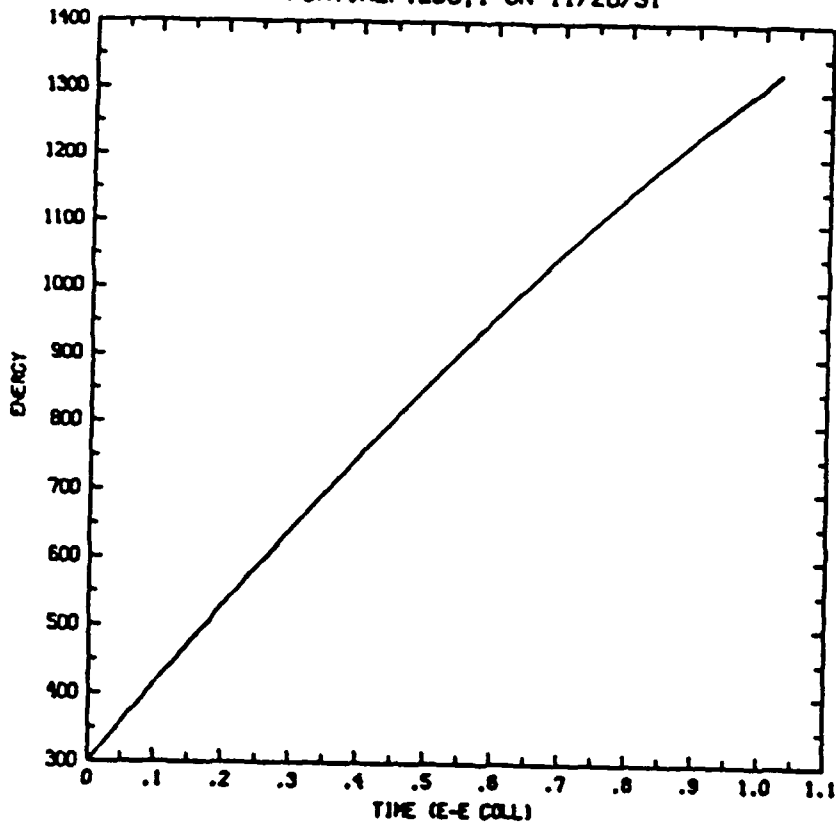
# Drift/ion acoustic velocity



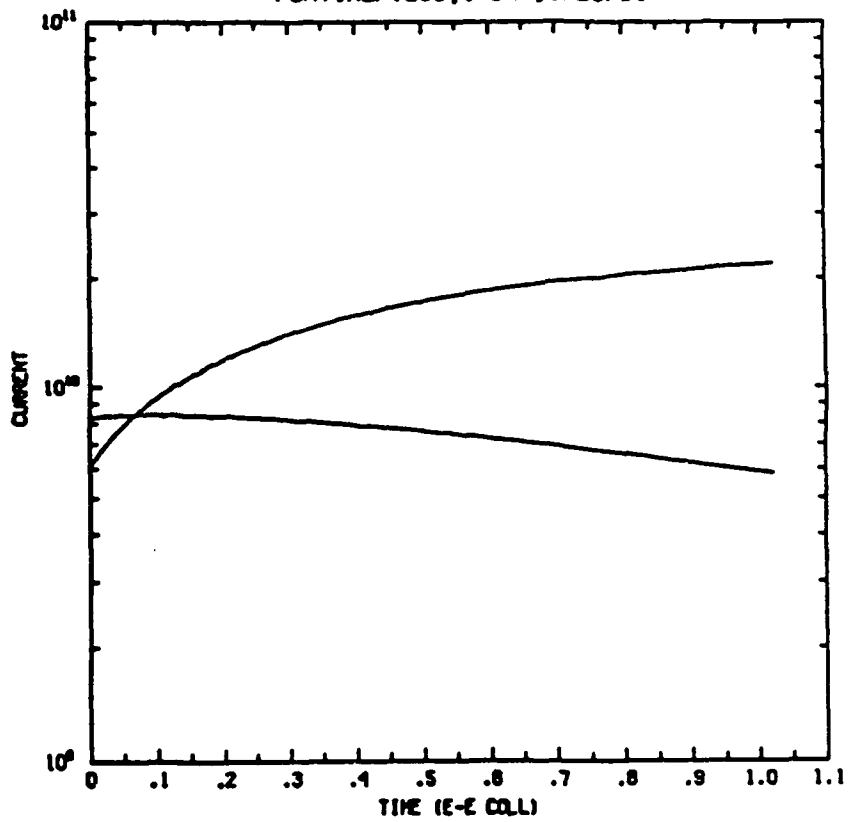
ELECTRON DISTRIBUTION, M=4.9 (M<sub>0</sub>)



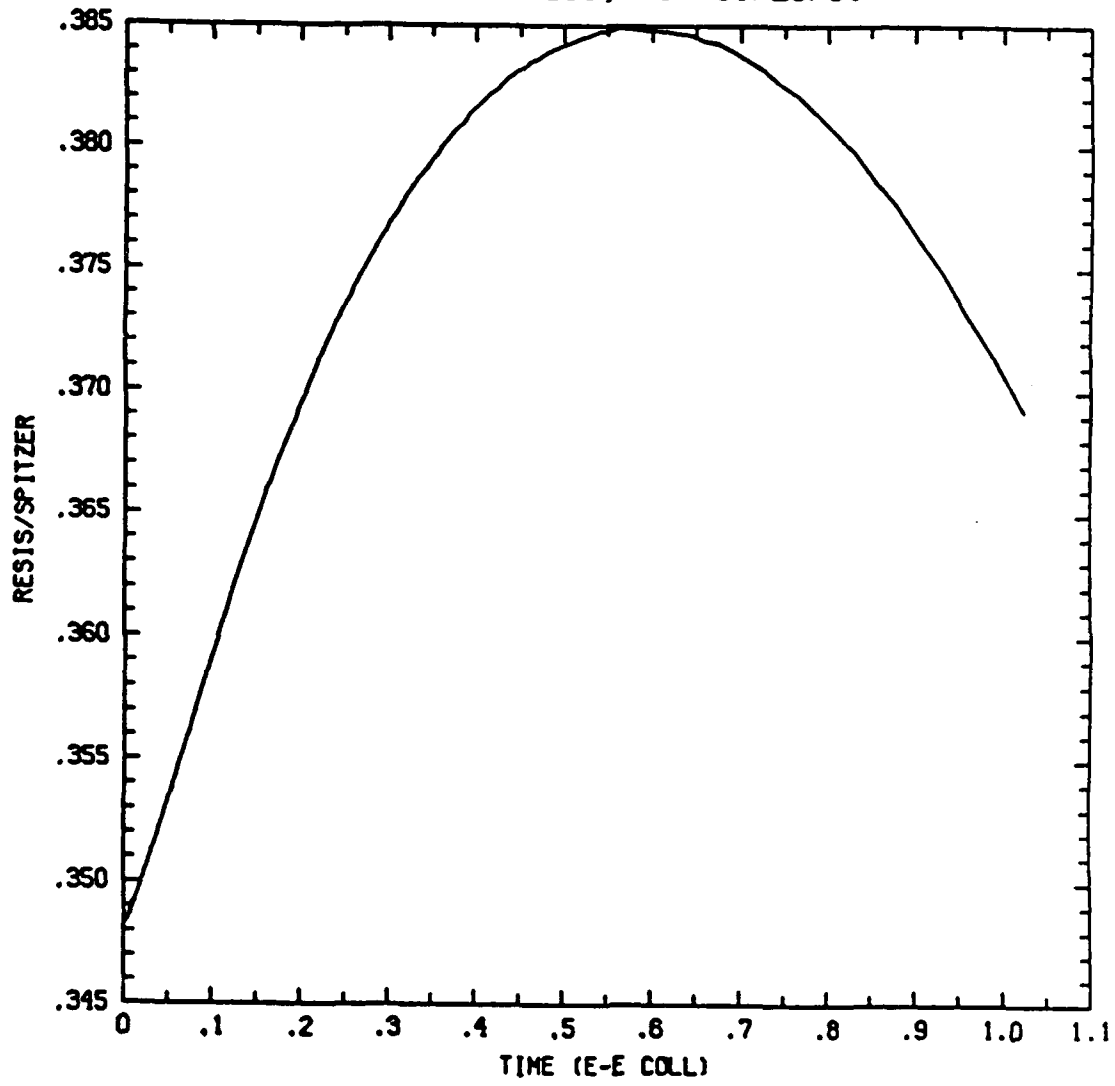
FOKTIMEP.LOG;1 ON 11/20/91



FOKTIMEP.LOG:1 ON 11/20/91



FOKTIMEP.LOG;1 ON 11/20/91



### III. MODELING AND DIAGNOSING L-SHELL DYNAMICS IN PRS EXPERIMENTS

#### A. INTRODUCTION

Until recently, the Plasma Radiation Source (PRS) program at the Naval Research Laboratory (NRL) has tended to emphasize the analysis of K-shell dynamics and K-shell emission behavior [1]. Similar efforts are now needed for the L-shell. There are a number of reasons for this change in program emphasis. As the DNA PRS program moves more and more in the direction of DECADE-class machines, the problem of generating higher yields at higher photon energies through the implosion of higher atomic number elements will become more important and relevant. In these implosions, the L-shell dynamics has a strong influence on the ability of the PRS to reach and to radiate from the K-shell. To theoretically determine this influence, it is important that accurate calculations be made of the power output from the L-shell of optically thick plasmas. From these calculations, we may accurately determine the PRS load requirements for burning through the L-shell into the K-shell, for example. Furthermore, the ability to diagnose the amount of mass radiating in a given ionization stage is an important tool in evaluating the quality of PRS implosions, and in comparing and evaluating the performance of different PRS machines. To date, this capability has been developed and applied to the K-shell H-like and He-like ionization stages [2,3,4]. We are currently expanding this diagnostics work into the L-shell in order to provide a similar study of the dynamics of selenium and other moderate atomic number implosions. Combining K-shell and L-shell diagnostic work with further study of the plasma dynamics will provide a unique opportunity to better understand PRS implosions and the differences in performance of the different decade-class machines. This capability will be essential in order to design these machines for optimal PRS performance and optimal return on investment in pulse power technology.

The determination and the diagnosis of L-shell dynamics requires accurate calculations of L-shell x-ray power outputs. The diagnostic effort also requires that accurate calculations of the L-shell emission spectrum be made

from which line ratios between different ionization stages are computed. Both of these calculations depend critically on our ability to model the multiplet dynamics of the excited states within each of the L-shell ionization stages. Important progress is being made on this problem, and it will be discussed briefly in this section. The section is organized as follows. In the past year we have expanded our diagnostic capabilities in the K-shell and applied them to the analysis of Physics International (PI) experiments. This work will be described first. Then, a review of some of the motivation for and the problems involved in analyzing L-shell dynamics will be discussed. In particular the influence of multiplet structure on power output and L-shell diagnostics will be discussed and illustrated with the development, now in progress, of a selenium atomic model. How this model is to be scaled to other elements will then be mentioned briefly. Finally we present some conclusions and mention some future questions that will need to be addressed.

#### B. ANALYSIS OF K-SHELL DATA

In this past year, we have expanded our diagnostic capabilities in the K-shell, from aluminum and titanium plasmas, to include argon and neon. Two extensive databases describing plasma conditions (such as: power output, electron temperature and ion density as a function of plasma radius) have been compiled from numerous collisional radiative equilibrium (CRE) runs for these two elements. Using these databases, PI Double Eagle argon data and PI Falcon neon data have been analyzed. New experimental data can quickly be analyzed as it becomes available.

The analysis procedure uses typically observed experimental x-ray data to infer the temporally and spatially averaged electron temperature and ion density that are achieved during K-shell emission, and, as a consequence, the mass fraction emitting in the K-shell. As a first step, the total yield in the K-shell x-rays, the K-series spectrum, the x-ray pulsewidth and the time-integrated pinhole picture showing the size of the K-shell emission region are used to determine an average energy production rate per unit length, the radial extent of the emission region and relative line strengths all in the K-shell. (Similar data and similar analysis procedures are under development

for the L-shell.) By combining these experimental quantities with CRE calculations for a uniformly dense, isothermal and optically thick plasma of the observed plasma size, the average temperature and density achieved can be estimated self-consistently.

Figures 1 and 2 show typical power output and line ratio contours obtained from such CRE calculations, in this case for a 2 mm diameter argon plasma. These contours were used to analyze argon experiments, such as PI shot 2268. Figure 3 shows the time-integrated K-shell spectrum for this shot. The K-shell diameter for this particular gas puff experiment was measured to be about 2.4 mm, close to the diameter of the theoretical plasma. Extrapolation procedures are often used to match variable experimental conditions with the theoretical database. Other experimental parameters for this shot are: an initial mass of 37.53  $\mu\text{g}/\text{cm}$ , an initial gas puff length of 2 cm, a pulsewidth (FWHM) of 9 ns, and a K-shell yield of 10.4 kJ. Table 1 shows the results when the contours in Figures 1 and 2 are used to analyze PI shot 2268. The results are similar to other results obtained from K-shell analysis: the K-shell emitting mass is less than the initial emitting mass. Is the missing mass to be found in the L-shell emission region and how does it vary from experiment to experiment? These are some of the important questions to be answered by an L-shell analysis especially as experiments are scaled to higher atomic number elements.

We are in the process of extending the above diagnostic techniques that were developed for use in the K-shell to the L-shell. Such a technique will allow us to analyze existing L-shell data, which in turn will test and anchor our understanding of plasma implosion and thermalization dynamics.

### C. MOTIVATION FOR STUDYING L-SHELL

To expand our understanding of this plasma dynamics, we need to analyze the L-shell emission region and to determine how it influences the K-shell emission. The L-shell emission region (see Figure 4) is generally large compared to the K-shell region. Thus, an analysis of L-shell x-ray data will provide insights into the plasma PRS dynamics outside of the K-shell region.

Figure 5 illustrates how the power output varies with average plasma ionization for a uniform selenium plasma a few millimeters thick. The curves are based on a CRE calculation. One sees that the higher the atomic charge  $Z$ , the harder it is to ionize to the K-shell. Indeed most experimentally observed emission from higher  $Z$  materials occurs down near Ne-like through O-like ionization stages, where the emitted power is about a factor of 10 less than near the K-shell. These curves unfortunately lack the needed accuracy to make reliable data inferences. (They were calculated using a hydrogenic atom model, neglecting the complex multiplet structure in the L-shell.) Nevertheless, as can be seen from Figure 6, to get to the 10+ keV K-shell photons (using Se), one must first burn through the 1-3 keV L-shell photons. Detailed L-shell atomic databases plus detailed diagnostics will lead to reliable scaling relationships in the L-shell region, an improved understanding of L-shell plasma dynamics, and, as a consequence, improved PRS load designs.

During the past year, work has begun on evaluating our modeling capabilities in the L-shell by building a selenium model with improved atomic multiplet structure in the Ne-like and F-like ionization stages. Looking at this multiplet structure will inevitably lead to a more complete and reliable picture of the plasma L-shell dynamics within a z-pinch. If, in addition, we successfully scale the L-shell collision strengths in energy and in atomic number, then we will be able to quickly and easily analyze other elements with moderate atomic number, such as molybdenum which has been proposed in experiments by Maxwell Laboratory, Inc..

#### D. MULTIPLY STRUCTURE

As mentioned, the important consideration in calculating x-ray emission from L-shell ions is the potentially large number of multiplet states whose populations must be coupled together and determined in the ionization calculation. The effective increase in radiation losses when multiplet structure is included for the  $\Delta n=0$  lines in the M-shell of Se (see Figure 7) has already been investigated and can be seen in Figure 8 [5]. We expect similar increases in the L-shell power output when the  $\Delta n=1$  L-shell multiplet structure is included. This would increase the L-shell power output in Figure

5, since these curves were calculated without taking into account this structure. This problem is especially important in optically thick plasmas.

Also due to the detailed energy level structure, L-shell spectra (see Figure 9) tend to be fairly complex compared with K-shell spectra. Since CRE calculations of the ionization state of a plasma are sensitive to the multiplet structure, its effect on the diagnostics procedures also needs to be investigated. As a first step, we have set up two different ionization calculations to study the dynamics of the  $n=3$  s and p states in neon-like selenium. In one, the 3s and 3p states are coupled to one lumped 3d state; in the other, they are coupled separately to each of the twelve 3d multiplet states (see Figure 10). The sensitivity of various line ratios and line powers of diagnostic interest to the different ionization coupling assumptions is being calculated. These differences are of interest since most radiative MHD calculations make use of hydrogenic or average atom models in which all states are lumped together by (n) or (nl) configurations.

#### E. L-SHELL SCALING

Over the past years, a fairly extensive atomic data base covering the K-shell region has been built up and used to obtain both detailed diagnostic [1] and K-shell emission scaling relationships [6,7]. As interest turns to higher Z materials, detailed L-shell atomic data bases are necessary. The only way to obtain atomic databases efficiently and reliably is by scaling the relevant rates with energy and atomic number, Z. Whereas, in the K-shell the two most dominate processes that determine the degree of ionization balance are collisional ionization and radiative recombination, in the L-shell the two most dominate process are collisional ionization and dielectronic recombination [8]. The dielectronic rates have been calculated using detailed atomic structure and have been scaled [9]. A method for obtaining and scaling the ionization/excitation collision strengths is under development [10]. The method has been shown to work but requires an investment in data generation and data management. However, once the rates have been calculated we have established that we can determine accurate scaling relationships for the ionization and the x-ray emission, similar to the work done in the K-shell [6,7].

## F. CONCLUSIONS

By using the existing Al, Ti, Ne and Ar K-shell databases, and, in the future, L-shell databases to analyze data from various machines, we will be able to gain new insights into the PRS plasma dynamics and to better evaluate and optimize machine performance. With the ability to analyze L-shell data, we will find out why the K-shell emitting mass appears to be constant with array diameter (see Figure 11) and to see how the L-shell emitting mass behaves. We will also be able to address such questions such as: can the missing K-shell region mass be accounted for in the L-shell emission region and what is experimentally governing its influence on the K-shell dynamics? How does mass participation vary from machine to machine and from element to element? These are just some of the questions that need to be answered in coming years using the experimental data analysis procedures recently perfected at NRL.

To address these questions, however, it is essential that the radiation losses from the L-shell due to multiplet structure be determined. We need to scale the ionization and x-ray emission in the L-shell with atomic number to achieve the versatility needed to analyze and theoretically model a variety of experiments. And, x-ray diagnostics in the L-shell are needed comparable to what we already have in the K-shell.

## FIGURES AND TABLES

Figure 1. Contours of power output as a function of ion density and electron temperature for an 2 mm diameter argon plasma.

Figure 2. Contours of line ratio as a function of ion density and electron temperature for an 2 mm diameter argon plasma.

Figure 3. Time-integrated experimental spectrum from PI shot 2268.

Figure 4. Typical pinhole pictures showing time-resolved L-shell and K-shell emission region (courtesy of C. Deeney).

Figure 5. Power output versus average ionization of a Se plasma for three different ion densities. (Courtesy of J. W. Thornhill).

Figure 6. Theoretical Se spectrum showing K- and L-shell lines, and continuum.

Figure 7. The LS multiplet structure of the  $\Delta n=0$  states in Al-like Se.

Figure 8. Ratio of the power outputs of  $\Delta n=0$  lines transported nonhydrogenically to  $\Delta n=0$  lines transported hydrogenically for Al-like Se ( from ref. 1).

Figure 9. Nickel spectrum showing L-shell spectrum.

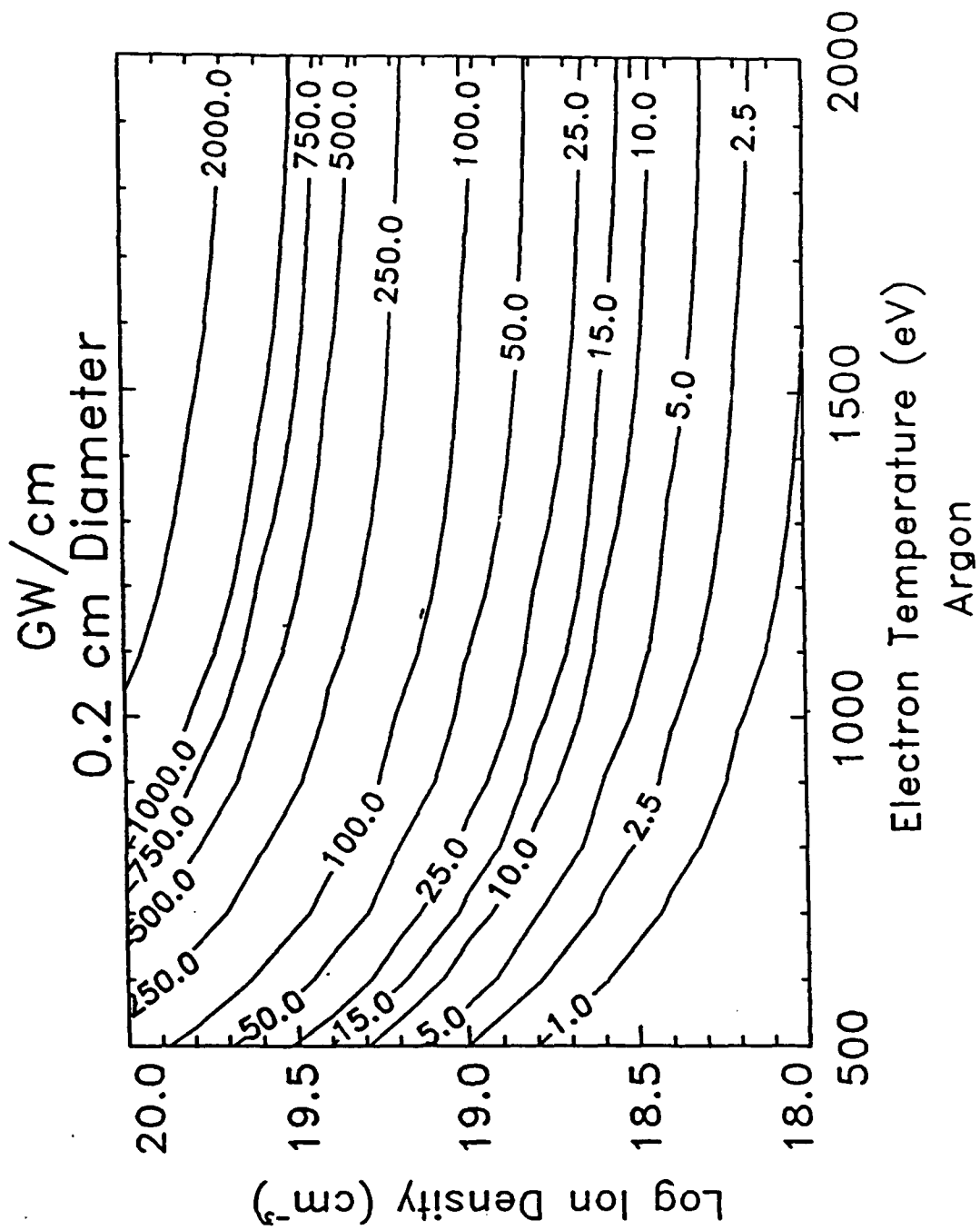
Figure 10. Energy level diagram showing multiplet structure for Ne-like Se.

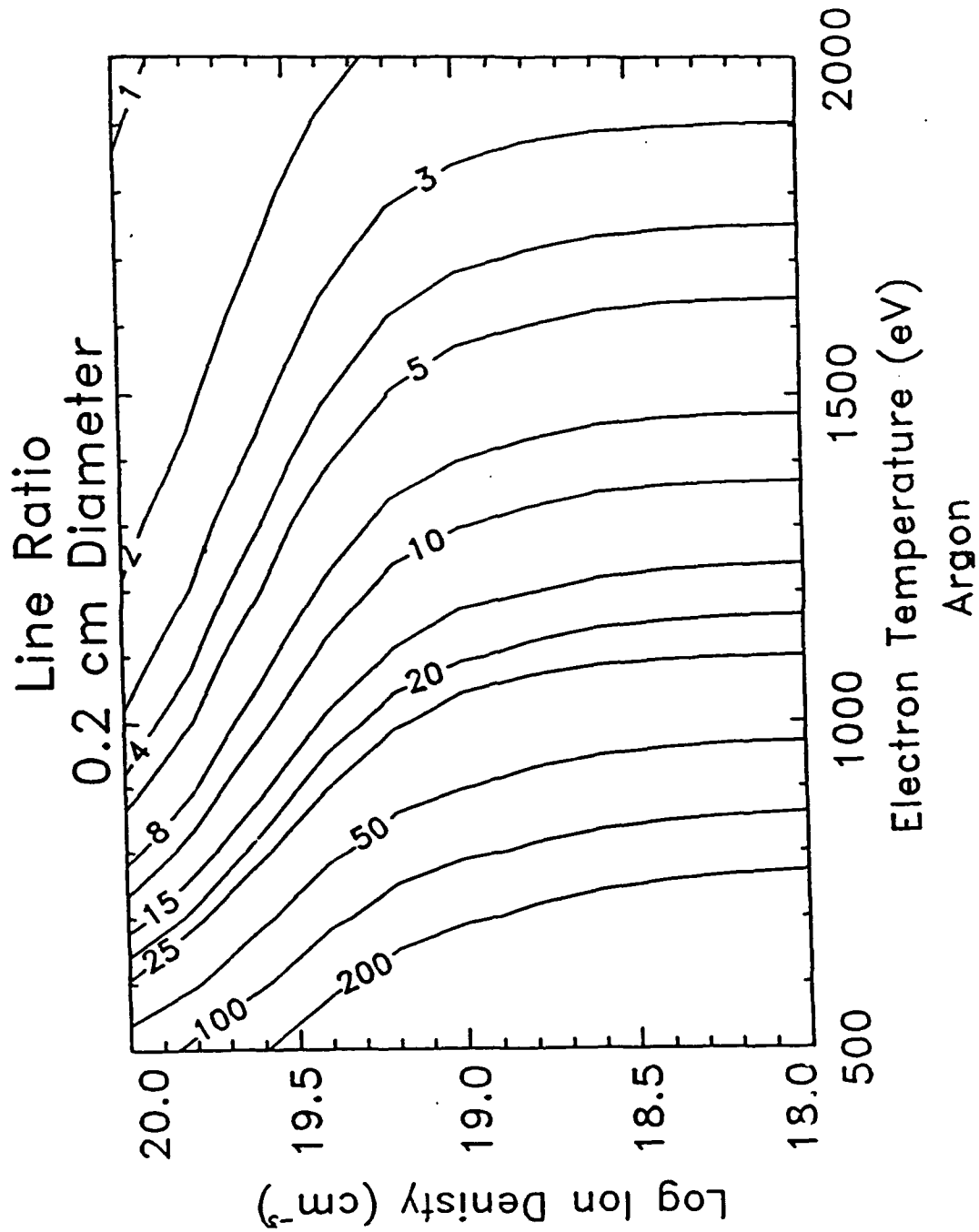
Figure 11. Initial wire mass and K-shell emitting mass versus array radius for PI Al wire experiments.

Table 1. Results of argon gas puff experiment (shot 2268) at Physics International.

## REFERENCES

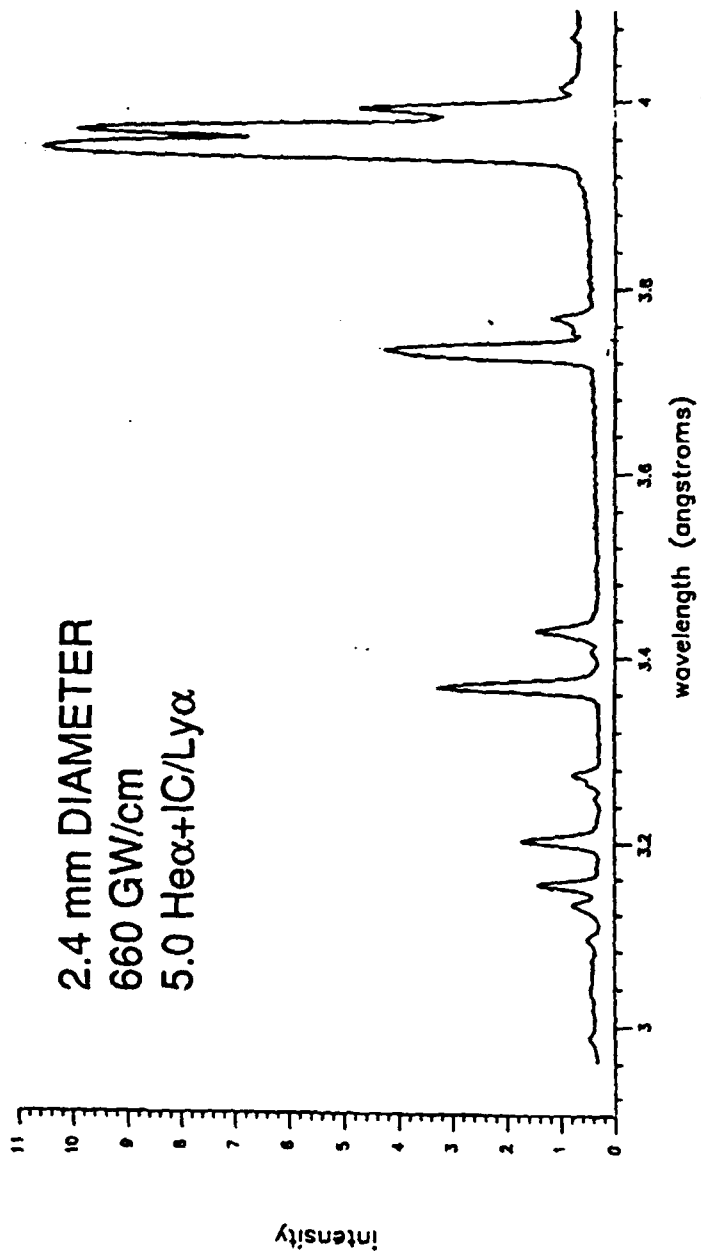
1. M. C. Coulter, K. G. Whitney, and J. W. Thornhill, *J. Quant. Spectros. Radiat. Trans.* 44, 443 (1990).
2. N. Loter, M. Gersten, R. Grandey, J. Rauch, K. Ware, M. C. Coulter, J. W. Thornhill, and K. G. Whitney, *J. Quant. Spectros. Radiat. Trans.* 44, 509 (1990).
3. M. C. Coulter, K. G. Whitney, and N. G. Loter, *Analysis of Maxwell Laboratory Wire Experiments*, NRL Memo Report 6383 (1988).
4. Deeney, C., T. Nash, R. R. Prasad, L. Warren, K. G. Whitney, J. W. Thornhill, M. C. Coulter, *Phys. Rev. A* 44 (1991).
5. K. G. Whitney and M. C. Coulter, *IEEE Trans. on Plasma Science* 16, 552 (1988).
6. Whitney, K. G., J. W. Thornhill, J. P. Apruzese, and J. Davis, *J. Appl. Phys.* 67, 1725 (1990).
7. Thornhill, J. W., K. G. Whitney and J. Davis, *J. Quant. Spectrosc. Radiat. Transfer* 44, 251 (1990).
8. Dasgupta, A., K. G. Whitney and M. Buie, *Bull. of the Am. Phys. Society* 35, 2077 (1990).
9. Dasgupta, A., K. G. Whitney, *Phys. Rev. A* 42, 2640 (1990).
10. DNA Final Report, Radiation Hydrodynamics Branch, NRL (1990).



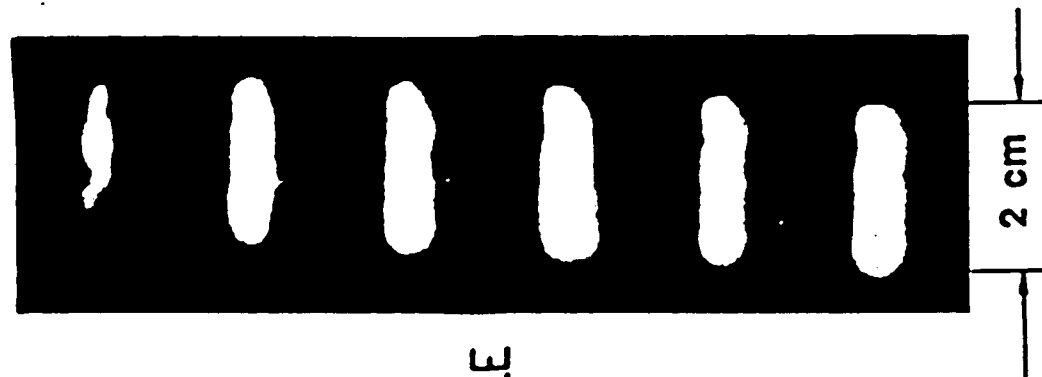


TIME-INTEGRATED SPECTRUM  
ARGON SHOT 2268

2.4 mm DIAMETER  
660 GW/cm  
5.0 He $\alpha$ +1G/Ly $\alpha$



# ALUMINUM PINHOLE PICTURES

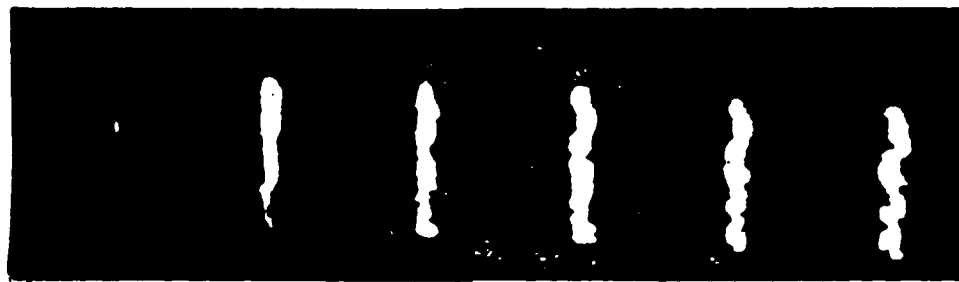


CURRENTLY

NON-ANALYZABLE

2 cm

L-shell



5 ns

10 ns

15 ns

20 ns

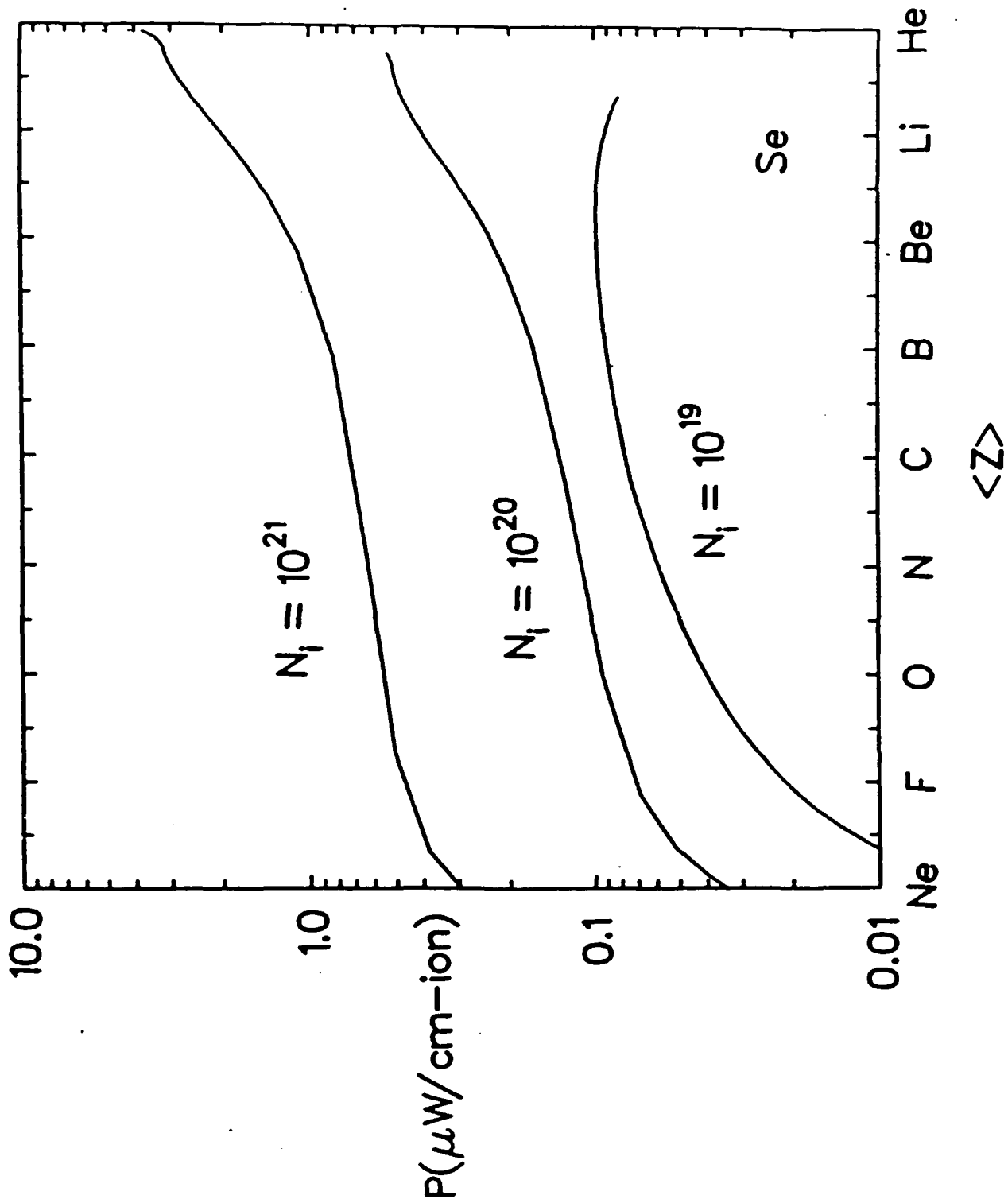
25 ns

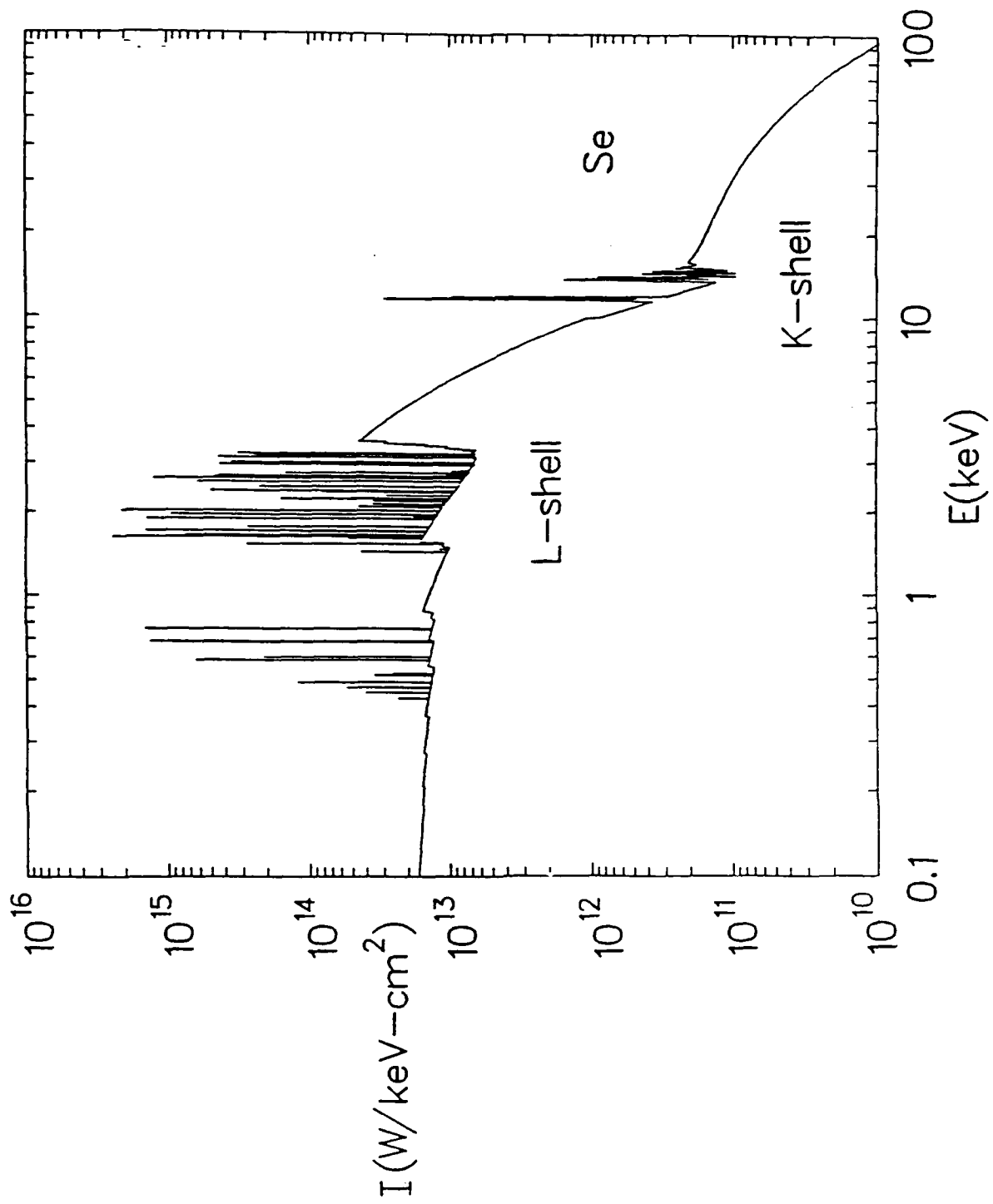
30 ns

CURRENTLY

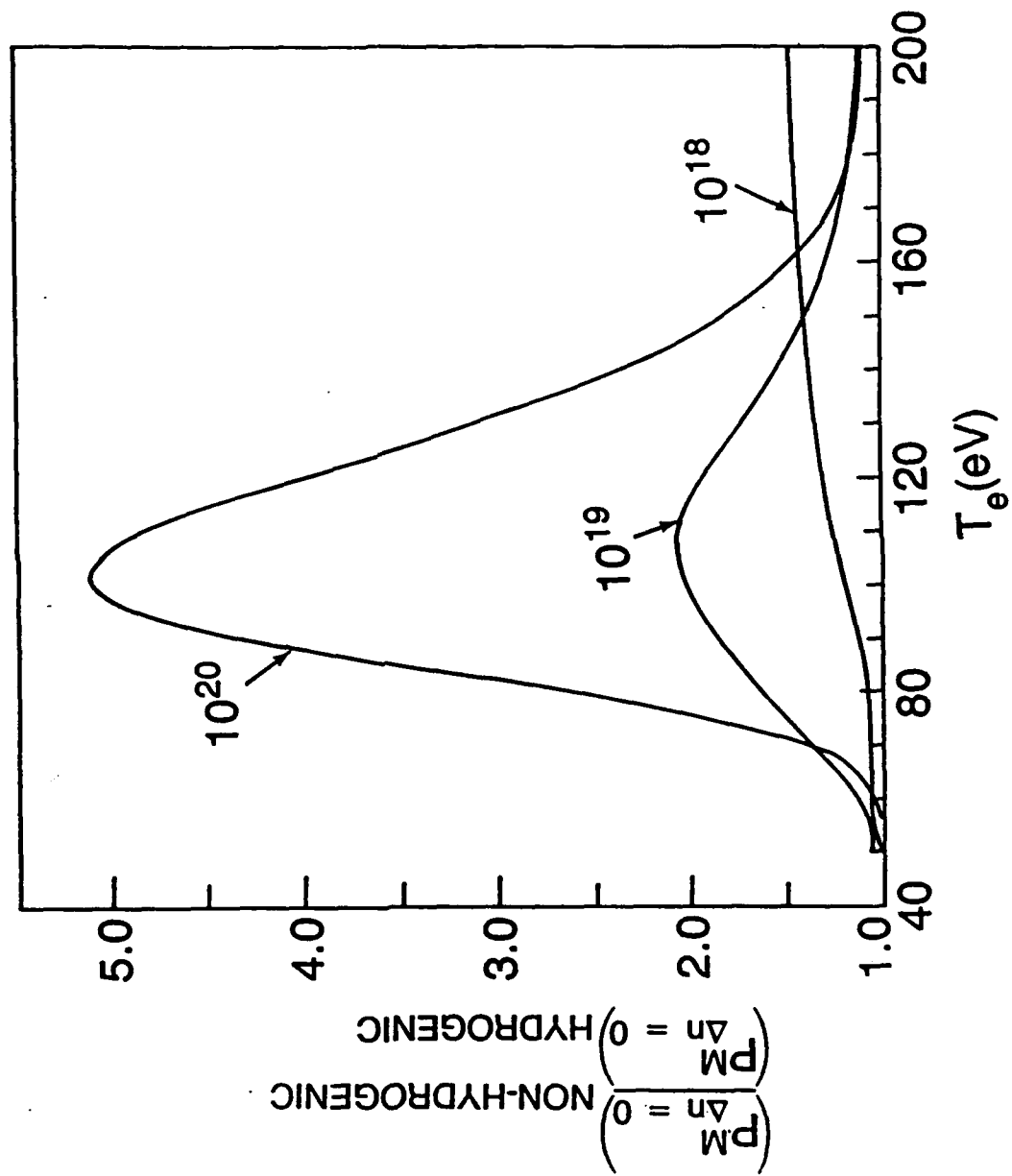
ANALYZABLE

K-shell

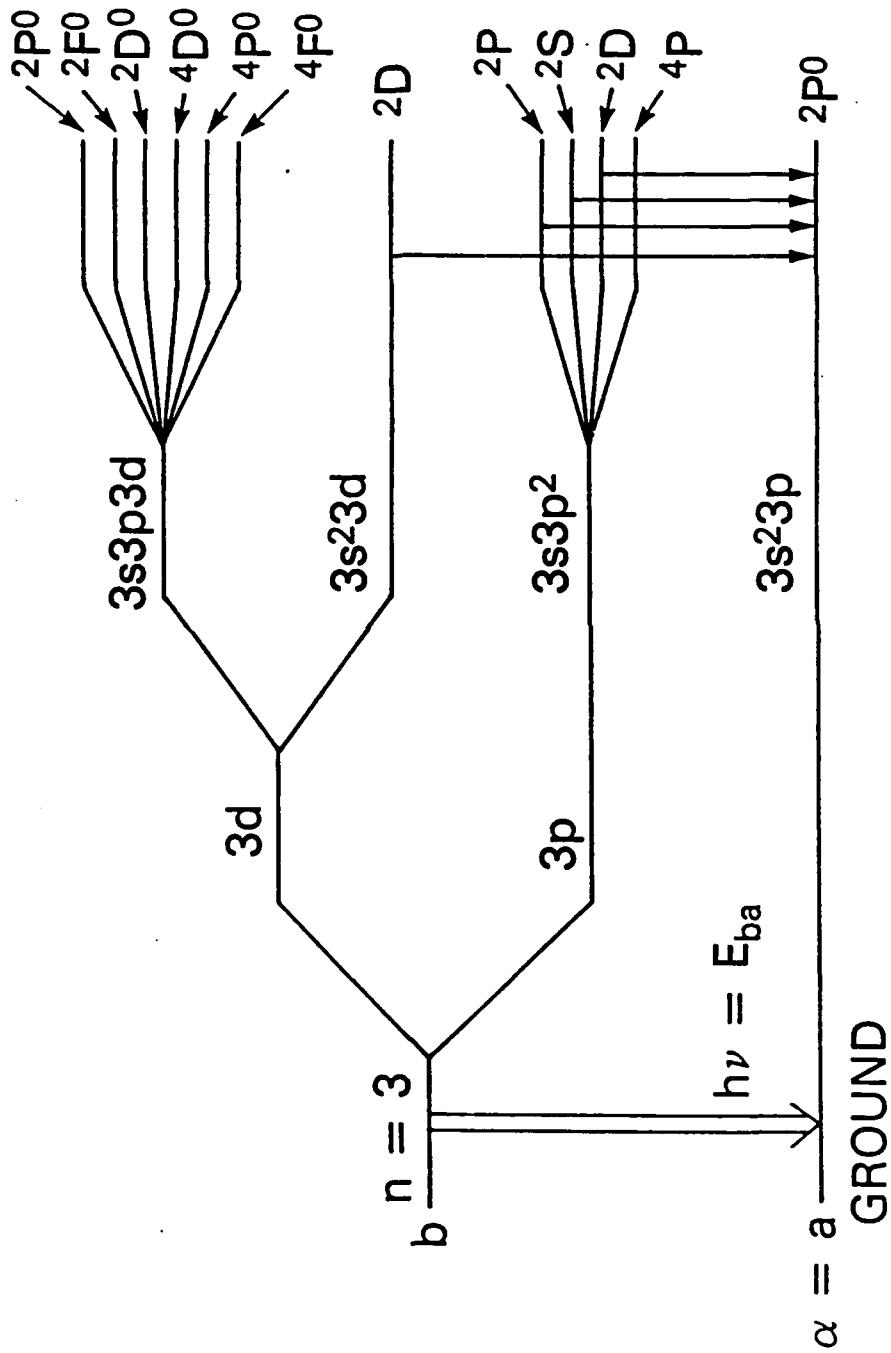




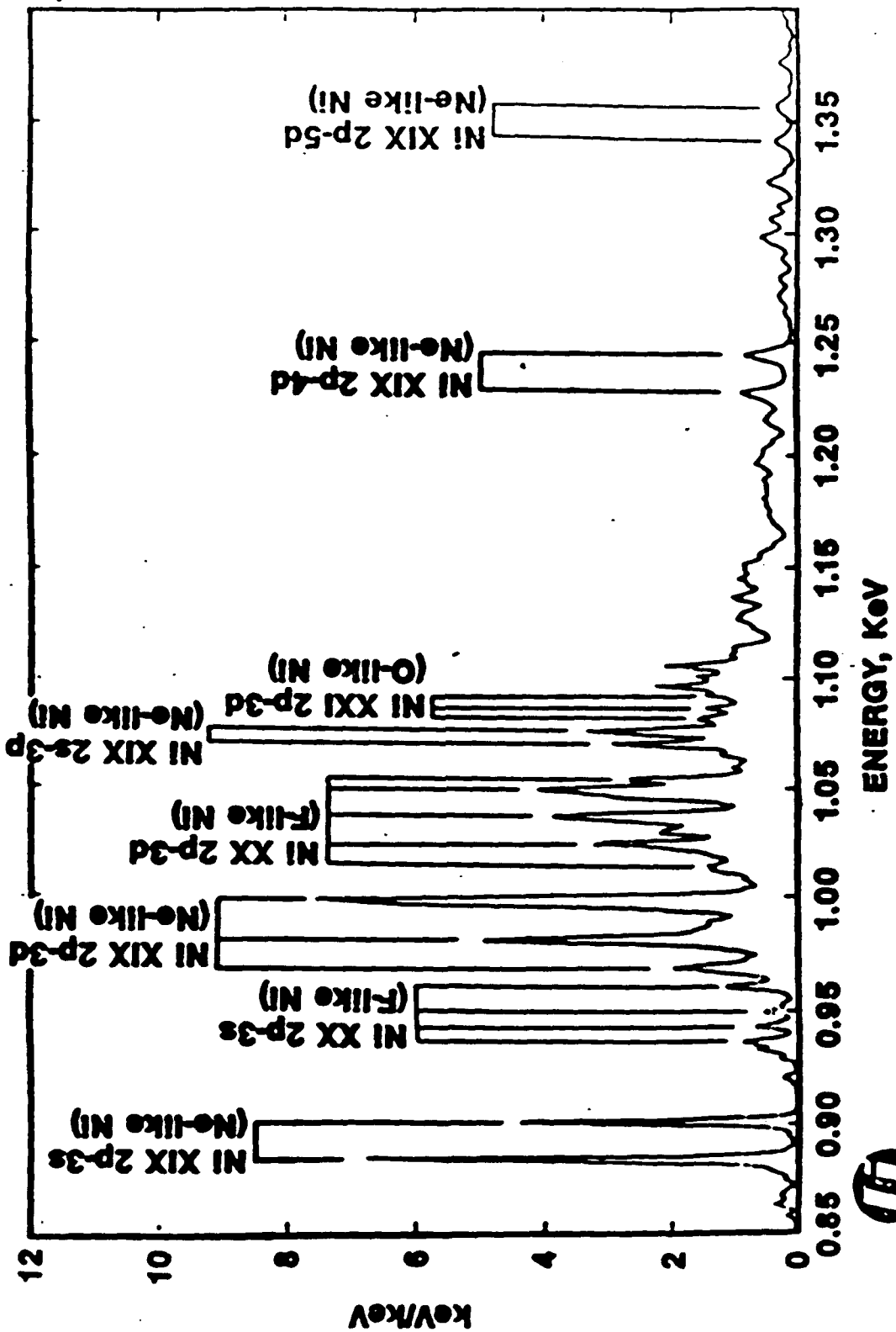
RATIO OF POWER OUTPUTS OF  $\Delta n=0$  TRANSPORTED  
 NONHYDROGENICALLY TO  $\Delta n=0$  LINES  
 TRANSPORTED HYDROGENICALLY.

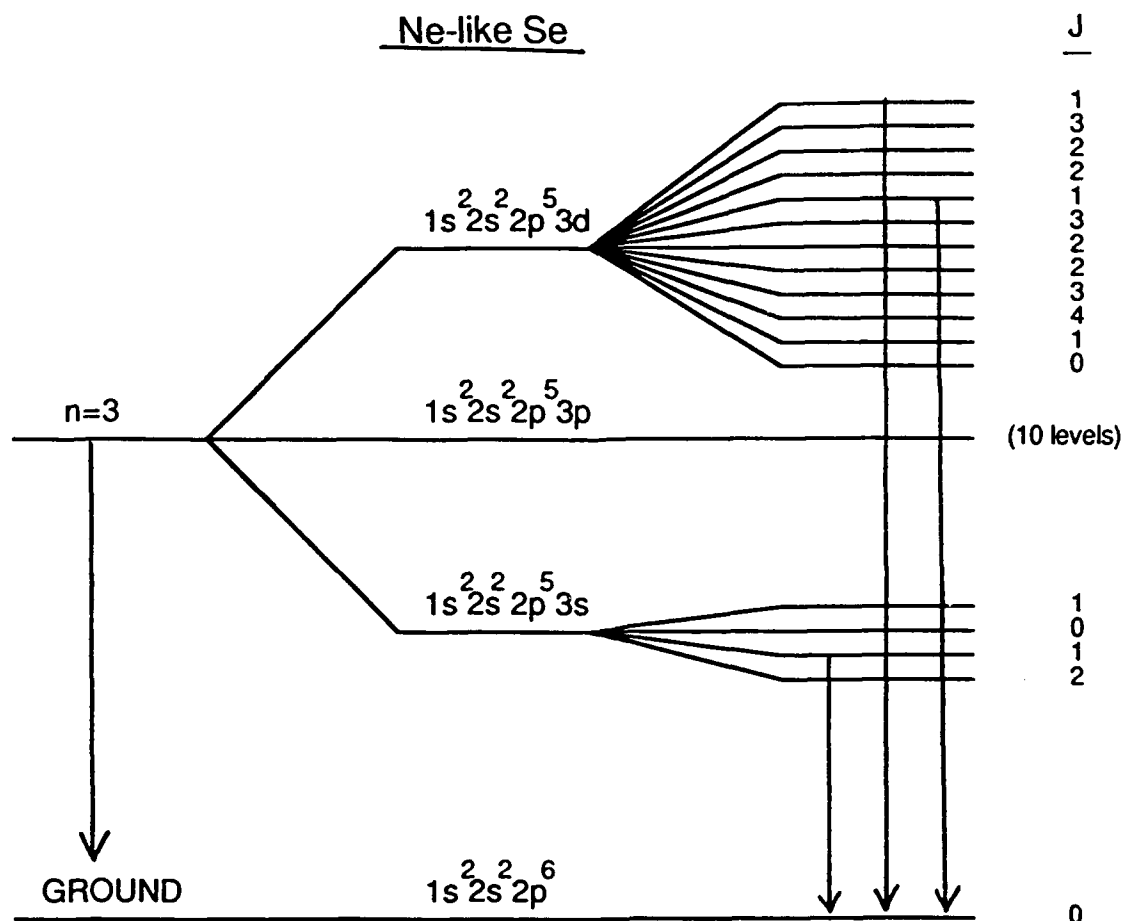


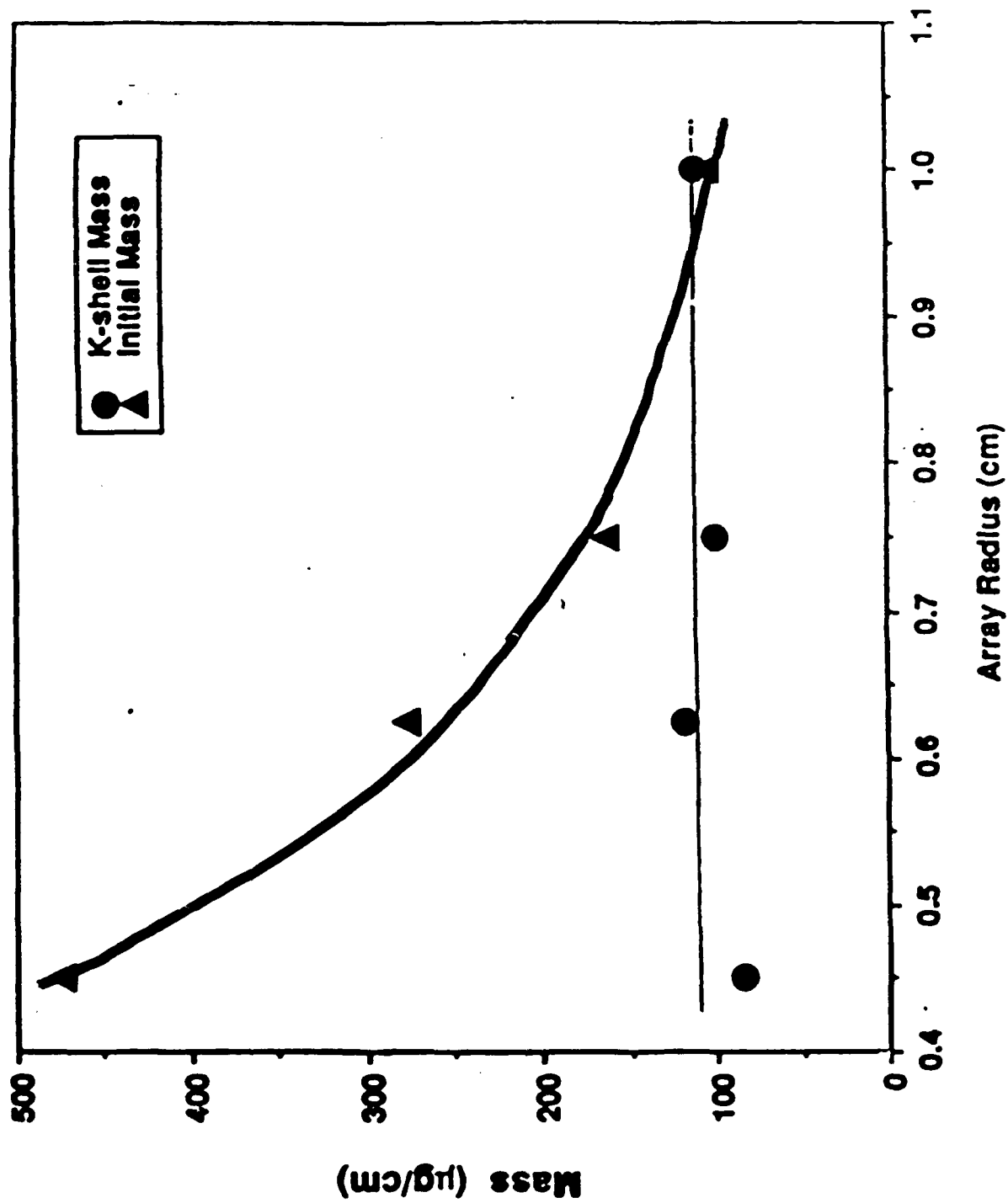
THE LS MULTIPLY STRUCTURE OF THE  $\Delta n=0$  STATES  
IN AL-LIKE SE.



# Nickel Spectrum Line Identifications







## SHOT 2268\*

### DATA AND ANALYSIS OF THE K-SHELL REGION

TIME STEP	DIAM mm	PWR GW/cm	He $\alpha$ +IC /Ly $\alpha$	Te eV	Ni/10 <sup>18</sup> cm <sup>-3</sup>	f <sub>M</sub> <sup>+</sup>
1	-	-	45.0	(1000)		
2	2.4	400	3.0	1900	1.5	0.12
3	2.4	400	4.0	1750	1.5	0.12
4	-	50	12.5	(1400)		
TI	2.4	660	5.0	1650	1.6	0.13

\* Argon data from C. Deeney, Physics International  
 + Fraction of initial  $\mu\text{g/cm}$  emitting in the K-shell.

TABLE 1

## **IV. Power Flow in Decade Class Machines: Developing Transmission Line Models for the Long Conduction Time POS Coupled to a PRS**

### **A. Introduction**

Interactions between a Decade class plasma opening switch and a plasma radiation source load are driven by three constraints. The POS generally opens best when any downstream inductance is small compared to the storage inductance, but it may close again if the plasma radiation source load erects too large a voltage reflection when it makes its transition from low to high impedance. The PRS generally obtains good energy coupling when the energy it needs is delivered promptly to the last 20 nH or so of transmission line, whatever the details of the driver configuration. The trade-offs involved here can be argued at length, but what appears lacking is a theoretical model containing both elements: POS and PRS, and characterizing each by the salient physics of the device rather than by largely arbitrary free parameters.

We have been quite successful heretofore in forging simple PRS descriptions and in investigating the electrical consequences of various load parameters on different drivers, e.g. Saturn, Double-Eagle, and Phoenix. Many of those investigations involved the use of phenomenological modules to mock up the POS – typically as a time dependent resistance with a conduction delay. The proper context for the work presented here is that of a natural extension of these previous studies, but different in that it is

- focused on Decade designs and PRS performance, and
- tied to a POS model which is at once simplified, yet grounded in a few simple hypotheses with no free parameters.

The PRS model, transmission line model, and driver models are very well known and understood. The normal application is to (i) set a voltage source at the input (typically a fast capacitor with some coupling inductance), (ii) define a transmission line to model the storage inductance and front end, (iii) install a time dependent opening switch at one node to imitate a POS, (iv) drive a slug or more sophisticated "gas bag" load model to imitate the PRS. All the usual line diagnostics provide the time histories of currents or voltages at any desire location, and estimates for the PRS yield can be extracted from the simplest load models in a variety of ways. The

existing transmission line models and load models can and have been exercised to examine the tradeoffs of inductance, opening time and reflected voltage – but the essentially free POS conduction time and opening rate parameters really set the final results. The POS represents a singular unknown in all this. However it is modeled phenomenologically, there is so far no coherent and satisfactory description of its properties that will allow a clean and sensitive assessment of PRS performance in Decade.

Since its origin some fifteen years ago the plasma opening switch has proved amenable to a fairly wide variety of moderately successful theories. The first attempts<sup>1,2,3</sup> focused on a four phase, phenomenological description of its operation, now known as the "NRL Model". As a working hypothesis the four phase picture succeeded in identifying parameter regimes in plasma density and injection velocity which satisfied the known experiments at short conduction times ( $\approx 200$  ns) and higher voltages ( $\approx$  MV). One also finds ample evidence that some sort of gap opening mechanism at the cathode could account for the rapidly increasing resistance observed in normal operation of the devices.

On the other hand this four phase picture proved very difficult to anchor in first principles theory<sup>4,5,6,7</sup> and to date many questions remain open. In particular, the scaling of peak conduction current with plasma parameters such as density, switch length, has not been accounted for in any systematic way. The crucial dependence of the sheath scale lengths on density or injection speed has only recently been accounted for in a systematic description which still ignores the problem of emission in a magnetized sheath. As the conduction time is extended, the competition or even transition among opening mechanisms has not been sorted out. The role of surface effects in the emission process for long conduction times is unclear, as are the ultimate limiting factor or factors which must, sooner or later, preclude an opening at sufficiently high density.

The investigation of these questions usually revolves around fairly primitive diagnostics with regard to the plasma dynamics. The current channel width and location is often resolved with magnetic probes and the plasma density assessed with broad microwave beams. Early experiments<sup>8,9</sup> have been systematic but poorly resolved and thus are inconsistent and plagued by controversy. Later experiments in similar pulse power environments<sup>10,11</sup> have the potential for useful resolution but have yet to

be extended to plasma opening switches. In many cases these experimental efforts provide at least the generic configurations and define a framework of observables which theory must discuss. In other cases experiments offer important clues to the operation of the switch. In the long conduction time limit ( $\approx 1\mu\text{s}$ ) recent efforts at NRL<sup>12</sup> have shown, in the center of the radial gap, the existence of a very strong density depletion region or "channel", since it is really a line integrated measurement. The conduction phase current either crosses this density depletion "channel" or finds the channel magnetically insulated to varying degrees along its length. The observation of such a channel represents a fundamental change in the known morphology of the switch plasma and will therefore play an important role in what is developed here.

Since the conduction phase is the subject of most of the controversy, the competing descriptions and extensions to the four phase model which have been developed so far tend to treat this phase primarily, and fall into two major classes: diffusive and advective. This distinction is of course not very strict nor of particular importance except as a guide to the primary theoretical ideas. The diffusive models tend to concentrate on the width of the current channel in the POS and examine the effect of various microinstabilities on the current conduction process. The advective models tend to focus on the location of the current channel and account for the duration of the conduction phase. Whatever the emphasis in terms of detailed physics, the primary question for any conduction phase model is whether the POS is a peak current limited device or a time limited device. If the conduction current has a fixed upper limit for any history of charging the upstream inductance, then presumably designing for this peak conduction current depends on knowledge of an identifiable set of plasma variables such as density, injection velocity, physical extent or temperature. If the conduction current depends on the penetration time for a current channel, then the charging rate will determine the peak conduction current as a simple contest of time scales and plasma length.

The diffusive models<sup>13,14</sup> have achieved a reasonable description of the conduction phase and even opening rates as measured against the POP experiments at NRL. The most interesting aspect of such a comparison is that the diffusive picture includes no emission constraints whatever in determining the opening - the current layer simply moves through the POS and then flows to the shorted load. In the case of a higher load impedance this opening process would look a good deal more sluggish

and the local details of magnetic insulation in the downstream transmission line would presumably play a more important role in establishing a true opening event. The weakest link in the theory is unfortunately its very strength – all the relevant saturation amplitudes of the microinstabilities must be calculated.

While reasonable estimates can be made there is more unknown territory to cover if a truly predictive capability, good enough to support machine design, is to be achieved. Early diffusion models found that the modified two stream instability (MTS) was a likely candidate for the apparent high resistivity of the POS, but the saturation levels could only be estimated and the theory of the more general and relevant kinetic cross field streaming instability was not developed to the point that a definitive calculation could be made of the nonlinear saturation. More recent work<sup>15,16</sup> has pointed out electrostatic instabilities similar to the ion acoustic (IA) mode which are perhaps even more relevant and very rapidly growing. Here again the calculation of a credible saturation level is complicated by mode coupling and mode conversion channels, subject to some controversy<sup>17</sup>, and awaits a more complete treatment.

The advective models<sup>18,19,20,21,22</sup> take their impetus from the Hall current channel, which has been a clear feature of all early particle simulation work, and arises from the tendency of the switch current to magnetize (and magnetically insulate) the electron population faster and more completely than the ion population. In principle the Hall channel could carry an unlimited amount of current, the issue of peak conduction current is therefore carried into a study of the dynamics of the charge separation in response to the incoming driver pulse. On the other hand, in particle simulations at least, the Hall channel tends to be narrow, apparently at variance with experiment, and clearly unstable with respect to the new electrostatic modes (of Ref. 15,16) because of the high current drift velocity which is usually seen in such calculations. The existing treatments of the Hall channel do not explore this issue, usually relying on a generalized Ohm's law to define the axial (downstream) electric field component.

In summary one can thus resolve two major problem areas to be treated by a POS theory which will be simple and useful in the context of the typical Decade/PRS power flow calculation. In the conduction phase a contest between diffusion and advection is to be unraveled and may have different results in high density or low density plasma domains. In the opening phase the sheath gap dynamics is crucial, but the

gap opening mechanisms cannot be separated from the magnetic insulation problem in the sheath. The model developed here is intended as a picture which is simplified to one dimension as much as possible, but which can capture the essential physics of the two dimensional field and material structures observed in either simulation or experiment. In essence this model will test the hypotheses that the long conduction time plasma opening switch

- conducts for whatever time it takes for a low density channel to form and to penetrate the plasma annulus by an essentially advective process, and
- opens through the combined processes of magnetic insulation, gap erosion, and hydrodynamic expansion.

The central points of departure from previous attempts are fourfold. First, although it is only resolved axially, the field theory remains fully electromagnetic in order to account properly for the interaction of the POS region and the other machine elements. Second, the emission from the cathode is axially resolved and self consistently calculated with the local magnetic field included, in order to account for the ion erosion and gap dynamics as the conduction phase progresses. Third, the axial charge separation in the higher density regions is calculated self consistently from a modified two fluid description in order to make the axial electric field a causal factor in the axial flow of the bulk plasma. Fourth, the neutral component is included at the cathode emission surface in order to address the long timescale phenomena known to be important in ion diode physics<sup>23</sup>.

The PRS/Decade theory task developments fall into the four major elements: (i) the required additional theory for the transmission line, (ii) the warm magnetized emission for the POS, (iii) the Vlasov picture of the nearly collisionless bulk plasma conduction and axial convection, and (iv) the gap dynamics, are developed and some illustrations of their implications are given. The first two are treated below.

## **B. Transmission Line Model Upgrades**

Because we will simplify the fluid description of the POS by discussing radial profiles in number density and injection velocity that are self-similar in their axial response to the electromagnetic stresses imposed by the generator, the normally complex 2-D electrodynamics usually present in a POS can be reduced to the evolution of a TEM mode in a transmission line. Resolving the continuous transmission line into discrete units of inductance ( $L_j$ ) in series with the load and capacitance

( $C_j$ ) in parallel with the load, the POS component requires the addition of shunts ( $Z_{s,j}$ ) across the line. When shunts are set in the line the voltage advance is accomplished using an integrating factor of the form  $e^{-Z_s \alpha / Z_{s,j}}$ . A set of shunts for the POS model usually spans only two to four nodes of the main transmission line. The line fields are interpolated to the finer axial POS mesh. These interpolated fields provide drive conditions for the emission into the sheath gap or depletion channel, and the resulting impedance from the parallel combination of these shunts is summed back to the primary line grid to set the local shunt impedance  $Z_{s,j}$ . Here the parameter  $\alpha = ch_t/h_x \leq 0.5$  is the Courant number, the time step is seen to be a fraction  $\alpha$  of the transit time along an element. In the difference equation forms below a leading superscript denotes the time level, a trailing subscript, the spatial position, with a capital subscript denoting the largest index on the spatial mesh. The spacetime grids are fully interlaced, viz. the voltages and shunt variables computed at nodes on the "full" step and the intervening currents at the mid points of the inductances are computed on the "half" step. The discretization unit in space is the "light-nanosecond" ( $\approx 30$  cm) so that if one runs the clock in nanoseconds the only remaining dimensions in the theory are electrical. Voltages, currents, and impedances in the transmission line are then expressed in kV, kA, and  $\Omega$ . Both  $Z_{s,j}$ , the shunt impedance, and  $Z_j$ , the line impedance, can be spatially and temporally variable – but they are defined at coincident spatial positions within the line. Because the spatial discreteness is set to a constant value  $h_x = c\tau$ , allowing all elements to be stepped together in time, one must generally choose a small spatial unit and gather many together to make up the actual element of the model transmission line. In doing this the impedance of a line section is adjusted in order to keep the inductance fixed in the transformation, viz.  $\tau \sum_{j=1}^{j=K} Z_j = L_K$ , with the various  $L_K$  derived from the physical specifications of the target machine. If the actual delay time in a machine element is either more or less than the chosen integral number of line units, then the section's impedance is adjusted to retain the true inductance. Including the shunts the telegrapher's equations can now be written as difference equations in the semi-dimensionless form

$${}^{n+1}V_j = {}^nV_j e^{-Z_s \alpha / Z_s} - (1 - e^{-Z_s \alpha / Z_s}) Z_s ({}^{n+1/2}I_j - {}^{n+1/2}I_{j-1}),$$

$$(\mathcal{D}_- {}^{n+1/2}I)_j = (\mathcal{D}_+ {}^{n-1/2}I)_j - \frac{\alpha}{Z_j} ({}^nV_{j+1} - {}^nV_j),$$

where the matrix operator

$$\mathcal{D}_{\pm} = (\mathcal{I} \pm \gamma \alpha \nabla^2)_{ij} ,$$

introduces an adjustable damping parameter

$$\gamma \approx \frac{1}{8} \propto \frac{k_{Nyq}}{k_{damp}}$$

which controls the dispersion of the method at high wavenumber. By damping out the large wave number components, the tendency of these difference equations to propagate higher wavenumbers more slowly is mitigated and low wavenumber pulse shapes are then transmitted with low harmonic distortion.

At the boundaries and in those sections equipped with shunts, the damping is set to zero. For the internal shunt sections the time advance is done as above, with a modified dispersion matrix which turns off the adjustable damping parameter at the shunt nodes. For the end points, the combination of exterior circuit elements and the local currents on the transmission line then fixes the time advanced currents and voltages through:

$${}^{n+1/2}I_o = {}^{n-1/2}I_o - \frac{\alpha}{Z_o} ({}^nV_1 - {}^nV_o) ,$$

$${}^{n+1/2}I_J = {}^{n-1/2}I_J - \frac{\alpha}{Z_J} ({}^nV_{J+1} - {}^nV_J) ,$$

$${}^nV_o = \frac{Z_o \tau V_s(t) + L_o {}^nV_1}{Z_o \tau + L_o} ,$$

$${}^nV_{J+1} = \frac{\tau Z_J {}^nI_J Z_L(t) + L(R) {}^nV_J}{\tau Z_J + L(R)} ,$$

where the time derivative of current has been eliminated in favor of the appropriate voltage differences and  $\tau$  is the single element delay interval. The source voltage  $V_s(t)$  can be derived through a variety of models, e.g., a fixed waveform, or a computed capacitive discharge into an inductive store, or a Marx bank. Particular examples exist for all these options for various DNA pulsers. The load is modeled as one of a variety of elements, ranging from a fixed matching impedance to a full 0-D PRS model. So long as the load behavior can be characterized by the (possibly time dependent) parameters of radius ( $R$ ), inductance  $L(R,t)$  and resistance  $Z_L(R,t)$ , then the element can be folded into the present picture.

For each POS section of the line which is decomposed as an axially distributed sequence of shunt paths, each path makes contact with the anode and cathode through a plasma sheath model and if necessary any internal resistance of the path is added in series with the impedance of the sheaths, c.f. Fig.1 where the field and current components are displayed. The shunt comprises two sheath sections and an annular plasma subject to the electromagnetic  $E, B$  and drift  $U, W$  fields shown. The input (upstream) current is  $I_j$ , the surviving output (downstream) current is  $I_{j+1}$ , which is the basis for the ambient magnetic field in the switch. The electron current "beam" flux  $\Gamma_{e,r}$ , shown leaving the cathode sheath in the figure, will have different collection behavior at high and low density. Under high density conditions the "beam" current will not penetrate the switch plasma very far, it will be stopped and returned to the "anode side" surface of the sheath or density depletion channel. In this limit the switch plasma is decoupled from the shunt and the corresponding voltage drop over that part of the circuit will be vanishingly small. As the switch plasma density decays the injected "beam" flux  $\Gamma_{e,r}$  penetrates into the switch plasma. The ambient magnetic field in the switch plasma will thus depend upon the ability of that injected flux to penetrate to the anode sheath for collection. Once collected it will connect the "switch plasma" portion of the shunt back into the circuit, feed an axial (ambipolar) electric field, and (if resistive turbulence arises) provide some additional voltage drop to that in the gap. The ambient magnetic field in the sheath or depletion channel will still determine the level of magnetic insulation, whatever the collection pattern is at the anode. This model is therefore equipped with an emission theory which covers all degrees of magnetic insulation accessible to the plasma, near the cathode or in any depletion channel which occurs between the anode and cathode.

How much or how little influence can magnetic insulation have over the shunted power flow in an interesting line geometry? If power is to flow past any such POS element, then  $Z_{s,j} \gg Z_j$  must hold, but what results for a shunt attenuation which is based on the Child-Langmuir gap impedance which depends on the voltage. Such a question can only be answered in the context of a transmission line calculation which establishes a typical voltage range across the shunt. Knowing nothing about the switch plasma properties, the electrical characteristics alone of such space-charge limited gaps figure heavily in the electrodynamics of the pulser. As an illustration of the ability of space charge limited gaps to attenuate the incoming current pulse, we have calculated in Fig.2 the space-time history of a POS model line for a sheath

gap held fixed in time but otherwise allowed to become magnetically insulated if demanded by local currents and voltages. If there were no magnetic insulation model, the energy would never have reached the (matched)load. The result shown in Fig.2c would not obtain for **any allowed gap size**. The voltage operating range ( $\geq 100\text{kV}$ ) in these calculations places any uninsulated gap in a very low impedance state and no energy would get through. Here, if we add an insulation model and allow a POS shunt attenuation to fall to zero as the current exceeds that required to insulate a given gap size:

$$I_j > I_{crit} = 13.6 \frac{R_{cath}}{D_{shth}} \sqrt{(1 + 1.96 \cdot 10^{-3} V_{j,kV})^2 - 1} \text{ [kA]},$$

then the switch plasma presents an impedance large enough to get energy to the load when a large enough gap is reached. Prior to reaching the critical current the shunt attenuation scales  $\propto \sqrt{V_j} D^{-2}$  and still shows very effective containment of the energy in the upstream inductive store. In this test the cathode radius was 5 cm, the POS section was 12 cm long, filled at an ion density of  $10^{12} \text{ cm}^{-3}$  with doubly ionized carbon at 10 eV. The plasma motion was not resolved in this particular test. Under these conditions the Debye length is about  $2.3 \cdot 10^{-3} \text{ cm}$ , and the collisionless skin depth is about 0.375 cm. As the gap dimension varies through  $(15 \rightarrow 500) \lambda_{Debye}$ , the energy transfer to the load jumps up quickly as the gap size parameter crosses the value corresponding to 2 mm and saturates thereafter. Smaller gaps don't allow a significant energy transfer, while larger gaps don't allow much more energy through than that computed at  $D = 125 \cdot \lambda_{Debye}$ .

Apparently this 2 mm gap size, inferred from recent NRL experiments, is a natural, **electrically determined** channel dimension for any pulse line similar to that in the HAWK device. Nothing in the model forces the power flow to be enhanced at 2mm, it just works out this way from simple electrical requirements, and this clearly reinforces the fact that magnetic insulation of the gap or low density channel is crucial to the opening process – the impedance of a pure Child-Langmuir gap, no matter how wide is simply too low to allow any power transfer. In other words the **"erosion" of a Child-Langmuir gap as envisioned in the original NRL Model cannot ever be the dominant opening mechanism** in these switches. In these calculations the penetration of energy to the load does not occur until most of the POS line shunts experience  $I > I_{crit}$  for most of the time. If any one or two of the shunt's had not been allowed to insulate or had a gap size much smaller than the

average, the power flow would have been substantially reflected for all values of the average gap size.

### C. POS Theory Development

Simply boosting the impedance when  $I > I_{crit}$  is little more than a good first cut, giving rise to a lot of noise in the POS calculation domain. A more complete theory of the emission requires (i) a treatment of the electron orbits entering any gap, (ii) a treatment of the space charge limitations on this flow for a given potential across the gap, and (iii) the use of (at least) a Maxwellian distribution of initial velocities at the emission surface. Such a warm emission model improves the sheath picture in two ways:

- the theory becomes applicable to an axial, low density channel opened away from the physical location of the cathode, and
- the singularities of cold emission theory are smoothed out and this will be reflected in a smooth transition to magnetic insulation.

A primary element of the emission model is an integration of the appropriate particle orbits in the applied  $E_r$  and  $B_\theta$  fields. For simplicity the present analysis is nonrelativistic, but the generalization is straightforward. With  $r_o$  the effective cathode radius,  $D$ , the gap width, and  $\lambda_o \equiv D/r_o$ , the radial electric field can be written  $E_r = -\frac{V_j^{gap}}{D} \frac{\partial \Psi}{\partial \xi}$ , with the radial coordinate normalized to the gap, viz.  $\xi = \frac{r-r_o}{D}$ , and the potential normalized to the local line voltage (diminished by any resistive drop in the bulk plasma and anode sheath, and denoted  $V_j^{gap}$ ). The magnetic field is related to the downstream current by  $B_\theta = \frac{2I_{j+1}}{cr}$ , which serves to define the cyclotron frequency at the emission surface,  $\Omega_o = \left(\frac{2e}{m_e c^2}\right) \frac{I_{j+1}}{r_o}$ , equivalent to a circulation velocity  $v_{\Omega_o} = r_o \Omega_o$ . It is convenient to normalize this and all other velocities in the problem to the electron thermal speed so that the dimensionless parameter  $\beta \equiv \frac{r_o \Omega_o}{v_{th}} = \sqrt{\frac{2e^2}{m_e T_o}} \frac{I_{j+1}}{c^2}$  appears as one of two natural scaling variables. The second velocity ratio is related to the gap voltage, viz. if  $v_{\Phi>}^2 = \left(\frac{2eV_j^{gap}}{m_e}\right)$  denotes the maximum free fall velocity in the applied electric field, then  $v_\Phi(r) = v_{\Phi>} \sqrt{\Psi(r)}$  is the spatial profile of this velocity, and the dimensionless ratio  $\gamma = \frac{v_{\Phi>}}{v_{th}}$  sets the energy scale of the problem relative to the thermal electron energy.

The nontrivial equations of motion can be written compactly in terms of these scaling quantities

$$\ddot{z} = \dot{v}_z = -v_{\Omega_0} \frac{\dot{r}}{r}$$

$$\ddot{r} = \dot{v}_r = \frac{1}{2} v_{\Phi}^2 \partial_r \Psi(r) + \left( \frac{v_z v_{\Omega_0}}{r} \right) + r \dot{\theta}^2 .$$

The first integrals are likewise straightforward, including the  $r^{-1}$  variation of the fields in logarithmic factors, so that

$$v_z(r) = v_{oz} - v_{\Omega_0} \ln \left( \frac{r}{r_0} \right) \equiv v_{oz} - v_{\Omega}(r)$$

$$v_{\theta}(r) = v_{o\theta} r_0 / r$$

$$v_r^2 = v_{r_0}^2 + v_{\Phi}^2(r) + 2v_{oz} v_{\Omega}(r) - v_{\Omega}^2(r) + v_{o\theta}^2 \left( 1 - \frac{r_0^2}{r^2} \right) .$$

An important role is played by the angular momentum  $\mathcal{L}_0 = m_e r^2 \dot{\theta}$ . Conserved in this "central force" problem, it modifies the turning points of the orbits. At  $r \rightarrow r_0$  the effect is minimal, as  $r \gg r_0$  the loss of azimuthal speed with increased radius keeps the energy in the radial motion and provides a positive contribution to  $v_r^2$ .  $\mathcal{L}_0$  thus moves the turning points outward and spreads them in space relative to the cold emission picture. A second important constant of motion is the initial (emitted) kinetic energy,

$$\mathcal{E}_0 = v_{or}^2 + v_{oz}^2 + v_{o\theta}^2 = v_r^2(r) + v_z^2(r) + v_{\theta}^2(r) - v_{\Phi}^2(r) \quad \forall r ,$$

which forms the basis of a Vlasov solution in the spatial domain of interest, viz.

$$f_0 = \left[ \frac{m_e}{2\pi T_e} \right]^{3/2} n_0 \exp - \frac{m_e}{2T_e} (v_r^2(r) + v_z^2(r) + v_{\theta}^2(r) - v_{\Phi}^2(r))$$

is a time invariant distribution for any electrostatic profile  $\Psi(r)$ . Solving the non-linear Poisson problem discussed below establishes the details of the Vlasov solution but it will always have the structure shown above if the emission surface is characterized by a Maxwellian electron distribution. The time invariance of this solution is readily established by noting that

$$v_r \left[ \left( \frac{e V_j^{gap}}{m_e} \right) \partial_r \Psi(r) + \frac{v_{\theta}^2}{r} \right] \frac{m_e}{T_e} f_0 \equiv v_r \partial_r f_0 \equiv -\vec{a} \cdot \partial_v f_0 .$$

Using these orbit properties it is possible to express initial velocities in terms of final velocities, or vice versa. When the final velocities at any given  $r$  value are

regarded as the output of the mapping, keeping  $v_r$  real requires

$$v_{z0} \geq v_{zom}(r) \equiv \frac{v_{\Omega}^2(r) + v_{o\theta}^2 \left( \frac{r^2}{r_0^2} - 1 \right) - (v_{r0}^2 + v_{\Phi}^2(r))}{2v_{\Omega}(r)}$$

and any orbit with  $v_{z0} < v_{zom}(r)$  turns before radius  $r$  is reached. When the initial velocities are to be recovered from the final ones, keeping  $v_{or}$  real requires a different constraint

$$v_z \leq v_{zmax}(r) \equiv \frac{v_r^2(r) - \left( v_{\Omega}^2(r) + v_{\theta}^2 \left( \frac{r^2}{r_0^2} - 1 \right) + v_{\Phi}^2(r) \right)}{2v_{\Omega}(r)}$$

and any orbit with  $v_z > v_{zmax}(r)$  is excluded from the Vlasov problem. If one examines the various orbit classes shown in Fig. 3, then clearly position and velocity on the emission surface vary according to these rules when mapping orbits into a "collection parcel" at the outer boundary of the problem. Orbits with greater initial axial velocities originate in  $z$  directly across from the collection point. Lesser initial axial velocities must come from higher in  $z$ , however, in order to meet the collection parcel with some remaining radial velocity. The cycloidal repetition of the orbits is also mapped onto the  $v_{oz} < 0$  domain because, whether a particle is absorbed into the cathode cloud (and exchanged for an emitted one), or reflected off specularly from the cathode surface, the velocity remains the same. Due to this remapped character of the orbits, the criteria for axial uniformity in  $E_r$ ,  $B_{\theta}$ , and the background density  $n_o$  can be based only on the electron Larmor radius, viz.

$$r_e < \left\{ \frac{E_r}{\partial_z E_r}, \frac{B_{\theta}}{\partial_z B_{\theta}}, \frac{n_o}{\partial_z n_o} \right\},$$

only when scattering after emission is included will the fluxes come from far away in  $z$ . In case of such scattering the orbits will detach from the emission surface and can be brought to any collection parcel from much further upstream. The scale length criteria therefore see  $r_e$  replaced by the mean free path for momentum transfer in any neutral components to be included in the cathode or emission surface model. Material scattered into such orbits will form a semi-collisional gyrokinetic component in the low density plasma. If enough such material is in any sheath or depletion channel, then the propagation of signals downstream will be slowed to the local Alfvén speed and substantially lengthen the timescale for energy to soak past the POS. In effect the sheath or depletion channel will appear as a plasma filled waveguide, magnetized by the current arc at its downstream termination.

From the Vlasov solution the electrostatic problem requires two moments – number density and radial flux. The velocity space integrations are quite complex if an unfortunate choice of variables is made; choosing between initial or final coordinate representations is often helpful. The Jacobian determinant allows moments to be taken in term of either set of phase space coordinates,  $\mathbf{v}(\mathbf{r})$ , or  $\mathbf{v}_o$ .

$$\Delta \equiv \left| \frac{\partial \bar{\mathbf{v}}}{\partial \bar{\mathbf{v}}_o} \right| = \left| \begin{bmatrix} \frac{v_{o\theta}}{v_r(r)} & \frac{v_{o\Omega}(r)}{v_r(r)} & \frac{v_{o\phi}^2 \left(1 - \frac{r^2}{r_o^2}\right)}{v_r(r)} \\ 0 & 1 & 0 \\ 0 & 0 & r_o/r \end{bmatrix} \right|$$

so that  $\Delta = \frac{r_o v_{o\theta}}{r v_r(r)}$  and, thus  $d^3 v = \Delta d^3 v_o$ .

The moment calculations can be summarized as follows, with the radial domain  $[r_o, \infty) \rightarrow [0, 1)$  mapped by the parameter  $\eta \equiv (r - r_o)/r$ , the flux moment is most conveniently computed using the final variables, while the relative number density is most easily done using the original variables

Let  $\Gamma_{e,th} = \frac{e}{2} \delta z r n_e(r) V_{th}$  be the thermal flux from the cathode, one can formulate the magnetically insulated flux as  $\Gamma_{e,r} = \Gamma_{e,th} \cdot \gamma_{er}(\Phi, \Omega_o \ln(1/1 - \eta), \eta)$  where

$$\gamma_{er}(\Phi, \Omega, \eta) \equiv 2 \left[ \frac{m_e}{2\pi T_e} \right]^{3/2} \int_{-\infty}^{\infty} dv_{\theta} \int_0^{\infty} dv_r \int_{-\infty}^{v_r^{\max}} dv_z \frac{v_r}{v_{th}} \exp - \frac{m_e}{2T_e} (v_r^2 + v_z^2 + v_{\theta}^2 - v_{\Phi}^2)$$

and, one can obtain a similar result for the relative number of particles which survive at a given radius  $n(r) = n_o H(\Phi, \Omega, \eta) = n_o \frac{r_o}{r} \Lambda(\Phi, \Omega_o \ln(1/1 - \eta), \eta)$ , given by

$$\Lambda(\Phi, \Omega, \eta) \equiv 2 \left[ \frac{m_e}{2\pi T_e} \right]^{3/2} \int_{-\infty}^{\infty} dv_{o\theta} \int_0^{\infty} dv_{or} \int_{v_{zom}}^{\infty} dv_{oz} \frac{v_{or} \exp - \frac{m_e}{2T_e} (v_{or}^2 + v_{oz}^2 + v_{o\theta}^2)}{\sqrt{2} (v_{oz} - v_{zom}) v_{\Omega}(r)}$$

In Fig. 4 the functions  $\Lambda(\Phi, \Omega, \eta)$  and  $\gamma_{er}(\Phi, \Omega, \eta)$  are illustrated for a general domain in the energy and magnetization parameters. The limiting case of the nonmagnetized gap is recovered most clearly in the behaviour of the average radial speed (Fig 4b) surviving at a given gap size ( $\eta = 0.75$ ). What one plots is the function

$$\frac{\langle v_r \rangle}{v_{th}} \equiv \frac{\Gamma_{er}}{n(r) v_{th}} = \frac{r \gamma_{er}(\Phi, \Omega, \eta)}{r_o \Lambda(\Phi, \Omega, \eta)}$$

and it is seen to drive this speed up monotonically for low magnetization, but curtail it substantially when the magnetic field gets stronger.

## Warm Magnetized Emission Model

When the potential profile  $\Phi$  is no longer a free parameter and the magnetic field profile is described by the linkage of  $\Omega$  with specific gap data, then the formulation above provides a kernel for the nonlinear Poisson problem. The assumptions of the emission model can be stated as follows

- i. there exists a Maxwellian distribution of emission off the interior radius at a fixed temperature,
- ii. collection at the exterior radius is irreversible, viz. any orbit which goes beyond the outer radius is presumed to be scattered and lost,
- iii. the timescale for changes in the boundary conditions at the interior and exterior radii is long compared to the electron transit time across the gap under conditions of equilibrium space charge limited emission, and
- iv. the ions thermal energy is small relative to either that of the electrons or the free fall energy across the gap to the cathode side.

Upon making the substitutions

$$\Phi = \gamma \sqrt{\Psi(\xi)} \quad \Omega = \beta \ln(1/1 - \eta) \quad \eta \equiv (r - r_o)/r = D\xi/(r_o + D\xi)$$

one is lead in turn to the following formulation of the Poisson problem in the gap

$$(\lambda_o + \xi)^{-1} \partial_\xi((\lambda_o + \xi) \partial_\xi \Psi) = \mathcal{K}(s_{oe}, \alpha, \Psi(\xi))$$

$$\mathcal{K}(\Psi(\xi)) = s_{oe} \left[ \left( \frac{\gamma r_o}{r_o + D\xi} \right) \frac{\Lambda(\gamma \sqrt{\Psi(\xi)}, \beta \ln(1/1 - \eta), \eta)}{\gamma_{er}(\gamma, \beta \ln(1/1 - \eta), \eta)} - \frac{\alpha}{\sqrt{1 - \Psi(\xi)}} \right]$$

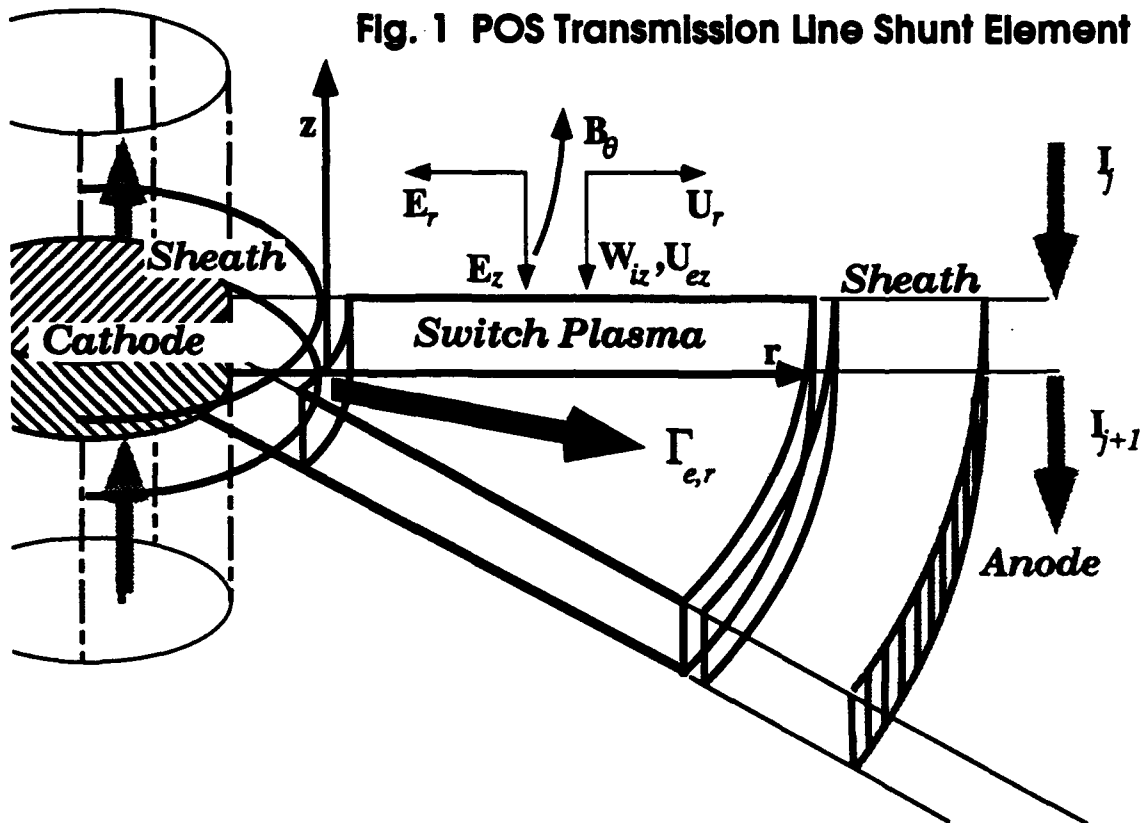
$$s_{oe} = j_{oe} \frac{D^2}{V_j^{3/2}} \left[ 2^{3/2} \pi \sqrt{\frac{m_e}{e}} \right] \quad \alpha = \frac{j_{oi}}{j_{oe}} \sqrt{\frac{m_i}{Z m_e}}$$

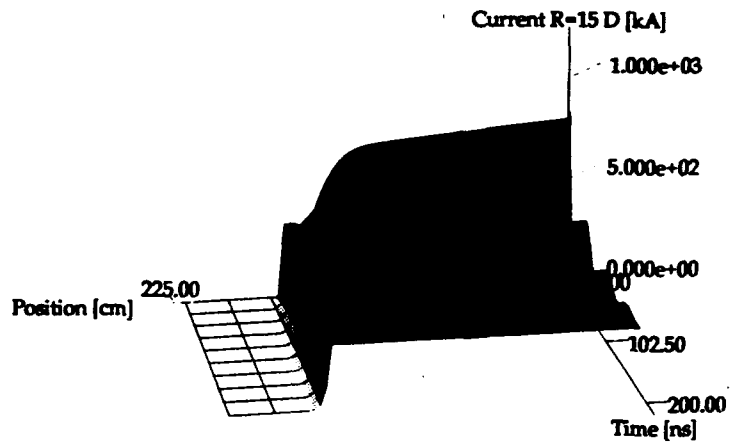
that reduces to the Child-Langmuir limit for cold emission and no magnetic field. The two free parameters,  $s_{oe}$  and  $\alpha$ , in the solution above must be determined from the boundary conditions at  $\xi = 0$  and  $\xi = 1$ . Enforcing the constraints  $\partial_\xi \Psi(0) = \partial_\xi \Psi(1) = 0$  and  $\Psi(1) = 1$  is sufficient to determine these quantities and predict an impedance for any such region. The impedance of the shunt  $Z_{sj}$  then becomes a function of the line parameters  $\beta_j$  and  $\gamma_j$  because these determine  $s_{oe}$  and  $\alpha$ . One can write shunt impedance in the general form

$$Z_{sj} = \frac{D_j^2}{\sqrt{V_j^{gap}} r_o \delta z} \sqrt{\frac{m_e}{e}} \frac{1}{s_{oe}(\beta_j, \gamma_j) [1 + \alpha(\beta_j, \gamma_j) \sqrt{\frac{Z m_e}{m_i}}]},$$

and hence make contact with the transmission line formulation above.

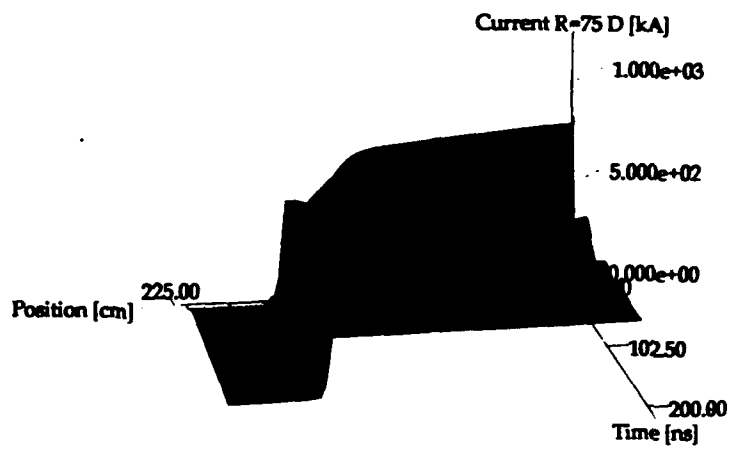
Fig. 1 POS Transmission Line Shunt Element





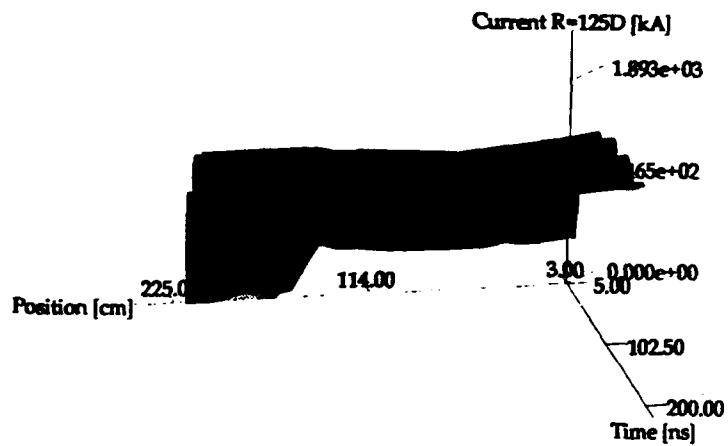
Current R=15 D [kA] vs. ( Position [cm], Time [ns] )

Figure 2a



Current R=75 D [kA] vs. ( Position [cm], Time [ns] )

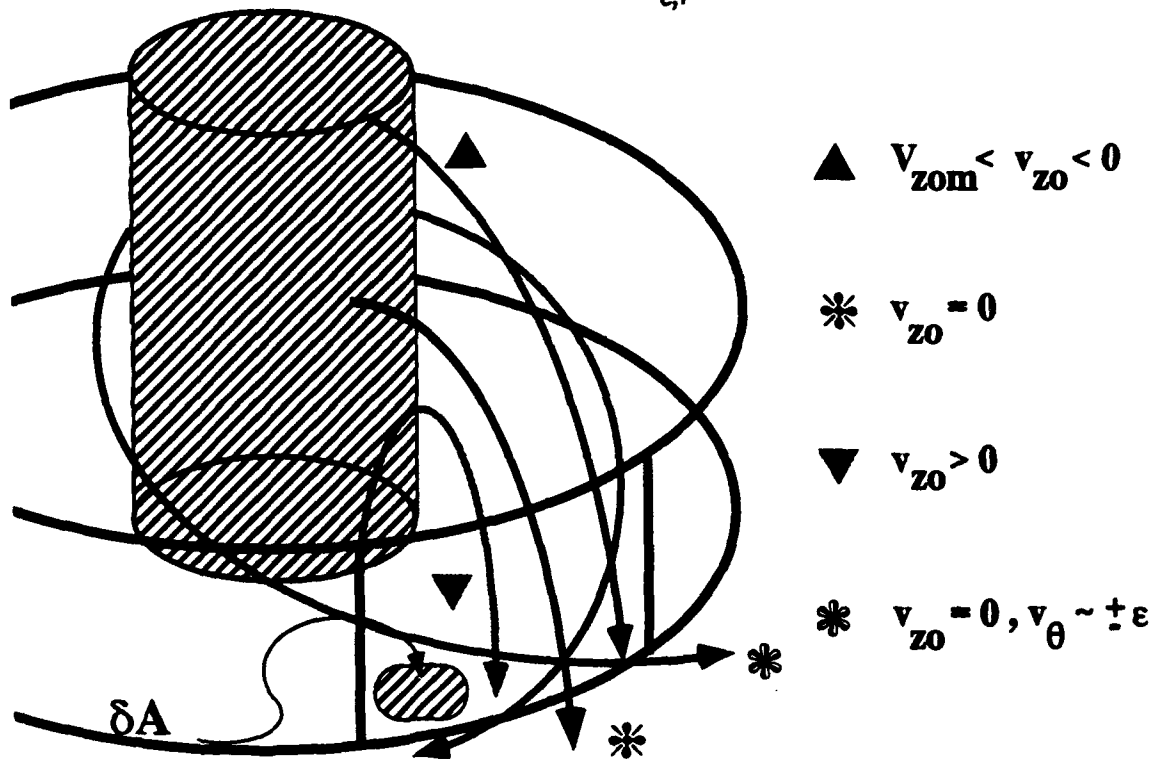
Figure 2b

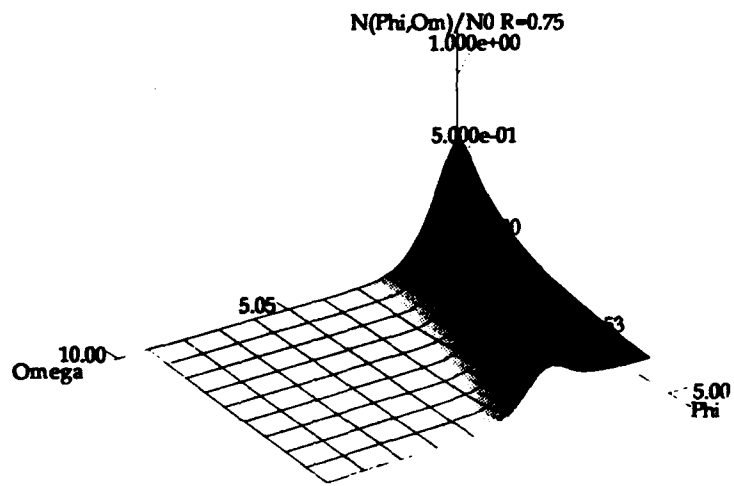


Current R=125D [kA] vs. ( Position [cm], Time [ns] )

Figure 2c

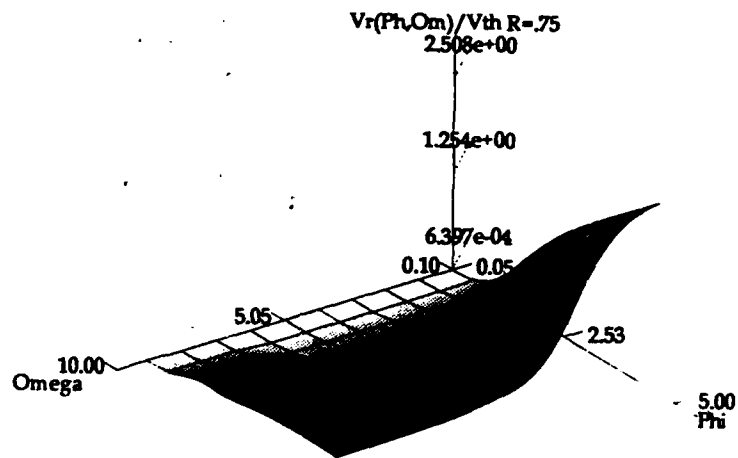
Fig. 3 Orbits Contributing to  $\Gamma_{e,r}$





$N(\Phi, \Omega)/N_0 R=0.75$  vs. (  $\Omega$ ,  $\Phi$  )

Figure 4a



$V_r(\Phi, \Omega) / V_{th} R = .75$  vs. (  $\Omega$ ,  $\Phi$  )

Figure 4b

## V. The Effect of 2-D MHD Flows on Gas Puff PRS Performance/Optimizing Gas Puff Nozzle Designs

In one of the important PRS (Plasma Radiating Source) concepts, a gas puff of neon, argon, or krypton is coupled to a pulse power device in order to produce a burst of x-rays which can then be used for simulation or testing purposes. For many years, imploding gas puffs of neon and argon have been successfully used in these devices to emit copious quantities of K-shell X-rays. However, several nagging problems have remained in the understanding, optimization, and scaling of these experiments. First, the radiation pulse which is observed experimentally is broader and shows irregularities that are not reproduced in 1-D simulations. Second, time integrated X-ray images taken during gas puff implosions at Physics International and other laboratories of gas puff implosions reveal axial plasma motions which play an important role in determining the quality of the implosion and the X-ray production.

A close working relationship between Physics International and NRL has recently produced an improved body of knowledge about the influence of 2-D flow processes which take place in these gas puff pinches on kinetic energy and X-ray generation from these plasmas. To that end, we have been focusing over the past several years on calculating the two-dimensional effects which are present in these gas puff implosions as a consequence of the nozzle flow that initiates these experiments.

During the past fiscal year, we have looked at the dynamics of gas puff Z-pinch implosions from the viewpoint of helping to understand experiments at Physics International, Inc. In these experiments, the nozzle design used in PRS gas puff experiments was varied in an attempt to optimize not only the total radiative yield, but also the FWHM of the pulse and the peak radiative power. The most striking results have come from tilting the nozzles inward to reduce the zippering effect. In these experiments, the zippering effect was reduced to less than 10 nsec in some cases. Zippering occurs when the plasma implodes on axis at different times. This is due to the spread of the initial gas profiles along the axis caused by expansion of

the gas away from the nozzle. We shall discuss simulations of these experiments in this report.

In order to simulate these pinches, we have used our code, PRISM, operating in a Lagrangian-Eulerian formulation. That is, the fluid variables are moved forward in time using a Lagrangian prescription and then the mesh is adjusted back to its original position with the appropriate advectations taken into account. At the end of a computation cycle, the result is similar to that of an Eulerian code. The set of equations used in the 2-D model are:

$$\frac{d\rho}{dt} = -\rho \vec{\nabla} \cdot \vec{u}, \quad (1)$$

$$\rho \frac{d\vec{u}}{dt} = -\vec{\nabla}(P_e + P_i + Q_a) + \frac{\vec{J} \times \vec{B}}{c}, \quad (2)$$

$$\frac{d\epsilon_e}{dt} + P_e \frac{dV}{dt} = -V \vec{\nabla} \cdot \vec{q}_e + V \eta J^2 + \dot{P}_{rad} + V \dot{C}_{ei}(T_i - T_e), \quad (3)$$

$$\frac{d\epsilon_i}{dt} + (P_i + Q_a) \frac{dV}{dt} = -V \vec{\nabla} \cdot \vec{q}_i + V \dot{C}_{ei}(T_e - T_i). \quad (4)$$

To these equations are added Maxwell's equations, viz.,

$$\vec{\nabla} \times \vec{B} = \frac{4\pi}{c} \vec{J}, \quad (4)$$

$$\vec{\nabla} \times \vec{E} = -\frac{1}{c} \frac{\partial \vec{B}}{\partial t}, \quad (5)$$

along with Ohm's law,

$$\vec{E} = \eta \vec{J} - \frac{\vec{u} \times \vec{B}}{c}. \quad (6)$$

In Eqs. (1)-(6)  $P_{e,i}$  are the material pressures for electrons and ions,  $\epsilon_{e,i}$  are the specific energies,  $\rho$  is the density,  $V$  is the inverse of the density,  $\vec{q}_{e,i}$  are the heat fluxes,  $\dot{C}_{e,i}$  is the electron-ion energy exchange term, and  $\eta J^2$  is the ohmic heating. The  $\dot{P}_{rad}$  term in Eq. (3) is the radiation source or sink term. In Eqs. (3) and (4),  $Q_a$  is an artificial viscosity used for numerical stability in regions of strong compression. The SESAME tabular equation of state was used to determine temperatures,

average charge states, and specific heats from densities and specific energies. In addition, the magnetic field on the outside of the mesh is specified through either a circuit equation or a prescribed temporal behavior.

We ran simulations which represented two different nozzles: a "thick" nozzle which had a nozzle exit diameter of 0.8 cm and a nozzle diameter of 2.5 cm, and a "thin" nozzle which had an exit diameter of 0.4 cm and a nozzle diameter of 2.5 cm. In turn, each of these nozzle designs was canted inward at three different angles (0, -7.5, and -10 degrees). In all cases, as in the PI experiments, the fill gas was argon with a linear mass density of 50  $\mu\text{gm}/\text{cm}$ . We used a prescribed current which matched the measured current provided by PI. Our goal in these simulations has been to provide input to the experimentalists about the direction one should go in optimizing the yield and/or power based on the choice of nozzle diameter, nozzle exit width, and nozzle tilt angle. In the simulations reported on here, we have concentrated on the last two parameters.

Figure 1 shows the initial nozzle density (logarithmic as indicated by the shaded bar) profiles for the 0 and -10 degree tilted nozzles (0.4 cm exit width). The gas expands outward from the exit (at  $z=0$  cm) at a 10 degree angle up to a total length of 3 cm. This value for the expansion is imposed in the initialization procedure and is based on the value measured in the experiments. The peak density decreases with increasing  $z$  because the 50  $\mu\text{gm}/\text{cm}$  linear mass density is preserved along the axis. Notice that for the -10 degree tilted nozzle, the inward tilt exactly compensates for the expansion at the back edge. In Fig. 2, the radial and axial kinetic energy (normalized according to  $\eta = [\text{Kinetic Energy}/\text{Ion}] / [1.49Z^{3.51} \text{eV}/\text{Ion}]$ , where  $Z=18$  for argon) are plotted for the two cases. In Fig. 2 (a) the axial kinetic energy is comparable to the radial value and subsequently rises above the radial value due to zippering. In contrast to this, the axial kinetic energy is well below that of the radial value in the tilted case, as seen in Fig. 2 (b), until 110 nsec when the radial value is at a relative minimum due to stagnation on axis. The increase in axial energy is indicative of unstable activity rather than zippering. The minimum in  $\eta_r$ , and the delay in the onset of  $\eta_z$ , indicates that the implosion is much more uniform than the previous case and that zippering is minimized. This is demonstrated in the density plots of Fig. 3. Figure 3(a) shows the high density "spot" characterizing the

zippering phenomenon after it has moved partially up the axis. At subsequent times, this spot moves up the axis until it contacts the wall located at 3 cm. However, when the -10 degree tilt is applied to the nozzle, the implosion is much more uniform (although, spots which are presumably caused by  $m=0$  instability activity can be seen near the axis).

Finally, Fig. 4 shows a measure of the implosion based on the product of the ion density and electron density:

$$\frac{dQ}{dt} = \int n_i n_e dv$$

$$Q = \int \left[ \frac{dQ}{dt} \right] dt$$

where  $dQ/dt$  is normalized by  $10^{18} \text{cm}^{-3} 10^{19} \text{cm}^{-3} 1 \text{cm}^3$  and  $Q$  is further normalized by 10 nsec. Since in general this product can be related to the radiation intensity, it provides a first approximation of the shape and width of the radiation pulse. The results are plotted for the three tilt angles. It can be seen that both the narrowness and the height of the density product (i.e.,  $dQ/dt$ ) improves significantly as the tilt angle is increased. The integral of these curves with time,  $Q$ , also increases with increasing tilt angle, although, the increase is less dramatic. Figure 5 shows the same quantities plotted for the case where the exit nozzle width was increased to 0.8 cm and the same tilt angles were used. Both the instantaneous value and the total value,  $Q$ , are reduced. The pulse widths at the maximum of the  $dQ/dt$  curves are also narrower when the nozzle exit width is reduced.

In conclusion, we can say that zippering, as evidenced by lower values of  $\eta_z$ , is reduced substantially by tilting the nozzle inward. The best results are obtained when that value is near 10 degrees. The curve of density product versus time is also narrower when the nozzle is tilted. Also, the integral with time of the curves is larger with increasing tilt angle. Results with nozzles which have lower exit widths (0.4 cm) show improvement over the wider exit width nozzles (0.8 cm). We are continuing these studies with an investigation of the effects of the 2-D flow on the radiative behavior of the plasma. These results will be reported on early in the next fiscal year.

We are just beginning to understand the effects that nozzle design will have on optimizing PRS load design. The dramatic improvement in pulse quality produced in the PI experiments, which can be explained by the comparisons made with the 2-D computer simulations, are encouraging. In the future, machines with much larger currents, such as Decade, will mean that the issue of nozzle design will continue to be important. We will need to know the effects of the three parameters discussed above (nozzle diameter, nozzle exit width, and nozzle tilt angle) in the higher current, high flow rate regime. In addition, since mass loading will be higher, this must be taken into account in scaling these PI to Decade designs. A foundation from which to make these predictions will be built by further comparisons with Double Eagle (Physics International) and Saturn (Sandia National Laboratory) experiments, and by making more comparisons and benchmarks of the 2-D calculations against the more complete dynamical descriptions that are contained in the 1-D calculations.

### Figure Captions

Figure 1. Fill plots showing the initial density for: (a) straight nozzle, and (b) -10 degree tilted nozzle.

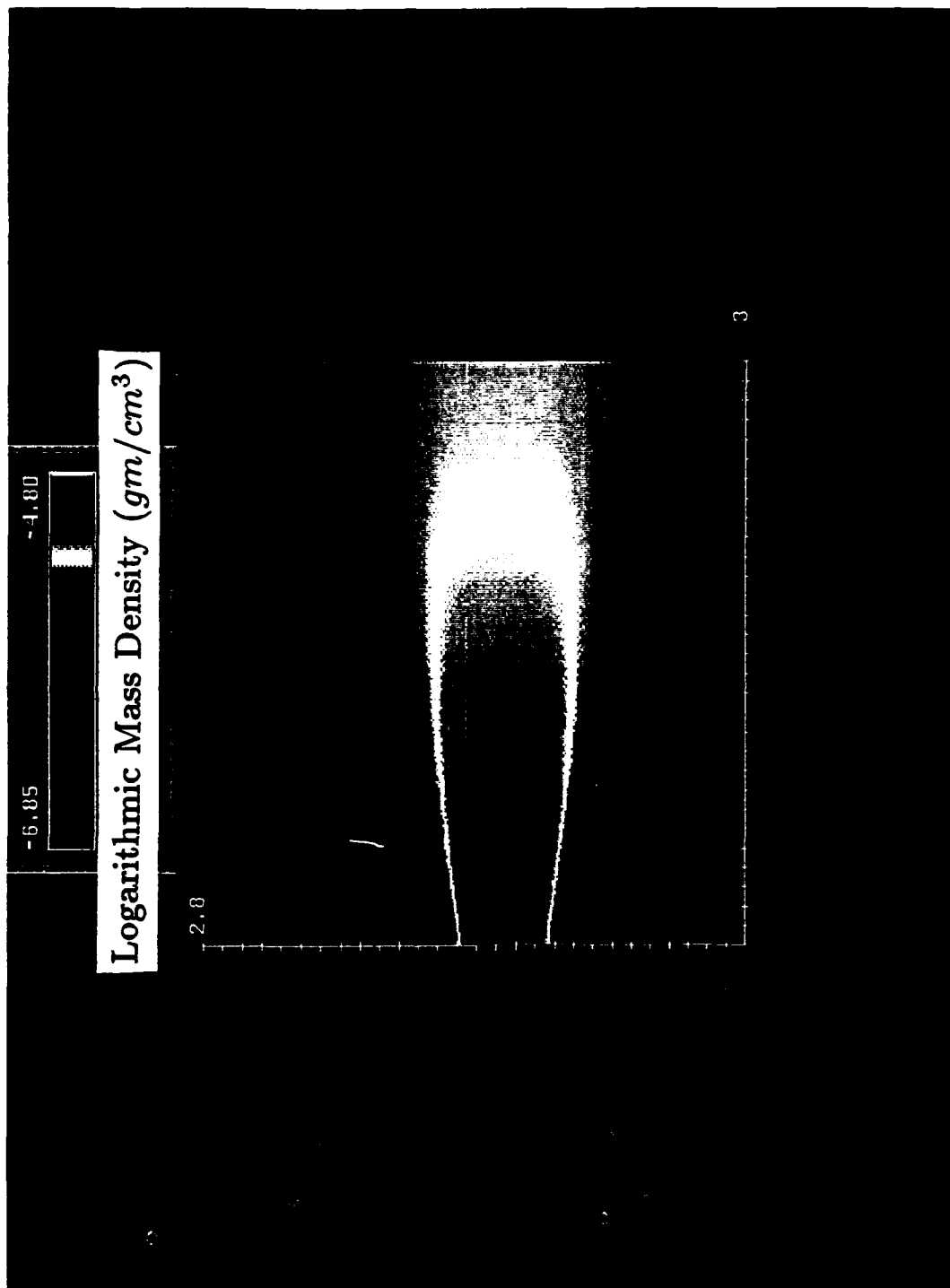
Figure 2. Radial and axial kinetic energy values for: (a) straight nozzle, and (b) -10 degree tilted nozzle.

Figure 3. (a) Moving high density spot created during the implosion of the plasma from the straight nozzle. (b) Density profile during the implosion of the plasma from the tilted nozzle.

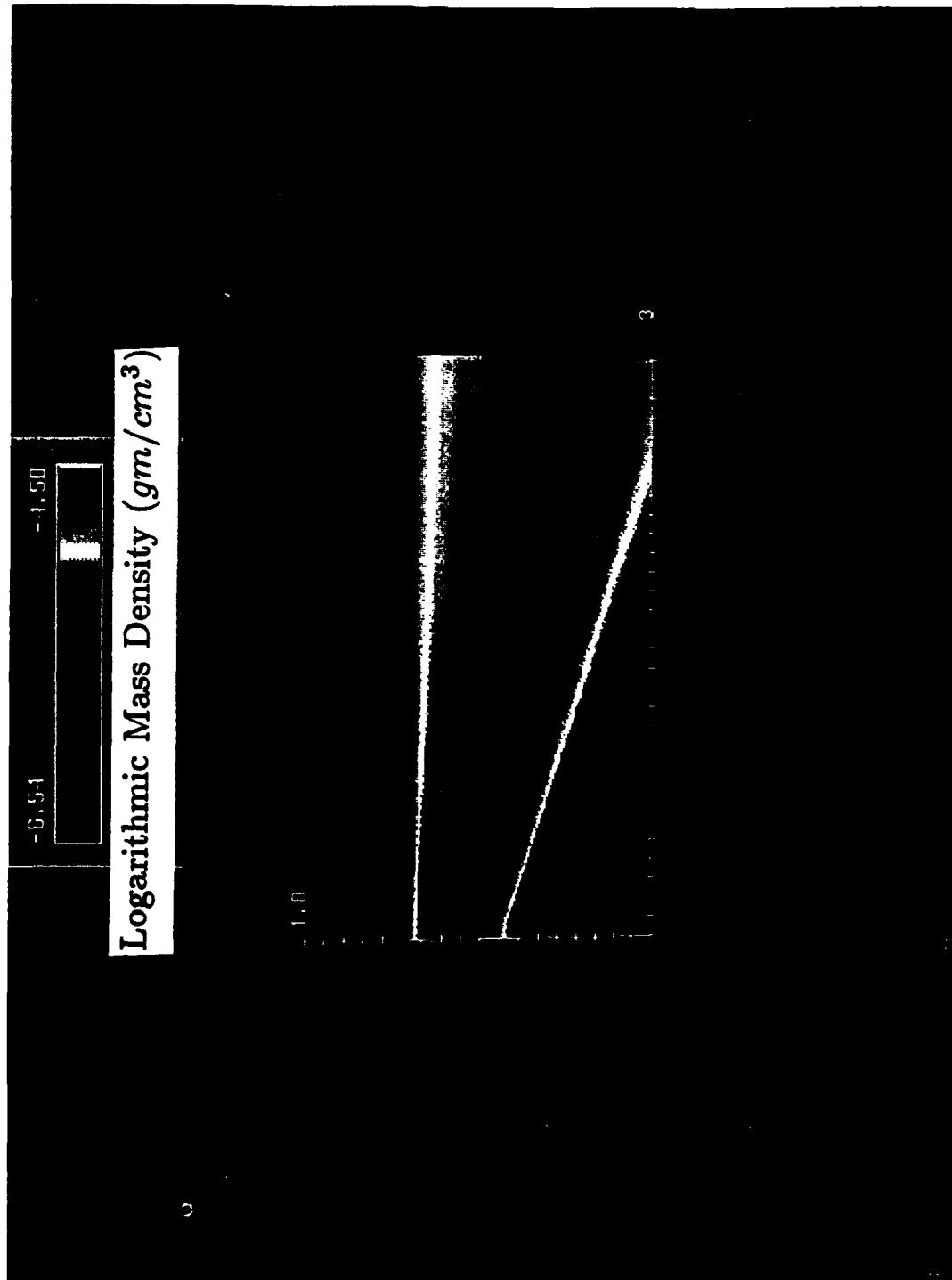
Figure 4. Values of  $dQ/dt$  and  $Q$  as a function of time for the three nozzles (0, 7.5, and 10 degree tilts).

Figure 5. Same as Fig. 4 but the exit width has been increased to 0.8 cm with the same fixed mass.

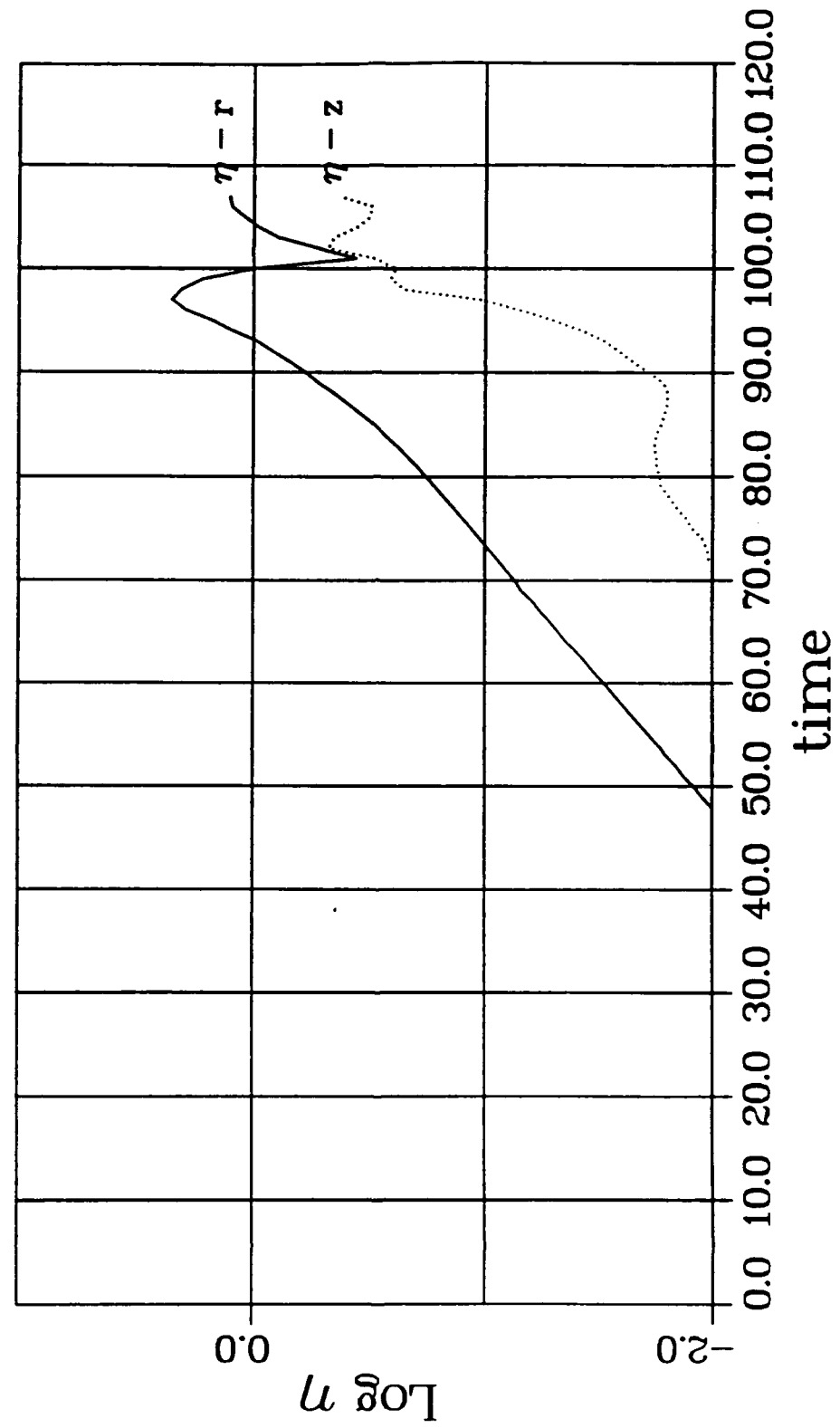
Nozzle: 2.5 cm diam., 0.4 cm width, 0° tilt  
Initial Profile



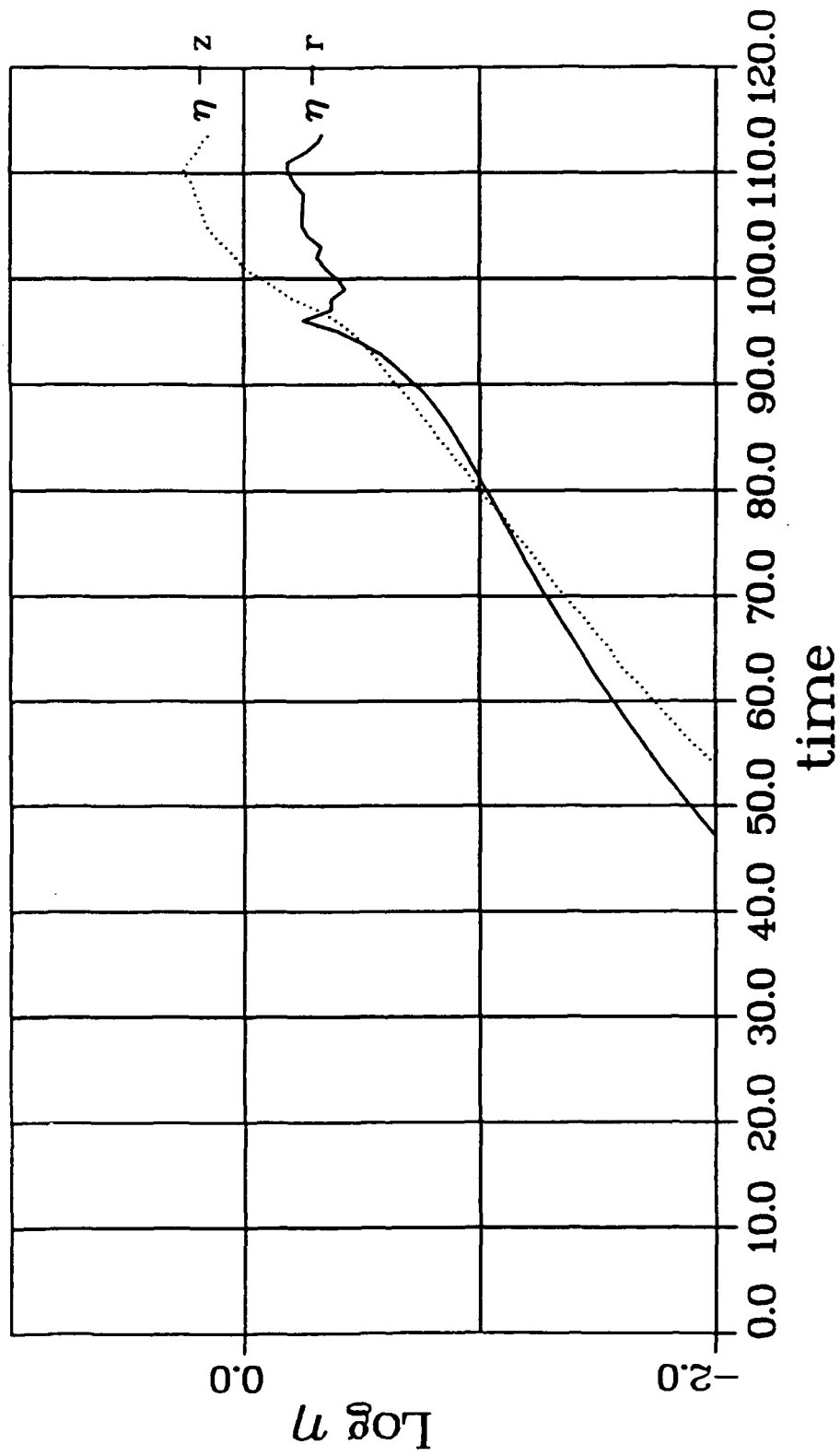
Nozzle: 2.0 cm diam., 0.4 cm width, -10° tilt  
Initial Profile



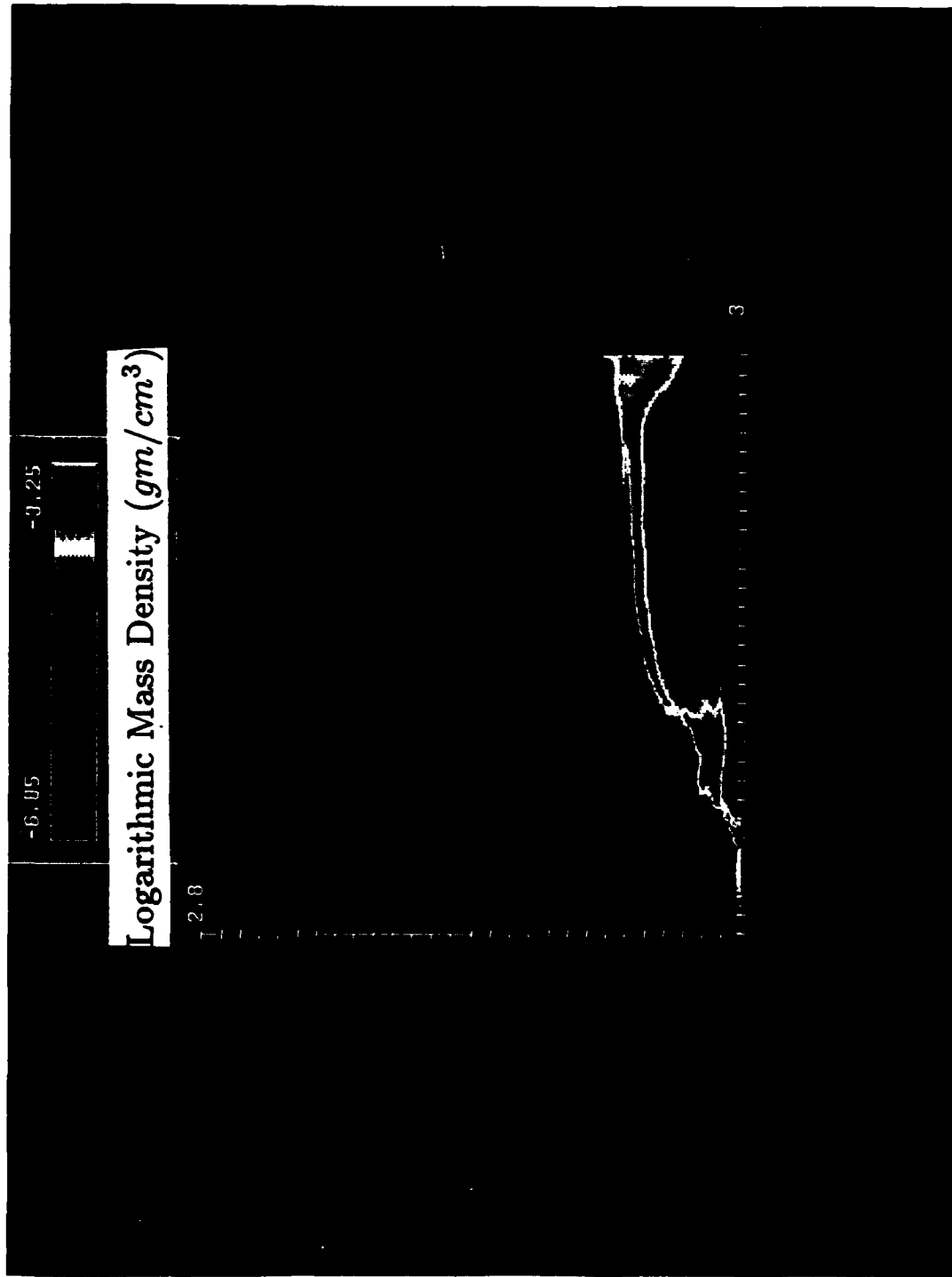
Nozzle: 2.5 cm diam., 0.4 cm width, -10° tilt



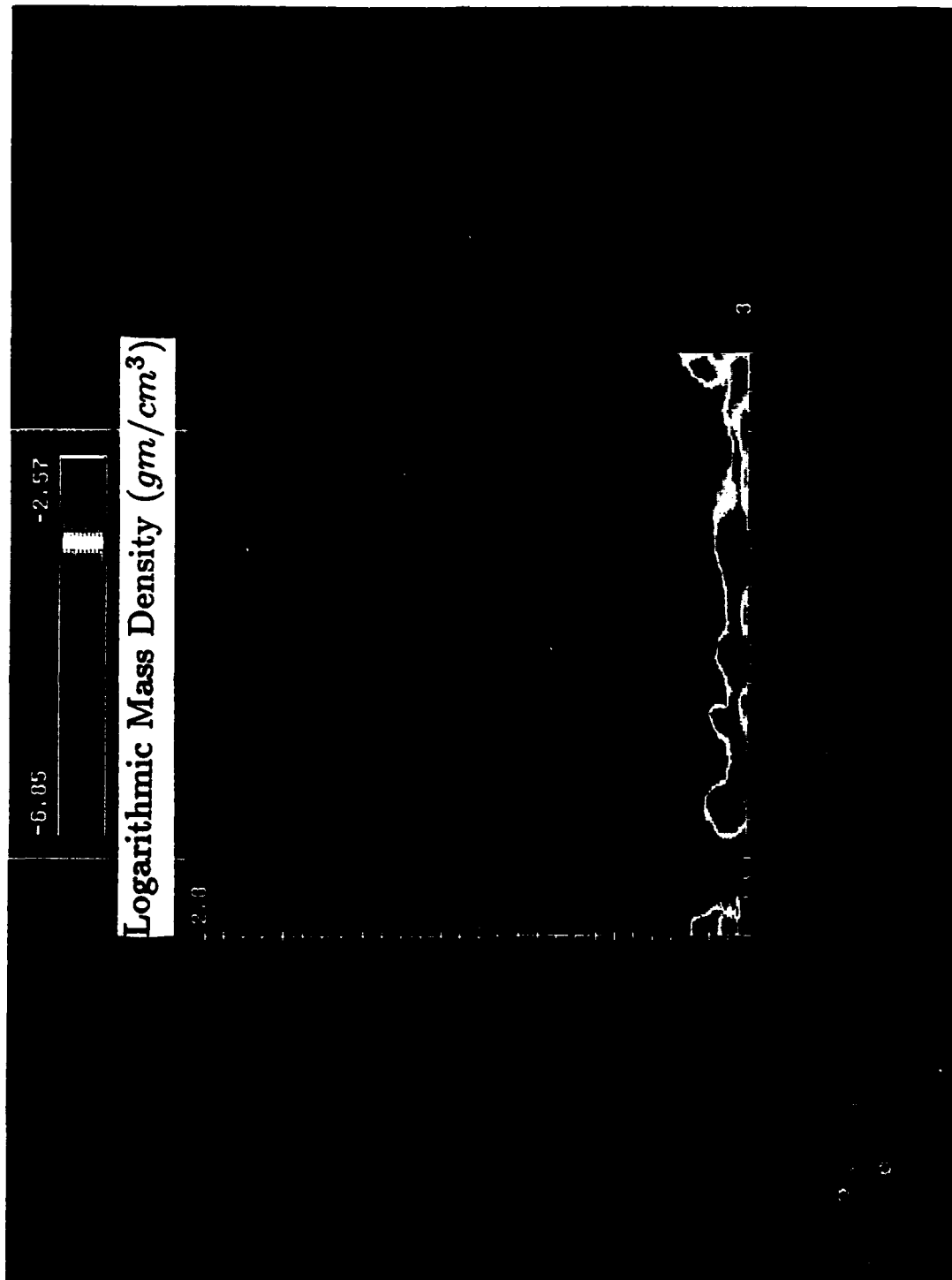
Nozzle: 2.5 cm diam., 0.4 cm width, 0° tilt



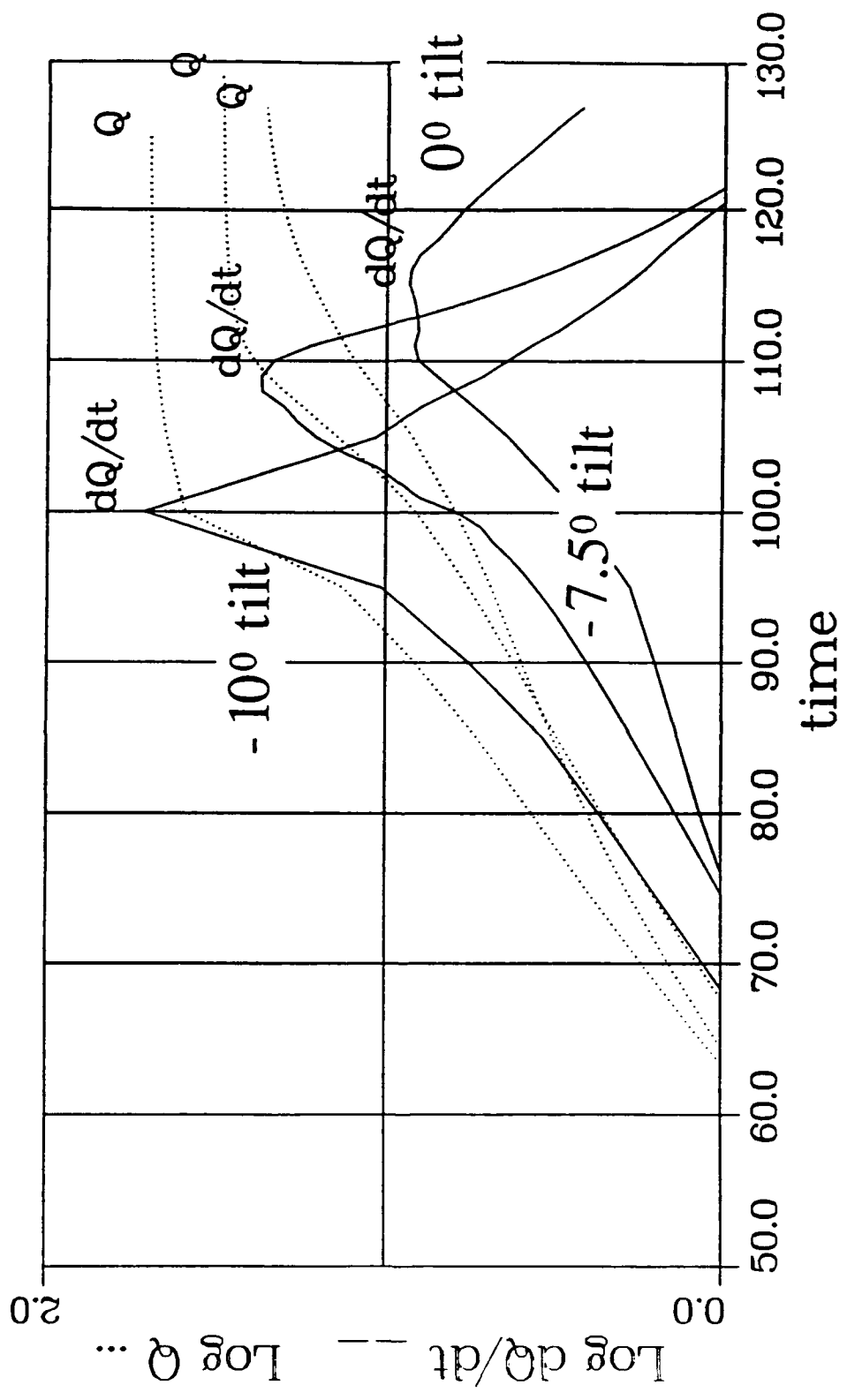
Nozzle: 2.5 cm diam., 0.4 cm width, 0° tilt  
110 nsec



Nozzle: 2.5 cm diam., 0.4 cm width, -10° tilt  
100 nsec



Nozzle: 2.5 cm diam., 0.4 cm width



Nozzle: 2.5 cm diam., 0.8 cm width

